5-2018

3D Micromachining of Optical Devices on Transparent Material by Ultrafast Laser

Yang Song
Clemson University, song5@g.clemson.edu

3D MICROMACHINING OF OPTICAL DEVICES ON TRANSPARENT MATERIAL BY ULTRAFAST LASER

A Dissertation
Presented to
the Graduate School of
Clemson University

In Partial Fulfillment
of the Requirements for the Degree
Doctor of Philosophy
Electrical Engineering

---

by
Yang Song
May 2018

Accepted by:
Dr. Hai Xiao, Committee Chair
Dr. Lin Zhu
Dr. Pingshan Wang
Dr. Fei Peng

ABSTRACT

Ultrafast lasers, also referred to as ultrashort pulse lasers, have played an important role in the development of next generation manufacturing technologies in recent years. Their broad range of applications has been investigated in the field of microstructure processing for the biomedical, optical, and many other laboratory and industrial fields. Ultrafast laser machining has numerous unique advantages, including high precision, a small heat affected area, high peak intensity, 3D direct-writing, and other flexible capabilities When integrated with optical delivery, motion devices and control systems, one-step fabrication of assemble-free micro-devices can be realized. In particular, ultrafast lasers enable the creation of various three-dimensional, laser-induced modifications using an extremely high peak intensity over a short time frame, producing precise ablation of material and a small heat affected area in transparent materials. In contrast, lasers with longer pulse durations are based on a thermal effect, which results in significant melting in the heat affected area. In general, ultrafast laser micromachining can be used either to subtract material from or to change the material properties of both absorptive and transparent substances.

Recently, integrated micro-devices including optical fiber sensors, microfluidic devices, and lab-on-chips (LOC) have gained worldwide recognition because of their unique characteristics. These micro-devices have been widely used for a broad range of applications, from fundamental research to industry. The development of integrated glass

micro-devices introduced new possibilities for biomedical, environmental, civil and other industries and research areas. Of these devices, optical fiber sensors are recognized for their small size, accuracy, resistance to corrosion, fast response and high integration. They have demonstrated their excellent performance in sensing temperature, strain, refractive index and many other physical quantities. In addition to the all-in-fiber device, the LOC is another attractive candidate for use in micro-electro-mechanical systems (MEMS) because it includes several laboratory functions on a single integrated circuit. LOCs provide such advantages as low fluid volume consumption, improved analysis and response times due to short diffusion distances, and better process control, all of which are specific to their application.

Combining ultrafast laser micromachining techniques with integrated micro-devices has resulted in research on a variety of fabrication methods targeted for particular purposes. In this dissertation, the direct creation of three-dimensional (3D) structures using an ultra-fast laser was investigated for use in optical devices. This research was motivated by the desire to understand more fully the relationship among laser parameters, material properties and 3D optical structures. Various all-in-fiber sensors in conjunction with femtosecond laser ablation and irradiation were investigated based on magnetic field, temperature and strain application. An incoherent optical carrier based microwave interferometry technique was used for in-situ weak reflector fabrication and a picosecond laser micromachining technique was introduced for developing LOCs with unlimited utilization potential.

DEDICATION

To:

My parents!

ACKNOWLEDGMENTS

Firstly, I would like to express my sincere gratitude to my advisor Prof. Hai Xiao for the continuous support of my Ph.D. study and related research, for his patience, motivation, and immense knowledge. His guidance helped me in all the time of research. I could not have imagined having a better advisor and mentor for my Ph.D. study.

I also would like to thank Dr. Fei Peng, Dr. Pingshan Wang, and Dr. Lin Zhu for taking their valuable time and being my committee member. I appreciate their advices and questions on my dissertation. Here's a special thanks to Dr. Fei Peng for co-advising me on my research projects and giving me the directions of breaking through.

I would like to thank my lab mates for all the help and support. With these amazing people, I had the chance to learn many things that I may miss on my own path. They also gave me so many valuable suggestions and advices on the work during these years. Special thanks to Dr. Liwei Hua, Jincheng Lei and Qi Zhang for assistance in my research. The results presented here is definitely the team work with my talented group mates.

Finally, I would like to thank my parents for always being my side, giving me endless love and support, encouraging me for being a strong person.

TABLE OF CONTENTS

Page

LIST OF TABLES

Figure Page

LIST OF FIGURES

Figure Page

CHAPTER ONE

INTRODUCTION

1.1 Laser Material Processing Technologies

The laser, along with the transistor and the computer, is considered one of the landmark inventions of the past sixty years, with the initial small ruby rod that crossed the threshold of laser emission introducing the laser industry [1]. Even though this breakthrough and the resulting demonstration earned headlines at that time, there was no rush to apply this new technology, explaining why lasers were referred to as "a solution looking for a problem." However, in the 1960s people began using lasers as cutting tools, opening up the possibilities for developing non-contact precision machining technique [2]. In the 1970s, an Italian company invented the three-dimensional laser-cutting process, and forty years later, this high-performance method is being used extensively in both industrial and laboratory applications [3]. This flexible, non-contact, pressure-free process can manufacture high quality finished products directly from the target material.

Currently, many modern technologies employ laser cutting and engraving processes [4] because of their wide-range of advantages. For example, laser cutting is a high precise process with outstanding spatial stability, a narrow cutting width and involving only a small area affected by the heat [5]. Furthermore, lasers can be used in various environments and with materials ranging from metal, plastics, glass, ceramics and organics (leather, fabric, paper, wood) as well as other raw and post-processed materials.

In addition to laser cutting, laser engraving, drilling and welding are considered as laser material processing [6].

The laser market in 2016 showed an increase in laser material processing applications, primarily because of the demand for the glass used in advanced devices [7]. For example, consumer electronics, the primary driver of the laser market, requires thin glass, tempered glass, sapphire windows, round contours, slots and button holes in their new designs [8], features appropriate for laser processing and its advantages of mechanical turning, drilling and polishing. In addition, this hands-free process offers high speed, accuracy and bend strength, also advantages over such traditional methods as mechanical turning, drilling and polishing. Furthermore the laser cutting process does not necessarily require supplementary conditions before or after [9], leaving target material or parts clean and neat, ensuring high production rates, competitive quality and fewer processing steps. The material selection and manufacturing task have furthered the development of various other processes, one example being gas lasers which have the capability of cutting straight, clean edges of high quality at an impressive speed [10]. As a result. advanced laser tools based on non-thermal processing have become increasingly more wide-spread in applications requiring miniature products.

In addition to the commercial needs, laser material processing and laser cutting also create the powerful precision tools necessary for fundamental research and lab experiments [11], especially important in the biological and medical fields. Much interest has focused on fabricating functional devices, in particular micro devices, are considered as the most promising and the closest to realization [12].

1.2 Advanced Ultrafast Lasers

Recently, various lasers have been investigated for use in material processing, with all of them from gas to solid state lasers exhibiting excellent capability for cutting, engraving and other types of material modification. One of the newest development in this area is the ultrafast laser, which has high output power and power density (i. e., the power of unit area)[13]. These lasers have seen unprecedented success since being introduced, with researchers continuing to improve their time and output limits. Currently, an integrated ultrafast laser system can produce a peak power of up to 10^{15} watts, much higher than the 10^{12} watt average of the world's power grid. The current time scale of the laser pulse can reach several femtoseconds (10^{-15}seconds), while light travels only 0.3 microns[14]. Because of its compact shape, the ultrafast laser machine has made innovative experimental methods under extreme physical conditions possible. For research both in and outside of laser laboratories, the high laser peak power and ultrashort pulse duration make ultrafast lasers very attractive, opening potential new paths in the engineering and scientific domains [15].

Some example applications are listed in Table 1 below:

Table 1 Ultrafast Laser Applications

APPLICATIONS	LASER REQUIREMENTS
TWO-PHOTON POLYMERIZATION	High laser peak power Short pulses
TIME-DOMAIN TERAHERTZ	< 100 fs pulse width 1560 nm, 780 nm
PUMP-PROBE SPECTROSCOPY	Phase coherent dual-beam system Independently configured outputs
MATERIAL PROCESSING	Picosecond or sub-picosecond pulses 1030 nm or 1064 nm
ATTOSECOND SCIENCE	CEO-free laser pulses Mid-IR radiation for OPCPA
OPTICAL COHERENCE TOMOGRAPHY	Very broad wavelength spectrum, Supercontinuum

The primary advantages of ultrafast lasers include their compact size, excellent beam quality, and high machining stability. Their micromachining technology is dramatically different from conventional laser processing methods, which use either a continuous wave (CW) or longer pulsed lasers [16]. The most significant differences, however, come from the physical principle or laser-matter interaction mechanisms of laser-induced material processing. Compared to micromachining with CW and longer-pulse lasers, ultrafast lasers offer several unique advantages: micro- or even nano-size structure creation; no collateral damage to the surroundings; a clean look after processing,

resulting in a minimal heat affected zone; no material property change; and the capability for transparent material sub-surface engraving. Femtosecond lasers and picosecond laser micromachining, more advanced areas of ultrafast laser applications, are receiving increasingly more attention. Furthermore, ultrafast laser micromachining processes do not rely on linear absorption at certain laser wavelengths [17]. As a result, virtually any dielectric, metal, and mechanically hard material can be processed by the same laser beam.

1.3 Fiber optic sensors

The technology of optical fiber sensing began to attract attention in 1977 [18] with the development of optical fiber communication. Since then this technology has been widely used in many fields, including the military, national defense, aerospace, energy, environmental protection, industrial control, medical science, measurement testing, construction among others [19]. As a result there are hundreds of fiber sensing technologies in the world measuring various physical quantities such as temperature, pressure, flow, displacement, vibration, acoustic and radiation.

Optical fiber works within a wide bandwidth and over a large dynamic range in addition to being suitable for telemetry remote control, immune to EMI, resistant to chemical corrosion, and exhibiting high sensitivity[20], all of which make it a good low-loss transmission line. Under certain conditions, an optical fiber can exhibit excellent sensitivity, making it easier to measure or load compared to other sensing technologies. As a result, optical fiber sensing technology has become the preeminent sensors, promoting the development of advanced sensing technology [21], with the Fiber Bragg grating sensor

and long period fiber grating being the most widely used structures in optical fiber sensors. Their sensing process is based on the wavelength shift and magnitude change of reflections, both of which are used to obtain the sensing information through these external physical parameters. The most common components of fiber gratings are an appropriate light source and photosensitive fibers [22]. The refractive index of the optical fiber changes with the spatial distribution of the light intensity. When this variation of the refractive index is saved in the fiber, it becomes a grating made by gas laser irradiation, chemical etching, mechanical dicing or electric arc modification[23]. However, the long-term reliability of these gratings has been a concern due to the degradation of their optical properties and mechanical strength when they are exposed to high temperature and high pressure environments.

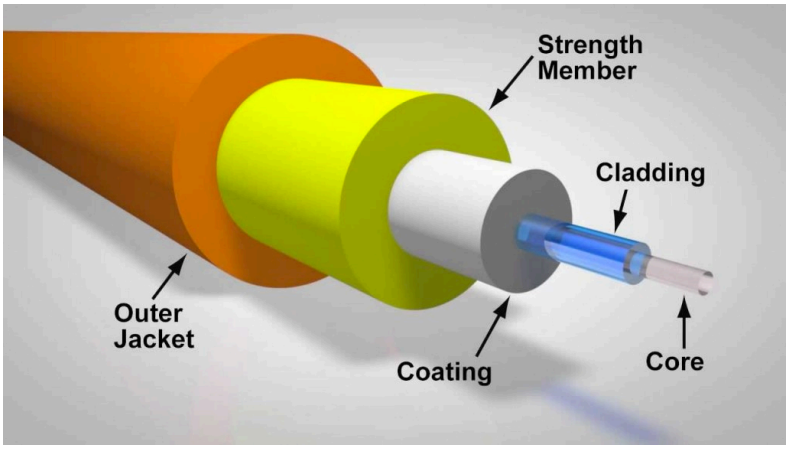

Figure 1.1 Schematic representation of the optical fiber

Fabry-Perot interferometers (FPI) have also been successfully used in optical fiber sensing applications[24]. Their micron-sized cavities, which are related to the wavelength of the light source, have been found to accurately measure physical quantities such as

temperature, pressure, strain, and pH values[25]–[29]. However, fabrication of these FPI sensors involves a complicated assembly of multiple components responsible for the robustness of the device due to the limited strength of the joints. Various advanced manufacturing methods have also been applied for fabricating FPI sensors, including tapering, fusion splicing, laser welding and irradiating, UV/excimer laser irradiating, and focused ion beam (FIB) lithography.

1.4 Lab-on-chip devices

Over the past two decades, the area of microfluidics and lab-on-a-chip has experienced explosive growth[30]. A lab-on-a-chip (LOC) is a small device that integrates a number of laboratory functions within one integrated circuit (generally called a chip) the size of millimeter to a few square centimeters for achieving automation and high-throughput screening. LOCs are designed to deal with extremely small fluid volumes down to several pico-liters. It has a broad range of uses in medical, physical and bio experiments even though they can be complicated to manufacture and operate [30]–[34]. Researchers have produced many types of functional microfluidic LOC devices using different approaches.

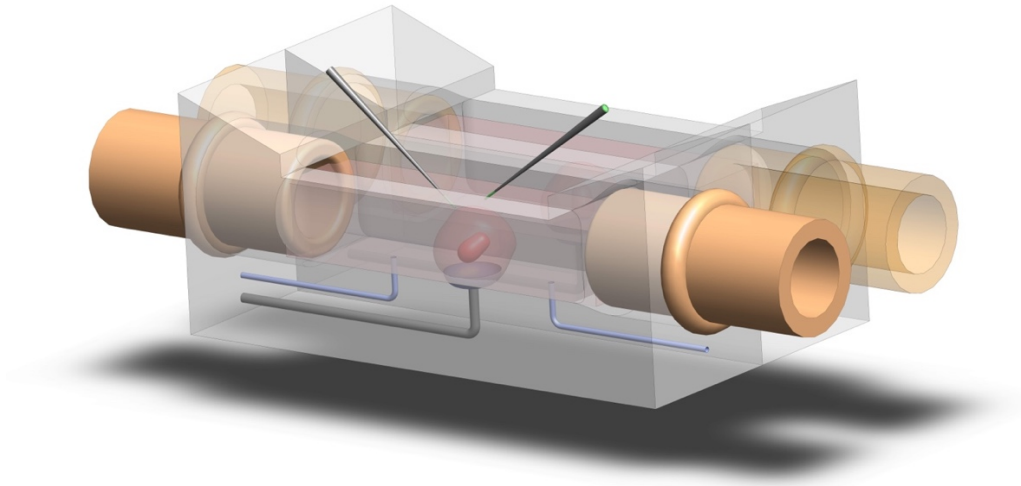

Figure 1.2 Schematic of an integrated cell testing LOC device

The challenges involved in fabricating LOC devices, especially their linear structure, are detailed below [35]

1. The sizes need to be sufficiently long to ensure completion of the chemical reactions.
2. The inner walls need to be smooth to avoid disturbing the fluidic dynamics or damaging the samples.
3. The fabrication resolution should be as high as possible to produce channels in micro sizes.

The most common method of LOC fabrication is photolithography. However, this process is limited to a 2.5D procedure as chemical etching is required, an issues as all of the challenges listed above require a high efficiency fabrication system that includes a

powerful ultrafast laser, an advanced control center, and precision motion devices with high speeds.

1.5 Motivation and objective

Given the these technical challenges, research on controlling the laser-induced damage and on manufacturing high performance devices is urgently needed. Past research has shown that the formation of the laser-induced damage depends on the three key issues: the laser parameters, the environment, and the material. Since the physical mechanism of laser-induced damage is impacted by many variables and conditions, it has been difficult to determine the precise cause of laser-induced damage: specifically what triggers its occurrence and how it can be partially if not fully avoided.

When researchers first began to investigate laser material processing, they explored four major questions, ones that we are still asking today: What happens? What is laser damage? Which laser? And how can it be controlled? While we can answer them to a certain degree, there is still more work that needs to be done. Thus, the primary objective of this dissertation is to directly create three-dimensional (3D) structures using an ultra-fast laser. The most important issue is to determine the relationship among the laser parameters, the material property and the 3D structure required. This research focused on laser irradiation-based fiber optic sensors and laser ablation-based LOC devices realized by fs lasers and ps lasers. The advantages of each type of optical device are listed below: These two kinds of optical devices both have unique advantages that I listed here

Fiber optic sensors (Femtosecond laser)

- Dependable performance (assembly-free)
- Mechanical robustness
- Long-term stability
- Fast installation and maintenance
- Economical cost

Lab-on-chip devices (Picosecond laser)

- Portability and integrity
- Higher sensitivity
- Shorter time-to-result
- Less laboratory space consumption
- High-speed serial processing

1.6 Organization of the dissertation

This dissertation focused on directly creating three-dimensional (3D) structures using an ultra-fast laser. I conducted experimental studies and investigated the performance of the fabricated devices to explore the ultrafast laser assisted micromachining technique. The dissertation is organized as follows. Chapter 1 summarized the laser material processing and discussed the motivation for and background and the objective of this work.

Chapter 2 introduces a brief review of laser cutting, laser-matter interaction and the ultrafast laser micromachining technique including discussing the fundamental physics describing femtoseond laser direct writing on transparent materials. The next chapter, Chapter 3, explores the femtosecond laser system setup, including the procedure development, the three-dimensional fabrication and the performance of the entire system of fs laser assisted sensing applications. In addition, sensors fabricated on a single mode fiber with a Febry-Perot interferometer for the purpose of strain, temperature and optofuildic sensing are discussed. Chapter 4 discusses in-situ weak reflector fabrication

using an optical carrier based microwave interferometry (OCMI) system for SMF, MMF, cascaded or longer FP cavities. The OCMI provides the opportunity to monitor the reflectance of weak reflectors. Multiple in-situ fabrication parameters are also discussed.

Chapter 5 introduces the overall procedure for the laser-assisted additive manufacturing technique, including the picosecond laser micromachining system used here, and Chapter 6 discusses the lab-on-chip technology and its applications. Manufacturing of microgrooves and microchannels in LOC devices with sufficiently long dimensions and smooth surfaces are analysed, and two laser fabrication methods for generating microgroove structures in fused silica glass substrate are compared for the application of microliter-volume reactors, which takes advantage of large surface area-to-volume ratios. Chapter 7 concludes this dissertation, summarizing the work presented and outlining research to be continued in the future.

1.7 Innovations and Contributions

The major scientific and technical contributions of this dissertation are discussed below.

A femtosecond laser micromachining system and a picosecond laser assisted additive manufacturing system were developed as well as three-dimensional manufacturing methods and laser processing techniques for fabricating integrated optical fiber sensors, lab-on-chip and other specific functional devices.

A ferrofluid-based optical fiber magnetic field sensor was fabricated through femtosecond (fs) laser ablation. With the help of an fs laser micromaching technique, a built-in micro-reservoir inside a singlemode optical fiber was fabricated inside a single mode fiber and capillary tube. The micro-reservoir functions as a fiber inline Fabry-Perot (FP) cavity which is filled with a ferrofluidic liquid. The refractive index of the ferrofluid varies as the surrounding magnetic field strength changes, a change that can be optically probed with the FP interferometer.

An intrinsic Fabry-Perot interferometry (IFPI) temperature sensor system with a self-compensate in strain fabricated by a Femtosecond (FS) laser is presented. This sensor is composed of two cascaded IFPIs of cavity lengths of 100μm and 500μm based on the wavelength tracking method. During fabrication, the intact puffer coating of the optical fiber is maintained unlike for the normal approach frequently used for maintaining the optical mechanical properties.

A polymer optical fiber (POF) based cascaded intrinsic Fabry-Perot interferometer (FPIs) system, which has the unique ability to measure distributed large strains along the fiber, is also presented. The optical carrier based microwave interferometry (OCMI) technique was used to in-situ fabricate the sensor structure and interrogate the POF-based cascaded FPIs system.

Two laser fabrication methods for generating microgroove structures on a transparent fused silica glass substrate, creating a microfluidic environment appropriate for very small fluid volumes and enabling control of microliter-volume reactors while taking advantages from large surface area-to-volume ratios, were developed.

A ferrofluid based optical fiber magnetic field sensor was fabricated through femtosecond (fs) laser ablation. With the help of an fs laser micromaching technique, a built-in micro-reservoir inside a singlemode optical fiber was fabricated inside a single mode fiber and capillary tube. The micro-reservoir functions as a fiber inline Fabry-Perot (FP) cavity which is filled with a ferrofluidic liquid. The refractive index of the ferrofluid varies as the surrounding magnetic field strength changes, a change which can be optically probed with an FP interferometer.

CHAPTER TWO

LASER MATERIAL PROCESSING TECHNOLOGY AND APPLICATIONS

2.1 Invention of laser cutting tools

The laser is one of the great inventions of the twentieth century, with inestimable technological potential. While the current leader in electronic technology is computer science, it is believed that the next generation will be the age of light technology with a focus on lasers. Lasers, which are characterized as monochromatic, directional and coherent [17], are seen as the most promising tool in material processing applications, with more than twenty types of laser processing technology currently in use. This technology is an especially effective technique for cutting, welding, surface processing, drilling and micro-processing of materials, both metallic and nonmetallic. The spatial and time control of laser processing is outstanding as is its ability to work with a wide range of target materials, shapes, and sizes and processing environments, making it the process of choice in the manufacturing domain.

In its early development due to its small output power, the laser was primarily used for drilling small holes and micro welding. By the 1970s with the emergence of high-power carbon dioxide lasers, high-repetition frequency Yi, and the development of laser processing mechanisms and processes, this technology saw significant improvements and consequently its scope expanded [36]. Laser processors with thousands of watts of output have been used for high-speed cutting, deep-melting welding and material heat treatment. In addition, a variety of specialized laser processing equipment, integrated with

photoelectric tracking, computer digital control, industrial robots and other automated technologies, has seen significant improvement [37].

2.2 Laser Cutting Technique

In its most general sense, laser cutting technology is used in processing both metallic and nonmetallic materials, reducing the processing time and cost while at the same time improving the quality of the workpiece, becoming the "sword" that people have dreamed of [9], [38]. A laser manufacturing system consists of the control system, the motion system, the optical system, the cooling system, and the exhaust gas and the air-gas protection systems. The most advanced numerical control mode is used to achieve multi-axis linkage, and the laser itself is not affected by the speed of processing. Furthermore, the system supports DXP, PLT, CNC and other graphics formats, all of which strengthen its capability for interface graphic processing. Typical systems also uses servo motors with superior performance and drive-oriented structures to achieve excellent motion accuracy in a high-speed state.

Laser cutting is achieved by the high density energy produced by the focusing of the laser. Controlled by the computer control center, the output of the repeated high-frequency pulse laser forms a beam of a certain frequency and width [39]. This pulse beam passes through, reflects and focuses on the surface of the object by focusing a lens group, forming a small, high-energy density spot and melting or vaporizing with the heat created from every pulse.

2.3 Laser Material Processing Characteristics

As an advanced manufacturing technology, laser processing has been widely used in the automotive, electronics, electrical appliance, aviation, metallurgy, and machinery manufacturing domains as well as in various other areas as producing pollution-free materials and reducing material consumption have become increasingly more important [40]. Laser processing is a comprehensive technology involving light, machinery, electricity, materials and measurement. Traditionally, it can be divided into nine aspects.

1. Laser processing systems including the laser machine, optical system, processing tool, control system and detection system.
2. Laser processing technology involving principles of welding, surface treatment, drilling, marking, fine-tuning and other material processing techniques.
3. Laser welding including car body thick sheets, auto parts, lithium batteries, seal relays, and various devices requiring no welding pollution and deformation.
4. Laser cutting including the automobile industry, the computer, electrical casing, a wide range of metal parts and special material cutting, circular saws, acrylic, spring gasket with YAG lasers and CO_2 lasers.
5. Laser marking widely used for almost all materials and nearly all industries.
6. Laser drilling primarily used in the aerospace, automotive manufacturing, electronic instruments, and chemical industries. Due to rapid development, the average output power of the YAG laser used for laser drilling has increased from 400 to 800w[41]. Applications of more mature laser drilling include the

production of artificial diamonds, natural diamonds, jewel bearings, aircraft blades, multi-layer printed circuit boards and other products. The lasers in use include CO_2 lasers and some Excimer lasers.

7. Laser heat treatment is widely used in the automobile industry for crankshafts, piston rings, commutators, and gears. Aerospace, machine tools and other mechanical industries also use lasers as a processing method [42]. CO_2 lasers are primarily used.
8. Laser rapid prototyping including the combination of laser processing technology and computer CNC technology. It is a flexible manufacturing technique, which is frequently used in the mold and model industry.
9. Laser coating including a wide range of applications in the aerospace, mold and electromechanical industries. High power lasers are primarily used.

Laser processing technology has many advantages compared with traditional processing technology, so it has been widely used in industry and laboratory applications, especially in the development of new products. Once a drawing is formed, the laser can process it immediately, producing the desired product in the shortest amount of time possible.

The rapid wide-spread use of laser cutting resulted due its ability to cut more quickly with higher quality than such competing processes as punch, plasma, abrasive waterjet, ultrasonic, oxy flame, sawing and milling [43]. Eighty percent of the industrial lasers are employed for metal processing. Further, its unique attraction is that it provides a clean environment and production process for industrial manufacturing; this is the most

important advantage of laser processing. Other advantages of laser material processing are listed below [8]:

- Small point of light, energy concentration, cutting depth dependent on the laser output power; 10-20mm is the current scale for well-finished cutting, while some extremely high power lasers can cut as deep as 50 mm.
- Hands-free, leaving workpiece clean. Target pieces do not need clamping. But some type of holder is suggested for avoiding movement with stage acceleration and for position locating.
- No electromagnetic interference. It is more convenient than using electron beam processing.
- Laser beams are easy to focus and guide, and are controlled automatically.
- Wide range: almost any material can be carved and processed--friable, brittle, electric conductors or nonconductors, hard or soft. Highly reflective materials such as aluminum may be problematic, requiring laser parameter adjustment to achieve satisfactory cutting. In addition, cutting may occur in polarization directions that might affect the processing efficiency.
- Safe and reliable: the key process step is the non-contact cutting. The use of non-contact processing eliminates mechanical pressure or mechanical stress.
- Precise: the processing precision can reach several micro-meters.
- The effect is consistent, ensuring equal quality for the entire batch processed.

- Fast speed: Laser is one of the fastest cutting tools. It can quickly carve and cut based on the design from the computer output. And laser cutting is much faster than the traditional processes.
- Low cost: no limitation in processing quantity. Especially for small batch processing services, laser processing is cheaper. Only procedure programming modifications with high flexibility are required for multiply tasks.
- Processed surface is smooth: the cutting surface of the laser has no burr. The cut edge is smooth. It is one-step cutting, with no further processing being necessary in most cases.
- Heat deformation is small: as the processing area is small and speed is fast, the dropping energy is concentrated. There is a very small area is affected by the heat, resulting in a very thin solidified layer of a few micro-meters, particularly on fragment-free processing with negligible distortion.
- Suitable for processing large products: the manufacturing cost of large products is costly in both space and assistance. Laser processing does not require mold manufacturing because the material is cut, meaning it can reduce the production cost while at the same time improving the quality of the products.
- Saves material: laser processing uses computer programming such as CNC for controlling, It can make the product in different shapes, maximizing the utilization of materials, This process reduces the cost of raw material.

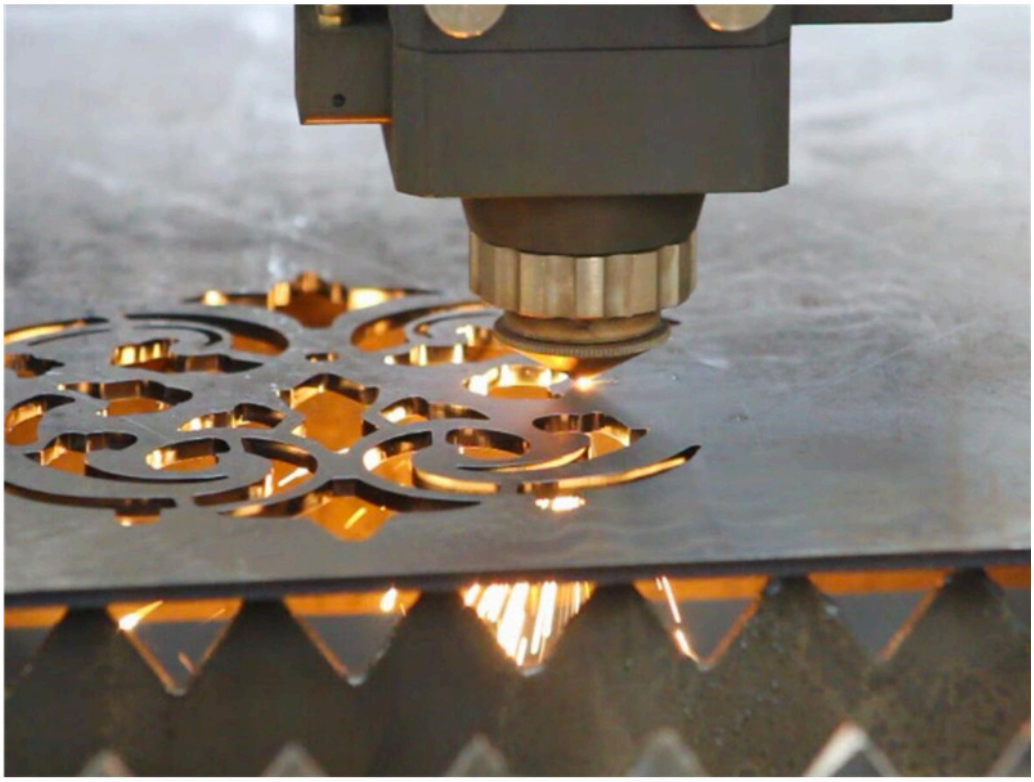

Figure 2.1 Gas laser is utilized in cutting metals with clean edge and flexible pattern

The laser marketplace has reported that the rapid development of this market in the Asia-Pacific region is a major factor in the rapid growth of the laser industry. The rate of growth in China, Japan and Korea is particularly prominent. Over the next five years, these areas will be the major contributors to the laser processing of automobile manufacturing, raw equipment manufacturing and other industries.

2.4 Laser Material Processing Mechanism

2.4.1 Comparison of Laser Mechanism in Different Duration

In laser processing the focused laser beam serves as a heat source for the workpiece, either metallic or nonmetallic, melting and evaporating the active area to form small holes, incisions, connections, and other processing goals. It is essentially the process of the interaction between the laser and the material. The energy transmission interaction of various kinds of lasers and the laser-induced effects of wavelength, environmental fluence and surface condition on energy absorption rate are different for different laser processing methods [44]. The mechanism of the interaction between the laser and the target can be produced in various ways. For example, the laser beam can be guided and passed over a numerically calculated optical delivery path and material removal can occur through a series of mechanisms. In comparison, vaporization requires more laser energy than melting does, and thermal stress, cracking and scribing require relatively low laser power.

Another laser processing phenomenon, referred to as cold ablation, is characterized by an ultrashort pulse laser [45]. The resulting interactions between the beam and material have opened a new generation of micromachining applications. This type of laser material processing is dramatically different from such conventional laser tools as continuous wave (CW) laser or longer duration pulsed lasers, the primary differences resulting from the theoretical principle and mechanisms of laser-induced material processing [17].

For continues wave or longer pulse laser beams, effective irradiation and ablation on/in materials occur from melt expulsion driven by the vapor pressure and the recoil pressure of light. These are considered unstable processes because the dynamics of the fluid phase and the vapor conditions are complicated: the melt layer is solidified, leaving permanent geometric modifications [46].

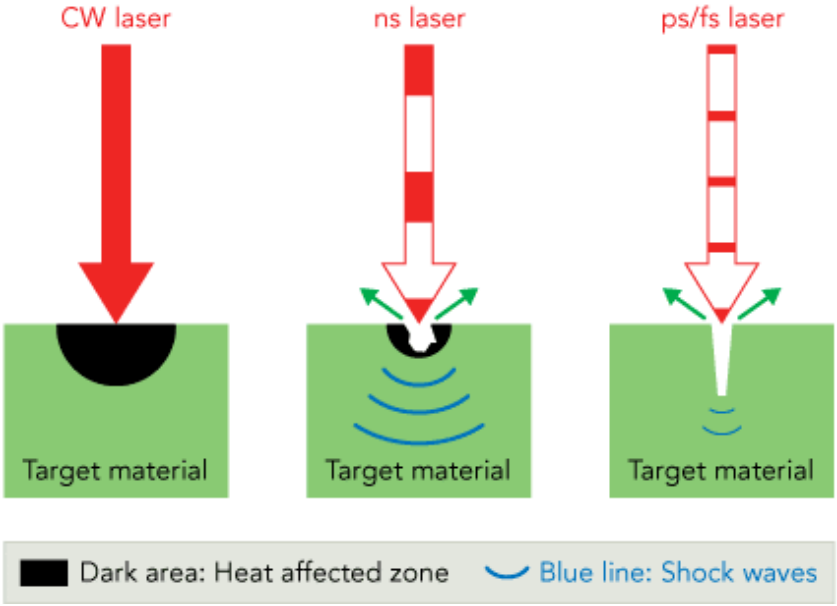

Figure 2.2 Schematic mechanism of CW, ns and ultrafast laser pulse

Figure 2.2 shows the schematic mechanisms of continuous wave (CW), nanosecond (ns), and pico/femtosecond (ps/fs) laser pulses. The black areas indicate the size of the heat-affected area (HAZ), while the blue lines show the shock waves created by the light pulses. The CW laser removes material through a thermal effect, melting, with creating a very large HAZ. The cutting, which is achieved by heating the shooting area until it becomes a fluid, does not result in changes in the properties of the material. For longer

pulse durations, as exemplified with an ns laser [47], part of the material is removed though evaporation because the pulse energy is high enough to disrupt the bandgap. But the HAZ for ns laser cutting is a concern as it is for ps/fs laser ablation since the pulse duration is longer than the time need to transfer the energy from electrons to lattices [48].

2.4.2 Ultrafast Laser Matter Interaction

Laser-matter interactions for ultrafast lasers are complex because of the number of processes occurring in a short time. When an extremely high intensity of light is incident on the material, an electron can be excited by multiple photons, even if the photon energy is smaller than the band gap. High intensity focused ultrafast laser pulses with wavelengths (λ) of 800 nm have insufficient photon energy to be linearly absorbed [45]. For this reason, nonlinear photoionization is used to promote electrons from the valence band to the conduction band, thus generating free electrons.

Typically, there are two steps in this ionization process: nonlinear photoionization and avalanche ionization. Nonlinear photoionization refers to direct electron excitation by an electric laser field. This process generates seed electrons that will participate in the next process. Photoionization involves multiphoton ionization and/or tunneling ionization depending on the laser frequency and intensity. Once the free electrons exist in the conduction band, free-carrier absorption occurs, leading to collisional ionization followed by avalanche ionization. This initial process must be nonlinear because the there are no electronic transitions allowed by the photon energy [43]. The following rate equation has been widely used to describe this nonlinear photoionization process [49] (the combined

action of multiphoton excitation and avalanche ionization):

$$\frac{dn_e(t,r,z)}{dt} = \delta_m(I(t,r,z))^m + a_i I(t,r,z) n_e(t,r,z)$$

where t is the time, r the distance to the Gaussian beam axis, z the depth from the surface of the bulk material, n_e the free electron density, I(t, r, z) the laser intensity inside the bulk material, m the order of the multiphoton process, $and\ \delta_m$ the cross-section of the m-photon absorption. For materials with defects or dopants, electrons can initially be excited from these low-lying levels via linear absorption or thermal excitation. For pure dielectrics, such electrons are generated by nonlinear photoionization (i.e., ultrashort pulses). Then, free electron plasma formation is realized.

This strong dependence on intensity also means that the photoionization process is more efficient for lasers with short pulse durations. For long pulse lasers (i.e., ns), the photoionization process cannot efficiently generate sufficient seed electrons, and the excitation process relies on the low concentration of impurities with energy levels distributed randomly close to the conduction band. As such, the modification process becomes less deterministic, and precise machining is not possible for longer pulses [50]. In other words, the laser pulse width is shorter than the time taken for the absorbed energy to diffuse into the material. Since the lattice heating time is on the order of 10 ps, which is much longer than the pulse duration of the fs and ps laser beam, less energy is needed to achieve the intensity for optical breakdown with respect to short pulses, and high precision micromachining can be achieved [48]. The material realizes a phase or structural modification, leaving behind a localized permanent change.

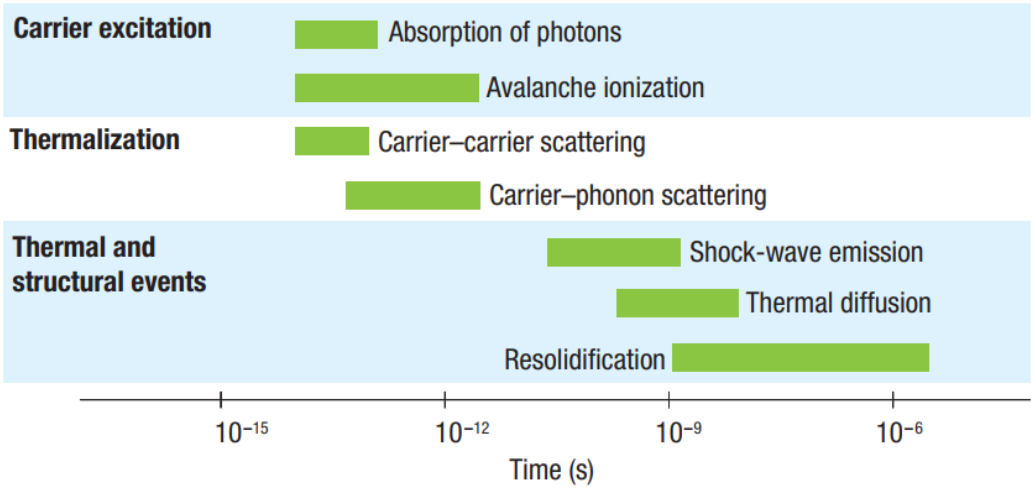

Figure 2.3 The green bars represent typical timescales for the relevant process.

Free carrier losses may occur on a time scale comparable to the pulse duration of the ultrafast laser beam in large bandgap materials such as quartz and fused silica. In this work, such losses can be neglected due to the longer pulse duration of the laser we used. Because of these properties of ultrafast lasers, novel techniques such as lasing transparent materials can be explored to remove material or to change its properties [51]. It should be noted that the permanent formations in transparent materials with large bandgap energy also depend on many other exposure parameters, such as pulse duration, repetition rate, laser wavelength, polarization state, and tight/loose focusing condition as well as the scanning speed of the translation stage. Further explanations of these mechanisms are found in the following discussions.

CHAPTER THREE

FEMTOSECOND LASER MICROMACHINING AND NOVEL SENSING APPLICATIONS

Fabry-Perot interferometers (FPI), one of the most widely used optical structures, has been fabricated using various advanced manufacturing methods, including tapering, fusion splicing, CO_2 laser welding and irradiation, UV/excimer laser irradiation, and focused ion beam (FIB) lithography[52]. Femtosecond laser micromachining, which was introduced to fabricate novel optical structures in transparent materials in recent years, has proven to be a reliable and high precision tool, with a fabrication resolution of up to less than 1 μm^2. And for fs lasers assisted FPI fabrication or direct mirror creation [53], laser parameters of, for example, the beam spot size and laser fluence, which are adjusted by such optical elements as the wave plate, filter, or objective lens with different NAs and magnifications, require such precise tuning to satisfy fabrication requirements. For a typical fs laser micromachining system setup, samples are placed onto a precisely controlled three-axis translation stage, and with the help of an in-situ monitoring CCD camera, the fs laser beam is focused on the desired area. In this chapter, two types of FPI-based optical fiber sensors fabricated by fs laser micromachining are discussed [54].

3.1 Integrated Femtosecond Laser System

In this section, the femtosecond laser micromachining system setup will be analyzed and illustrated. The femtosecond laser consists of a Ti: sapphire mode-locked

laser (Mira 900, Coherent Inc.) and a Ti: sapphire regenerative amplifier laser (RegA 9000, Coherent Inc.). The laser parameters are shown below in Table 2.

Table 2 Femtosecond laser machine specification

SPECIFICATIONS		
LASER MODELS	MIRA 900 (Oscillator)	RegA 9000 (Amplifier)
PUMP POWER	8W	10W
PULSE DURATION	200fs	200fs
PULSE ENERGY	2μJ	2μJ
WAVELENGTH RANGE	700-980nm	400-1000nm
AVERAGE POWER	1W	500mW
REPETITION RATE	76MHz	10 kHz to 300 kHz
BEAM DIAMETER	0.8 ±0.1	3mm
BEAM DIVERGENCE	1.7 ±0.2mrad	2mrad

The primary technique used to mode-lock the Mira 900 laser is Kerr Lens Mode-locking (KLM). The optical cavity is specifically designed to utilize changes in the spatial profile of the beam, i.e. self-focusing due to the nonlinear optical Kerr effect, generated in the Ti: sapphire crystal. Occurring in the gain medium itself, this mechanism results in

higher round trip gain in the mode-locked (high peak power) versus continuous wave (CW) (low peak power) operation due to an increased overlap between the pumped gain profile and the circulating cavity mode.

Ultrafast pulses with a spectral bandwidth greater than 10 nm full-width at half maximum (FWHM) from the Mira oscillator are amplified in the RegA Head. The Mira oscillator beam is directed into the RegA head using two mirrors shielded with dust covers and beam tubes. The input beam from the Mira passes through a Faraday Isolator, and a single pulse is injected into the RegA by a TeO_2 acousto-optic Cavity Dumper. Amplification over 20 to 30 round trips allows the GVD in the TeO_2 Q-switch in the RegA to expand this pulse from 200 fs to 30 ps length. The Cavity Dumper then extracts a single pulse of several μJ energy, which returns through the Faraday Isolator and is separated from the input beam path by a polarizer. For a repetition rate at 250 kHz, the average power is approximately 1.0 W for an output energy of 4 μJ. The schematic of the home-integrated fs laser micromachining system with direct writing capability is shown in Fig. 3.1. This ultrafast laser system, which is used for transparent materials processing, sets the central wavelength, pulse width, and repetition rate of the fs laser at 800 nm, 200 fs, and 250 KHz, respectively, and the maximum output power of the laser is 1 W.

A half waveplate [55] in combination with a Glan-Thompson Calcite polarizer [56] is used to precisely control the actual power used for fabrication, while an optional variable neutral density (ND) filter [57] is used to tune the laser power more precisely. The laser exposure is switched on or off by an external mechanical shutter (SH05, Thorlabs) or by electrically gating the internal clock via the laser controller. In general, the laser beam

passes through a commercial microscope objective to generate a tightly focused laser spot. After extensive experimentation to determine the threshold power, the laser energy used for processing silica glass and single crystal sapphire materials is tuned to be approximately 0.4 ~ 0.5 μJ per pulse for RI modulation [58] purposes; however, the energy may be adjusted within this range if the fs laser beam becomes unstable due to laboratory temperature and humidity. Depending on the purpose, various types of optical elements can be applied, including a cylindrical lens for line scanning, a phase mask for grating inscription, or an axicon lens to shape the beam from Gaussian to Bessel for high-aspect-ratio drilling applications.

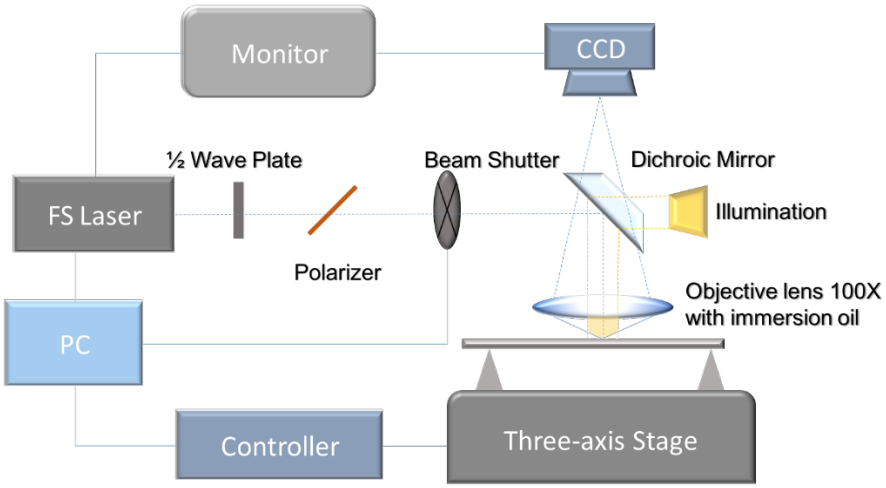

Figure 3.1 Schematic of femtosecond laser system

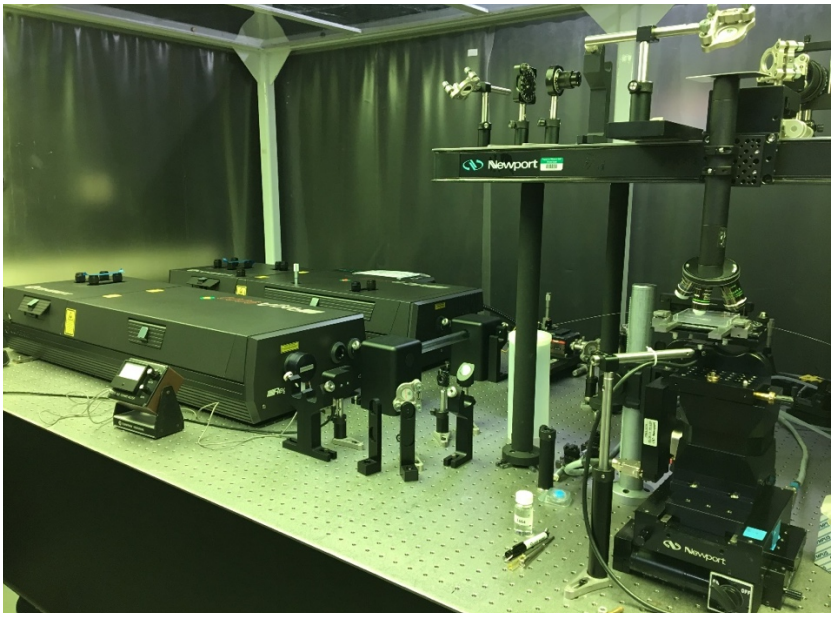

Figure 3.2 Set of the femtosecond laser micromachining system

Substrates or optical fiber samples are mounted on a computer-controlled, three-axis translation stage (PM500 series, Newport, Inc.) with a resolution of 0.1 μm. Depending on the fabrication needed, fiber mounting methods and illumination choices vary as do the velocities of the translation stage. Further details can be found in the following sections. For the research reported here, the fs laser beam is either directly focused on the fiber surface (ablation) through an objective lens (20X) with an NA of 0.4, or focused inside the optical fiber sample (irradiation) using a water immersion lens (20X) with an NA of 0.4 or an oil immersion lens (100X) with an NA of 1.3. The diameter of the focused beam is varied from 0.5 μm to 1 μm depending on the microscope objectives [59]. The spot size of the focal point inside the transparent materials plays a significant role in high accuracy, high precision 3D structure micromachining using fs lasers. Typically, the radius r of the spot size can be roughly calculated by

$$r = \frac{0.61\,\lambda}{NA}\frac{}{n}$$

where λ is the wavelength of the incident laser and λ/ n represents the effective wavelength when the laser is focused inside the media with a refractive index of n [60], meaning the focal spot inside the material is smaller by a factor n than that in air (nair =1). Once the wavelength of the laser and the refractive index of the material are fixed, r depends only on the NA of the microscope objective: the larger the NA, the smaller the spot size. In addition, the immersion lenses (water immersion or oil immersion) usually have larger NAs (NA > 0.9), generating a smaller focused beam spot, compensating for the refractive index mismatch at the sample surface as well, thus producing a better fabrication resolution[61].

For in-situ fabrication, a dichroic mirror and a charge-coupled device (CCD) camera connected to the computer help to in-situ monitor the fabrication process. Front-side and backward illumination methods can be applied as needed depending on the purpose of the fabrication [53]. For example, both methods are suitable for transparent material ablation/irradiation, while for non-transparent materials (i.e., silicon), only the front-side method is acceptable and for cases like water immersion fabrication, the backward illumination method helps the CCD collect more data, thus producing images with better resolution.

During the laser processing, exposure conditions such as pulse energy, repetition rate, scanning speed, beam shape condition (spatio/temporal beam profile), and polarization state have a significant impact on the micro-machined structures. For example, the polarization state of the laser beam is effectively controlled using the combination of a

half waveplate and a polarizer, which is useful for nanostructures formation. Although this schematic is used only for low throughput applications, lower than with parallel processing via micro-lens arrays [62] or spatial light modulator (SLM)[63], it is still suitable for most of research under laboratory conditions.

The movement of the three-axis translation stage is effectively controlled through a home-developed graphical user interface (GUI) based on MatLab, with the GPIB-USB connection being adopted for the communication between the stage controller and a desktop. Multi-function operations (i.e., stage control and machining functions) are integrated in this software, showing significant capabilities for complex structure micromachining.

3.2 Fabry-Perot Interferometer

The Fabry-Perot interferometer (FPI), seen in Figure 3.3, consists of two parallel semi-transparent mirrors separated by a specified distance[64]. This low finesse FP device can be modeled using the two-beam optical interference equation.

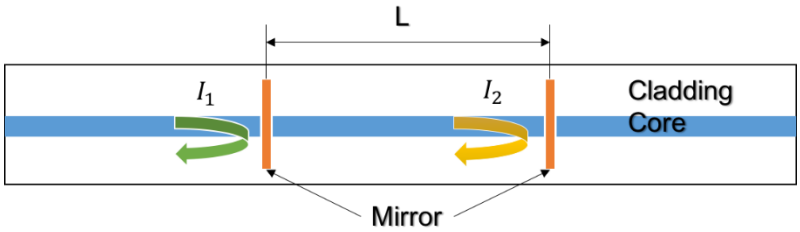

Figure 3.3 Schematic of Fabry-Perot Interferometer

The low finesse FP device can be modeled using two-beam optical interference equation:

$$I = I_1 + I_2 + 2\sqrt{I_1 I_2}\cos\left(\frac{4\pi n \cdot L}{\lambda} + \phi_0\right), \quad (1)$$

where I is the intensity of the interference signal, I_1 and I_2 are the reflections at the cavity end faces, φ_0 is the initial phase of the interference, L is the cavity length, n is the refractive index of the medium filling the cavity, and λ is the optical wavelength in vacuum.

Based on this equation, if the amplitudes of two reflection beams are same, the FPI has the largest fringe visibility and dynamic range, thus improving the signal quality. The interference signal reaches its minimum (I_{min}) when the phase of the cosine term becomes an odd number of π, which can be seen as

$$I = I_{\min}, \text{ when } \frac{4\pi n \cdot L}{\lambda_v} + \phi_0 = (2m+1)\pi, \quad (2)$$

where m is an integer and λ_v is the center wavelength of the valley.

The phase difference of the two adjacent interference minimums is 2π, so we can obtain the optical length of the cavity:

$$L \cdot n = \frac{1}{2}\left(\frac{\lambda_{v1}\lambda_{v2}}{\lambda_{v2} - \lambda_{v1}}\right), \quad (3)$$

where λ_{v1} and λ_{v2} are the center wavelengths of the two adjacent valleys in the interference spectrum. Eq. (3) can be used to calculate either the absolute refractive index (n) or the absolute length (L) of the cavity if one of them is known. The nL term is also known as Free Space Range (FSR)[65].

When transforming the FPI into a refractive index measurement, the relative refractive index change is so small that the phase shift is less than 2π, meaning the phase ambiguity issue can be ignored. The relative refractive index change can be calculated based on the spectral shift of the interferogram. By taking the derivative of n with respect to λ_v, we get

$$\frac{dn}{d\lambda_v} = \frac{1}{4\pi L}. \tag{4}$$

Assuming the cavity length remains constant during the measurement, the refractive index change (Δn) can be calculated based on the wavelength shift ($\Delta\lambda_v$) of a particular interference valley using the following equation derived from Eq. (4):

$$\Delta n = \frac{\Delta\lambda_v}{\lambda_v} n \tag{5}$$

where the relative refractive index change is directly proportional to the spectral shift of the interferogram[66].

The relationship between the relative refractive index change and the spectral shift of the interferogram can be used to compute and examine the stability of the IFPI. In addition, the variation of total power (amplitude) and fringe quality also reflect the stability of the refractive index changes. With the help of powerful fs laser micromachining tools, refractive index fiber optics sensors can be fabricated [67].

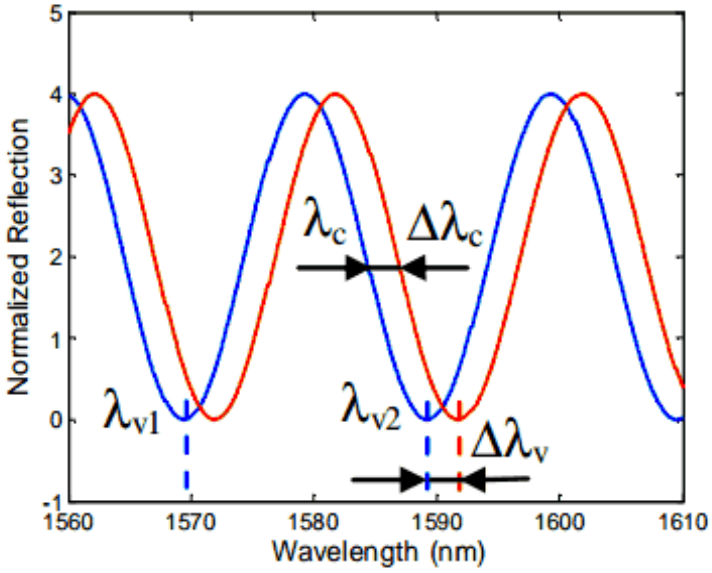

Figure 3.4 The relative refractive index change related with frequency change

3.3 Ferrofluid based optical fiber magnetic field sensor assisted by femtosecond laser ablation

3.3.1 Introduction

Optofluid systems have become increasingly more attractive in such optical sensing applications as chemical and biological analysis as they incorporate unique features from both integrated optics and microfluidics [26]. Recently, various optofluid based structures have been investigated in/on an optical fiber platform referred to as a "lab in/on a fiber." Femtosecond laser micromachining plays an important role in those integrated structures due to its high precision fabrication, flexible design, 3D capability, and compatibility with other methods. Here we present a ferrofluid-based optical fiber magnetic field sensor

fabricated through fs laser irradiation. Using this technique, a micro-reservoir composed of a capillary tube placed between two single mode optical fibers is used to form the two mirrors of the FPI [68]. The side wall of the capillary tube is ablated to generate an open reservoir, which serves as a channel for the ferrofluid, loaded using a syringe pump. The open reservoir is then sealed with UV glue, he UV light illuminating the glue area for 5 minutes to affect the sealing. The refractive index of the ferrofluid varies as the strength of the surrounding magnetic field changes, thus changing the FSR of the FPI.

When measuring the FPI spectrum, the light from a white light source with a range of 1520 to 1620 nm passes through a 50/50 fiber coupler to the FPI; the two reflected beams are bounced backwards and are received by the Optical Spectrum Analyzer (OSA), resulting in a well-formed FPI interference spectrum being displayed on the screen, and as the intensity of the surrounding magnetic field changes, the spectrum shifts. A fringe visibility of up to 30 dB can be achieved with a detection limit of approximately 0.4 Gausses. Because of the fabrication process, micro-reservoirs can be assembled using optical fibers and distinguished through a microwave-photonic interrogation system.

3.3.2 Magnetic Field Senior Review

Magnetic field fiber sensing has attracted increasing attention recently [69]. Ferrofluid, a new type of function material with adequate flow ability and the magnetic property of nanomaterials, is made of ferromagnetic particles in nanoscale and a surfactant suspended in a carrier fluid such as water or oil [70]. When surrounded by a magnetic field, the ferrofluid behaves as a magnet until the field is removed.

In 2013 Gao [71] et al. developed a photonic crystal fiber (PCF) based magnetic field. The ferrofluid was pumped into a PCF connected between two single mode fibers (SMF). The transmission spectrum of the sensor was monitored, the results showing a good relationship between the wavelength shift and the change in the surrounding magnetic field. However, the transmission-based sensor was difficult to install and difficult to assemble. In 2014, Lv et al. [26] proposed a magnetic fluid-filled optical fiber Fabry-Perot sensor for magnetic field measurement, one that improved the volume limitation found in previous work [72]. The Fabry-Perot (FP) cavity was reduced to 32μm in length; however, the package of the ferrofluid could not be precisely controlled. Because of the UV glue used in assembly, an air bubble in the liquid mixture is unavoidable [73]. Here, a mechanically robust magnetic field sensor with flexibility in fabrication is described. In this magnetic sensor, the reflection properties are used for magnetic field sensing, with the FP cavity functioning as the leading optical component. As result, the FP cavity is typically used to obtain the refractive index (RI), pressure or strain measurement. In addition, it has been found to be insensitive to ambient temperature. Femtosecond laser irradiation was used to fabricate the cavity and the fluid injection.

To create a magnetic field, ferrofluid was used to help build a magnetic field fiber optics sensor. Variation in the magnetic field will change the refractive index of the ferrofluid. Optically, when the light propagates inside the fiber, the two end faces of the horizontal cavity will act as two reflectors, and the two reflected waves will generate an interference pattern, referred to as the FP interferometer. The intensity of this interferometer is related to the optical path difference between the two beams. Therefore,

a refractive index change of the cavity medium will result in a spectrum shift of the FP interferometer. This reflection-based probe has the advantage of easy installation. In addition, it can access the testing environment through a single point insertion while a transmission probe requires two access ports, one for input and the other one for output, making it difficult for in situ monitoring applications.

3.3.3 Sensor Structure and Principle

The structure of sensor is shown in Figure 3.5. First, a glass capillary tube 30μm in length is spliced between two standard SMFs, resulting in the cavity formed between the SMFs functioning as an FP cavity. The light from a broadband laser source propagated inside the fiber reflects back at the two end faces of this spliced region. The two reflected beams, denoted I_1 and I_2 generate an interference pattern [68]. The equation for the FP interferometer can be modeled as the two-beam optical interference equation:

$$I = I_1 + I_2 + 2\sqrt{I_1 I_2}\cos\left(\frac{2\pi \cdot OPD}{\lambda} + \phi_0\right), \quad (1)$$

Where I is the intensity of the interference signal; ϕ_0 is the initial phase of the interference (usually equal to zero), and λ is the optical wavelength in vacuum. The round-trip optical path difference (OPD) of the FP interferometer is given by

$$OPD = 2n_{cavity}L, \quad (2)$$

where n_{cavity} is the RI of the cavity medium and L is the cavity length. The wavelengths of the valleys in the spectrum are represented by the following equation:

$$\frac{4\pi n_{cavity} L}{\lambda_m} + \varphi_0 = (2m+1)\pi \quad (3)$$

where m is an integer and λ_m is the wavelength of the mth order interference valley [26]. The distance between two adjacent valleys of the spectrum, defined as the free spectrum range (FSR), where m = 0 in equation (3), can then be expressed as

$$FSR = \frac{\lambda^2}{2n_{cavity} L} \quad (4)$$

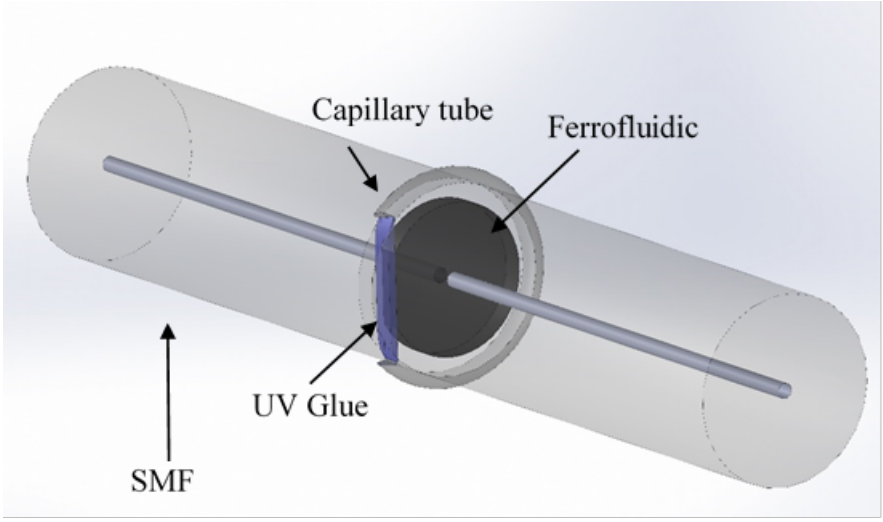

Figure 3.5 The structure of sensor probe

In this sensor, Ferrotec- Oil-based Ferrofluid EMG 909 was loaded into the FP cavity [26]. The Δn_{cavity} follows the equation:

$$\Delta n_{cavity} = a_H \Delta H + a_T \Delta T, \quad (4)$$

where the Δncavity is the refractive index change when filled with ferrofluid, aH is the magnetic sensitivity of the ferrofluidic, and aT is the temperature sensitivity. The thermal expansion can be ignored as the experimental environment was held at a constant

temperature of 21˚C in the laboratory. Therefore, the resonance wavelength shift of the interference spectrum is related to only one term:

$$\Delta\lambda_m = \lambda_m \cdot a_H \Delta H \tag{5}$$

When the magnetic field changes, the entire spectrum will shift, depending on the magnetic sensitivity of the ferrofluid. Monitoring the single valley of the spectrum shift over the magnetic field correlates the relation between the sensor and the magnetic field.

3.3.4 Experiment Setup

To assist the injection of ferrofluid into the FP cavity, femtosecond laser micromachining was used to drill a hole into the side of the capillary tube. Figure 3.6 shows the system of the Ti:sapphire fs laser with a central wavelength of 800 nm, a pulse width of 200 fs, and a laser repetition rate of 250 KHz. While the maximum output power of the laser was 1 W, the actual power used for fabrication was controlled by adjusting the laser beam optics, which include a half-wave plate, a polarizer, and several neutral density (ND) filters. A beam shutter (Thorlabs, Co.) was used for switching the laser on and off. The actual pulse energy for fabrication in this experiment was 0.3 μJ, as measured by a power meter.

An SMF-28e (Corning Co.) optical fiber with a core diameter of 8.2μm and a cladding diameter of 125μm was used in this experiment, and the capillary tube used was a glass tube with an OD of 164μm and an ID of 100μm. Both the fiber and the tube were

mechanically stripped of their buffer and cleaned with acetone. First, an SMF was spliced with a capillary tube, after

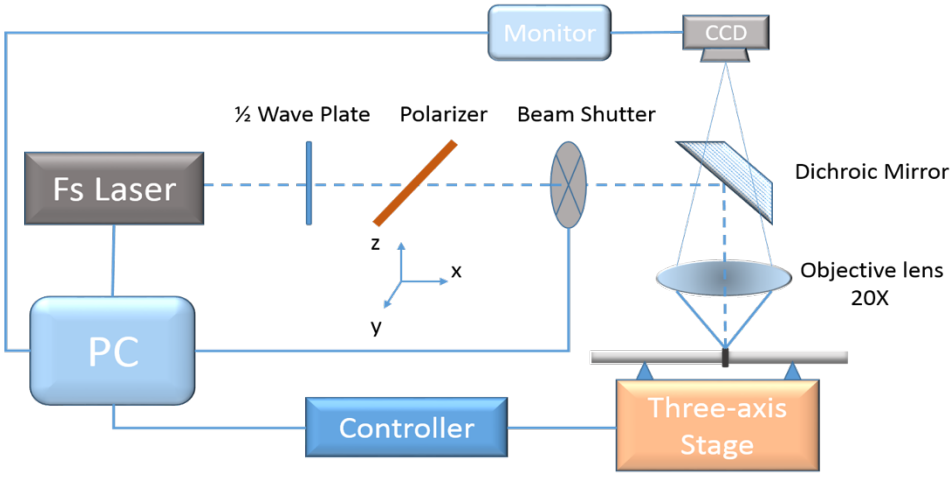

Figure 3.6 Femtosecond laser micromachining system

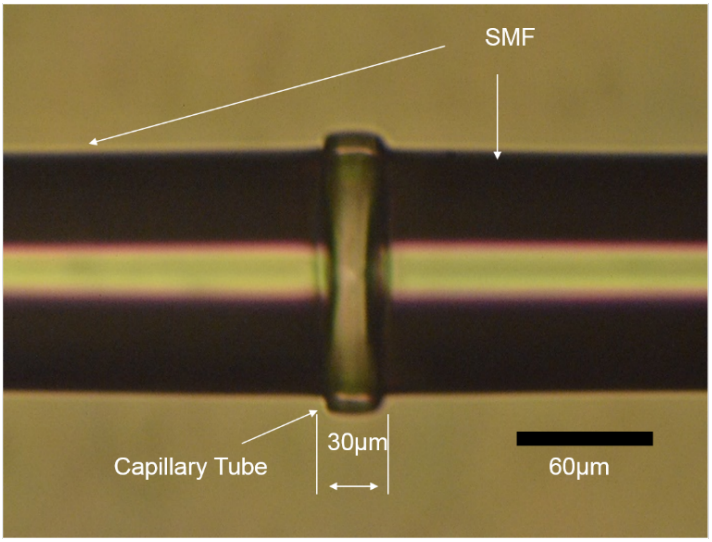

Figure 3.7 The assembly before ablation

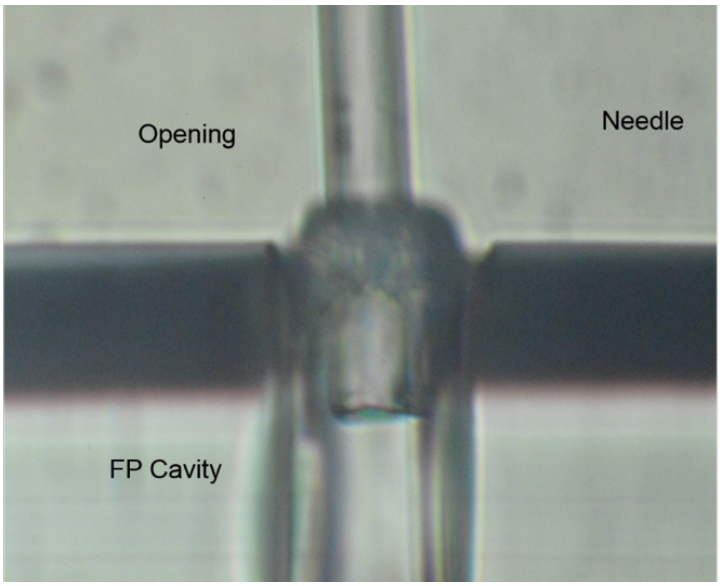

Figure 3.8 The assembly after fs ablation with needle

which this spliced fiber-tube structure was mounted into the home-made cleaving system. An online monitoring system was used to facilitate this mounting of the cleaver to the connection area of the fiber tube. The translation stage holding the cleaver was moved 30 μm away to leave a tube length of 30μm, a reasonable length allowing the tube to hold the ferrofluid and minimize the loss as the reflected beam passed through the ferrofluid. Finally, a second SMF was spliced to the other side of the tube to form the second reflection mirror as shown in Figure 3.8. The splicing parameters and the splicing time were well tuned to help maintain a flat end-face at the fiber tube connection area.

The FPI cavity was created by the fiber-tube-fiber structure with the help of the fusion splicer and the precisely controlled home-made cleaving system. Then, fs laser micromachining irradiation was applied to drill a hole on the side of the tube for loading the ferrofluid into the cavity to allow the FPI to perform the magnetic field sensing function.

A ~30 x 30 μm square shape open hole, was needed for this research to ensure the pump needle could be inserted into the FP area. The assembly was clamped horizontally onto two fiber holders (Newport 561-FH). Then the fabrication was processed in air, the laser beam moving from the capillary tube surface to its center from the top to the bottom. Next , a rectangular region with dimensions of 30×60×40 μm was inscribed on the capillary tube, and the fs laser irradiation swept from the top to the bottom. The total number of layers of sweep was 40, an opening appearing on the specified region. A capillary tube (with OD 150 μm and ID 100 μm) was tapered to smaller than 20 μm to ensure insertion into the tube.

Assisted by the microscope and a manual three-dimensional stage, the needle was inserted into the cavity though the opening as shown in Figure 3.8. The speed of the syringe pump was set as 1milliliter per second. The ferrofluidic, EMG 909 from Ferrotic, has a low viscosity of 3 cP (at 27˚C) and a saturation magnetization (Ms) of 220 Gauss. The loading process stopped when the cavity was filled with the liquid as indicated by the microscopic monitoring. Subsequently, the open cavity was sealed with UV adhesive. The entire device was exposed in UV light to help shorten the UV glue solidifying time. Finally, the tail of the SMF was cut to the minimum length to reduce the device length and prevent it from bending.

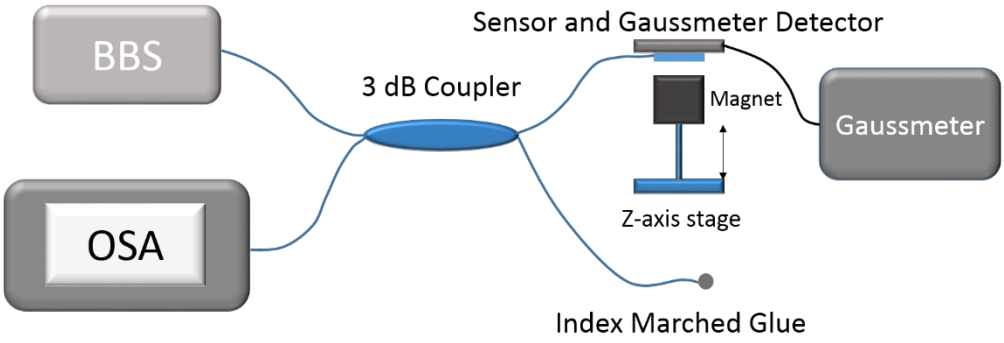

Figure 3.9 The sensing system of FP strucure

The packaged optofluidic device was interrogated by a broadband light source with a wavelength ranging from 1520 to 1620 nm. This light was routed by a 3dB coupler, and the interference spectrum was detected using an optical spectrum analyzer (AQ6319). Figure 3.9 shows the sensing system of the FP structure. The magnetic field was generated by a 20mm*20mm*20mm rectangle magnet. The detector of the Gaussmeter was placed parallel and tightly against the sensor to ensure precise magnetic field intensity detection. The range of magnetic field intensity applied was from 60 to 180 Gs.

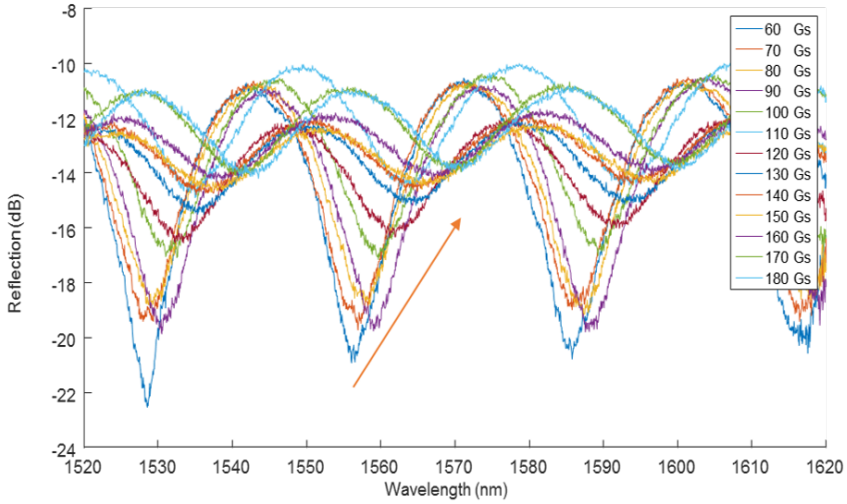

Figure 3.10 The reflection spectrum of magnetic field sensor in magnaetic field from 60Gs to 180Gs

3.3.5 Result and Discussion

From the OSA record, the dimension of the FP cavity can be calculated using the FSR equation shown above. Its measured length was 32μm. Figure 3.10 shows the interference spectra of this ferrofluidic-based magnetic field senor under magnetic fields of different intensities. As the magnetic intensity increased, the interferogram shifted toward the longer wavelength region. Figure 3.11 shows the spectrum valley shift from 60Gs to 180Gs. The linear relationship between the magnetic field intensity and the wavelength confirmed the experimental principle. The ratio was calculated under this range, with a ratio of 0.121Gs/nm being referred to as the sensitivity. Similar results have been obtained from sensors with a 50μm cavity length.

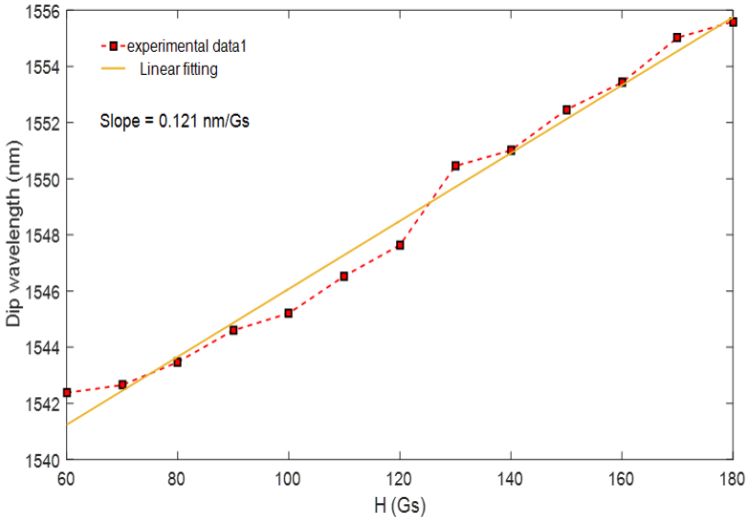

Figure 3.11 Transmission spectrum at different magnetic field

3.3.6 Conclusion

In summary, a ferrofluid-based optical fiber magnetic field sensor was fabricated through fusion splicing and fs laser ablation. The structure was easy to make and the FP cavity generated high fringe visibility. With the function material (e.g., ferrofluid) loaded, this cavity was sensitive to changes in the surrounding magnetic field, the wavelength shifting linearly, and the sensitivity was calculated as 0.121 Gs/nm, i. e., high sensitivity. The proposed sensor was novel in structure design and fabrication. This sensor exhibits impressive advantages in magnetic field sensing, making it particularly applicable to harsh environments.

3.4 An Intrinsic Fabry-Perot Interferometry (IFPI) Temperature Sensor with Self-strain-compensation Function

3.4.1 Introduction

Optical fiber based sensors have been the focus of much research on sensing various physical quantities, including temperature, strain, pressure, and biochemical quantities like intracellular pH, and chemical concentration, among others [74]. A variety of optical fiber sensor structures as well as sensing mechanisms have been investigated over the past two decades, one example being the FP interferometer. FPI sensors can be subcategorized into two types, extrinsic Fabry-Perot Interferometers (EFPI) and intrinsic Fabry-Perot Interferometers (IFPI). EFPI is able to facilitate direct wave-matter interaction, while IFPIs are used for stability, all-in-fiber flexibility and lower insertion loss. Because of their unique features, IFPIs are advantageous for sensing in harsh environments.

In the past, several types of distributed sensors with cascaded FPIs have been developed, their primary tracking method based on demodulating the multiplexed interferometers through fast Fourier transform (FFT). A quasi-distributed IFPI sensing system demultiplexed with an FFT-based wavelength tracking method developed early [75] was used to demodulate the temperature information applied to all IFPIs. Frequency components corresponding to each sensor were extracted from the transmission spectra and then transformed back to the wavelength domain [76]. The experimental results of these multiplexed IFPI sensors exhibited high reliability in their wavelength tracking methods based on their temperature sensitivity [77]. More recent research has reported a sensor using cascaded EFPIs and IFPIs as temperature and pressure sensing elements. These

sensing systems can measure temperature and pressure unambiguously, confirming the viability of wavelength tracking methods. However, they detected single varying quantities and analyzed the sensitivity assuming no cross talk from other changing parameters at the sensing area.

In this section, a temperature sensor system with strain self-compensation is presented. A dual-parameter sensing design using cascaded IFPI structures addressed the issue from temperature-strain cross talk. To achieve the high quality optical structure needed inside the fiber, femtosecond laser micromachining was employed to fabricate the IFPIs. This ultra-fast laser delivers high-intensity energy to the core of the SMF effectively changing the refractive index in the inscribed region. During the fabrication, the intact polymer buffer coating of the SMF is not striped off [78], significantly enhancing the mechanical prosperity of the sensor. A pair of IFPIs of different cavity lengths including the main sensor and the compensation sensor comprise this sensor system.

3.4.2 Demultiplex Principle

IFPI is sensitive to temperature due to the combination of the thermo-optic effect and thermal expansion of the fiber material. In addition, it is strain sensitive because of the variation of refractive index (RI) and the optical length changing simultaneously with physical length of the sensor changing under stretch[79]. Strain-induced effect is defined by Young's modulus multiplexing the stress. Therefore, temperature and strain variation are independent variables to the IFPIs because temperature change will not significantly

affect the Young's modulus that could be ignored. Specifically, the laser ablated cavity-mirrors reflect the guided

$$I = I_1 + I_2 + 2\sqrt{I_1 I_2}\cos\left(\frac{2\pi \cdot OPD}{\lambda} + \varphi_0\right) \quad (1)$$

where I is the intensity of the interference signal; φ_0 is the initial phase of the interference (normally equal to zero), and λ is the optical wavelength. The round-trip optical path difference (OPD) of the FP interferometer is given by

$$OPD = 2n_{cavity}L \quad (2)$$

where n_{cavity} is the RI of the cavity medium and L is the physical cavity length of each IFPI. At the valleys in the interferogram in spectrum domain, the phase difference of the two light beams satisfies the condition of destructive interference:

$$\frac{4\pi n_{cavity}L}{\lambda_m} + \varphi_0 = (2m + 1)\pi \quad (3)$$

where m is an integer and λ_m is the wavelength of the mth order interference valley. [7] The distance between two adjacent minima of the spectrum, defined as the free spectrum range (FSR), can then be expressed as

$$FSR = \frac{\lambda^2}{2n_{cavity}L} \quad (4)$$

In this sensor system, the compensate IFPI sensor has wavelength shift as a function strain as

$$\Delta\lambda_\varepsilon = (-P_{eff} + 1)\varepsilon \cdot \lambda_m \quad (5)$$

where P_{eff} is the effective strain-optic coefficient, approximately 0.204 for fused silica materials. From the Eq. 5, the strain sensitivity is dependent on the interrogated wavelength and the effective strain-optic coefficient.

the wavelength shift caused by temperature variation around main IFPI sensor can be expressed as the equation below,

$$\Delta\lambda_T = (\alpha_{CTE} + \frac{d_n}{d_T}) \cdot \lambda_m \cdot \Delta T \quad (6)$$

where a_{CTE} and $\frac{d_n}{d_T}$ are the thermal expansion coefficient and thermal-optic coefficient of the material[80], respectively. For fused silica material, the CTE is 0.55×10^{-6}/°C and the thermo-optic coefficient is approximately 7×10^{-6}/°C. Based on Equation (5) and (6), the temperature-strain cross talk of the main IFPI sensor is given by

$$\frac{\mu\varepsilon}{\Delta T} = \frac{\Delta\lambda_T/\Delta T}{\Delta\lambda_\varepsilon/\mu\varepsilon} = \frac{(\alpha_{CTE}+\frac{d_n}{d_T})\cdot10^6}{-P_{eff}+1} \quad (7)$$

The calculated result of the temperature-strain cross talk for the main IFPI sensor is 9.57 με/°C[81].

In general, the wavelength shift of the sensing system can be expressed as,

$$\Delta\lambda_{compensate} = K_\varepsilon \times \mu\varepsilon$$

and (8)

$$\Delta\lambda_{main} = K_\varepsilon \times \mu\varepsilon + K_T \times \Delta T$$

where $K_\varepsilon$is the coefficient of strain-induced effect and K_T is the coefficient of temperature-induced effect[82]. The strain and temperature can be obtained by solving the following matrix[83]

$$\begin{bmatrix}\Delta T \\ \mu\varepsilon\end{bmatrix} = \frac{1}{\mathrm{A}}\begin{pmatrix}K_\varepsilon & -K_\varepsilon \\ -K_T & 0\end{pmatrix}\begin{bmatrix}\Delta\lambda_{compensate} \\ \Delta\lambda_{main}\end{bmatrix} \quad (9)$$

where A=$-K_\varepsilon \cdot K_T$.

The interference signal of the sensing system is multiplexed. The OPD of the two IFPIs can be resolved by performing the Fourier transform on the recorded interferogram. A broadband light source with a range of 1520 to 1620 with a minimum detectable OPD change of 12⌈m is used here. As reported in early research, a wavelength tracking method based on FFT has been used to improve the measurement accuracy and demodulate multiplexed signals. Demodulation of the IFPIs spectrum signal begins by distinguishing the two IFPI free spectrum ranges in the frequency domain through FFT. Then band-pass filters are used to extract two separate frequency components and to determine the inverse FFT [84]. The individual wavelength domain spectrum obtained is used to track the wavelength shift for each IFPI.

3.4.3 Sensor Design and Fabrication

The sensor consists of two pairs of low reflectance cavity-mirrors that form two cascaded IFPIs. Each reflector is created by laser micromachining in the core of a single-mode fiber (Corning SMF-28e). The cavity length of main IFPI sensor is 100μm and the so called compensate one is 500μm.

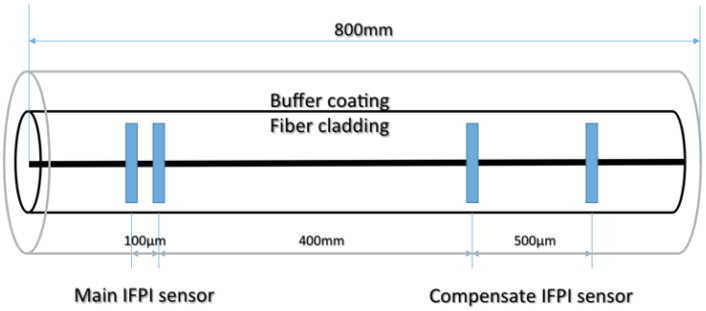

Figure 3.12 Cascaded IFPI sensor system structure

Figure 3.12 shows the sensor structure along with the dimensions. The four low reflectance mirrors are 15μm in width, 15μm in height and 1μm in thickness. The distance between the two IFPIs is 400mm to ensure that the temperature changes only around the main IFPI sensor. The total mounted length of fiber is 800mm. In practical applications, the dimensions are flexible and able to be designed as needed. As mentioned previously, both IFPIs are sensitive to temperature and strain.

In the case of the stripped-off fabrication, the bare fiber lacks mechanical properties and breaks easily, meaning it is not robust for experimental or other harsh environments. Its pliability is reduced due to the loss of integrity even with a recoating process [85]. Therefore, the engineering challenge in this sensor is to retain the acrylate buffer coating during fabrication with no damage to it. Improper use of laser power and poor focal delivery results in melting the polymer coating and defocusing the laser beam.

To assist the fabrication of IFPIs in SMF, FS laser micromachining was used. The fabrication system remained the same with a Ti: sapphire fs laser with a central wavelength of 800nm, a pulse width of 200fs, and a repetition rate of the laser of 250 KHz. The maximum output power of the laser was 1 W, with the actual power used for fabrication being controlled by adjusting the laser beam optics, which included a half-wave plate, a polarizer, and one-linear neutral density filters. A beam shutter (Thorlabs.) was used for switching the laser on and off. The actual pulse energy for fabrication in this experiment was 0.32 μJ. The fs laser beam was focused into the fiber through an oil immersion objective lens (Olympus. UMPLanFX 100X) with a numerical aperture (NA) of 1.3. The entire cross section of the fiber core was covered by a cuboid region of 15*1*15μm

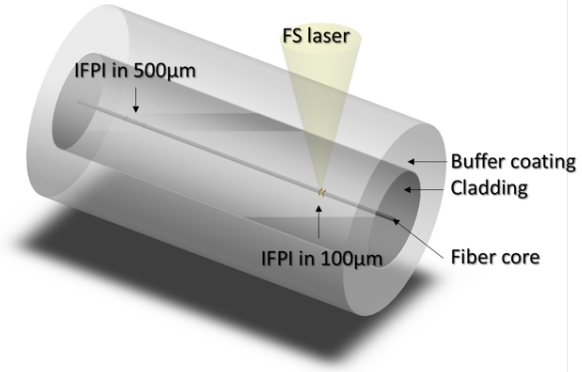

Figure 3.13 Schematic od the fs laser fabrication

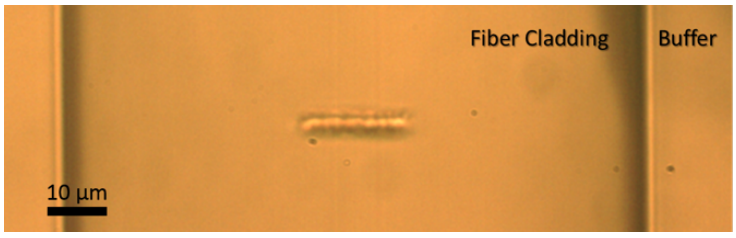

Figure 3.14 Micrograph of the inscribed region

inscribed in the center of the fiber from the bottom up. The scanning speed was 20⌈m/s. Figure 3.13 shows the schematic diagram of the fabrication with the buffer intact and the micrograph of the inscribed region which forms a low reflectance mirror.

Refractive index matching oil (Type A. Cargille) with low viscosity and a refractive index of 1.46 was used as the transparent immersion medium [86]. In oil immersion, the aspect ratio value of the laser spot is significantly higher than it is in water immersion. This ratio value depends on the NA, a value that can be obtained only with oil/water immersion objectives where the lateral spatial resolution is less than 100 nm. The large NA due to the high refractive index of matching oil helps to improve the aspect ratio of the inscribed region. More importantly, it prevents heat absorption and melting in the acrylate buffer coating more effectively.

3.4.4 Experimental Result

In the experiment, one side of the strain sensor system was mounted on a moto-driven one-axis stage (Newport) and the other side on a fixed post. The stage has an axis resolution of 50nm, the specified length of movement controlled by its software. Applied strain occurs when the stage move outwards until the fiber is tight. Figure 3.15 shows the experiment setup including the strain and temperature environment. For the main IFPI sensor temperature test, a hotplate with a thermal couple heated a water bath from 30-90˚C as the acyclic buffer coating will not survive at high temperature due to its low melting points. The distance between the two IFPIs was 400mm and the total length of fixed optical

fiber is 800mm. This cascaded sensor system was interrogated by a broadband light source, with a wavelength range from 1520 to 1620 nm. The light was routed by a 3dB coupler, and the interference spectrum was detected by an optical spectrum analyzer (AQ6319).

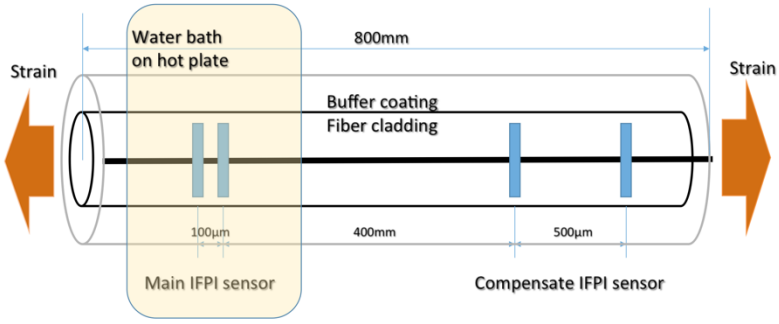

Figure 3.15 Schematic of the experiment set up

Figure 3.16 shows the recorded spectrum of multiplexed sensing signal in air and the demodulated result after FFT. The waveform domain signal has a high fringe visibility of 7dB. Since the recorded signal is in wavelength axis and only the wave number axis spectrum is suitable for FFT, the LINSPACE function in MATLAB library was used to arrange the sampling points from the wave domain spectrum at equal intervals. In Figure 3.17, two space frequency components with substantially different OPDs can clearly be seen. To select the individual frequency domain component, Hanning-windowed digital filters were used in FFT to plot the result. Next, the filtered result was transferred back to the wavelength spectrum. Figures 3.18a and b show the reconstructed waveforms of two the IFPIs, respectively. Once we have the individual interferogram of the two IFPIs, the

tracking wavelength can be selected from a specific interference dip in the reconstructed spectrum. Later, the waveform shift is obtained from this tracking method.

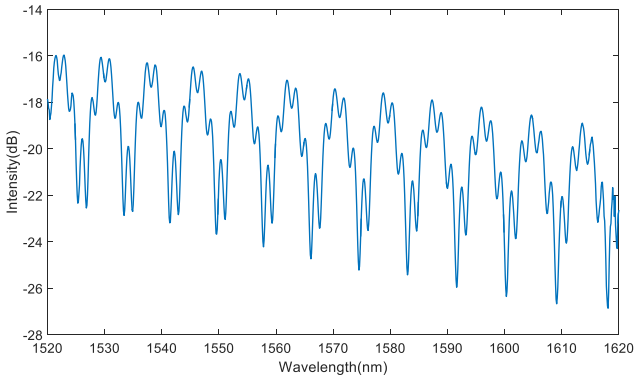

Figure 3.16 Recorded spectrum of cascaded IFPI sensors

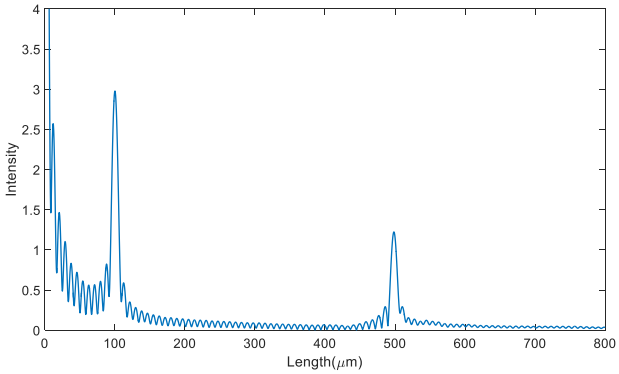

Figure 3.17 FFT result of the multiplexed sensors

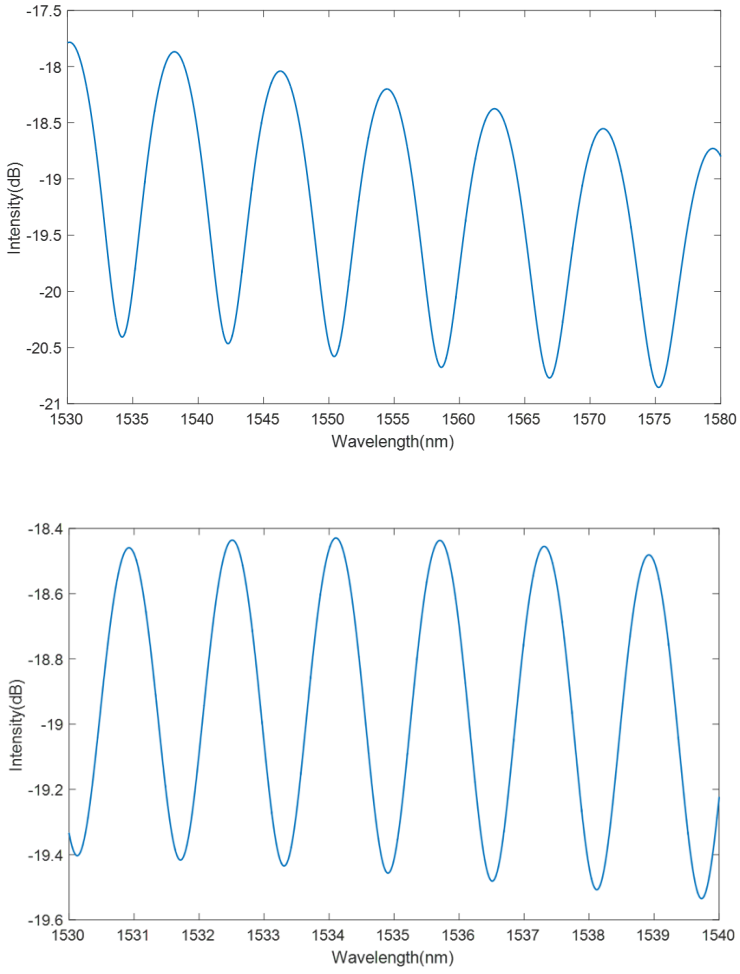

Figure 3.18 Reconstruction of wavelength signal of (a). main IFPI sensor in 100μm (b). compensate IFPI sensor in 500

The first experiment calibrated the temperature response of the main IFPI sensor. A water bath was heated on a hot plate (Corning) with a thermal couple indicating the temperature change from 30-90˚C at every 10˚C step. The fiber was loose in the sensing area with no strain exerted. In theory, the compensate IFPI sensor should not indicate a wavelength shift.

The dynamic measurement result of the sensor system provides individual results for the temperature sensitivity and the strain self-compensation. In dual varying parameters, the main IFPI sensor gives the wavelength spectrum shifts from the combined impact of temperature and strain. The temperature effect is refined by linearly subtracting the strain information from the main sensor signal. Figure 3.19 shows a dip in the reconstructed spectrum shifting from the compensate IFPI sensor between 1534nm and 1536nm, and Figure 3.20 shows the strain-induced response. The initialized position of the strain text is set once the fiber is tight. According to the calculation of temperature-strain cross talk in principle, a strain from initialization to an additional 600 μm at 100 μm step is exerted. Simultaneously, the temperature test on the main IFPI sensor is run again. The number of sampling points in the strain test matches the number in

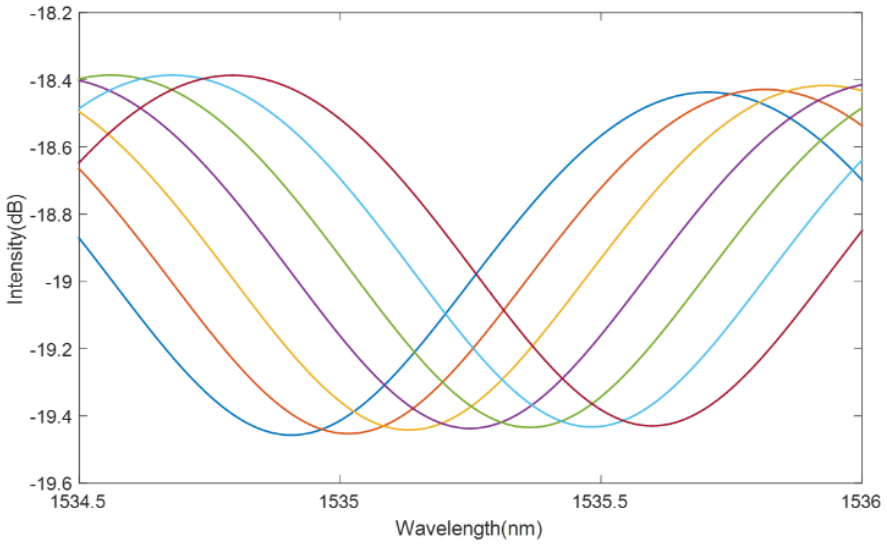

Figure 3.19 Compensate IFPI sensor waveform shifts to the longer wavelength range.

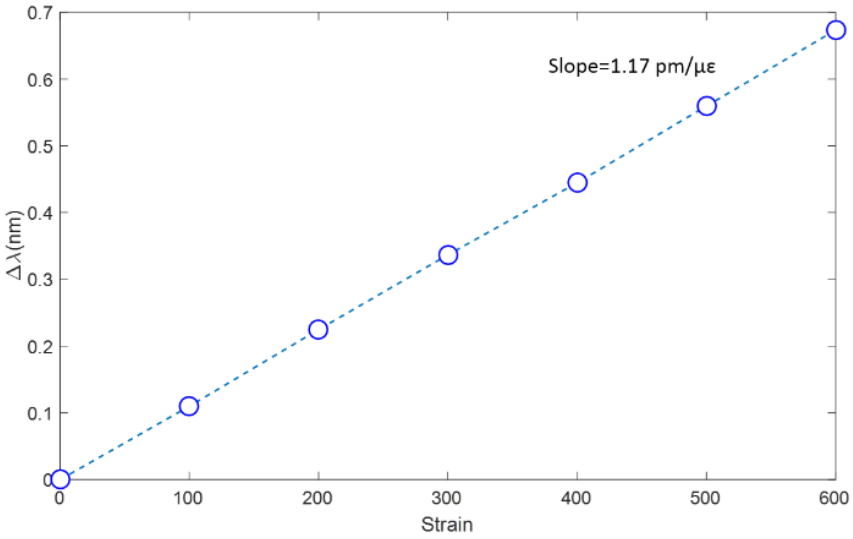

Figure 3.20 Strain test result with slope in 1.17pm/με.

the temperature test. In Figure 8b, the compensate IFPI sensor spectrum shifts towards the longer wavelength under increasing strain linearly and the response slope is 1.17 pm/με.

For the main IFPI sensor, the waveform seen in Figure 3.21 shifts similarly to the longer wavelength range co-responding to the dual parameters. The plotted results of the linear relationships in Figure 3.22 show the wavelength shift information from the main IFPI sensor before and after compensation. The strain-induced effect is removed from the recorded spectrum by linearly subtracting the spectrum in Figure 8b from the main result. The calibration of the temperature response in the main IFPI trends linearly with slopes of 11.12 pm/˚C provided from the first experiment. The compensated slope with a sensitivity of 11.33 pm/ ˚C is in full accord with the temperature calibration. The result shows that the temperature sensor system has analogous self-compensated sensing capability by interfering with the strain.

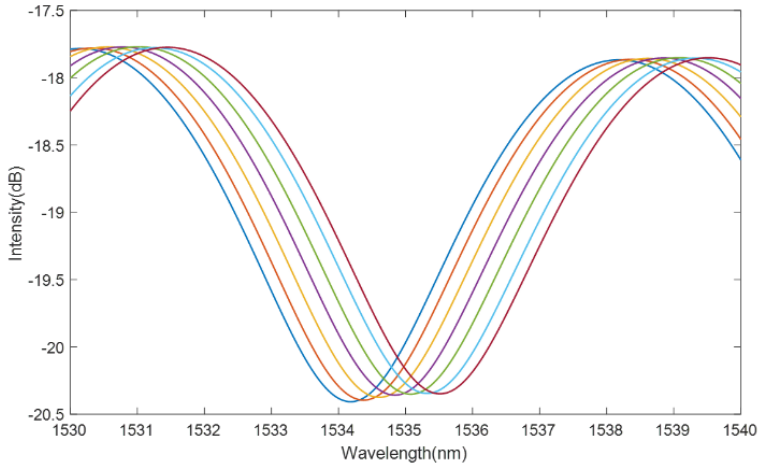

Figure 3.21 Main IFPI sensor waveform shifts to the longer wavelength range.

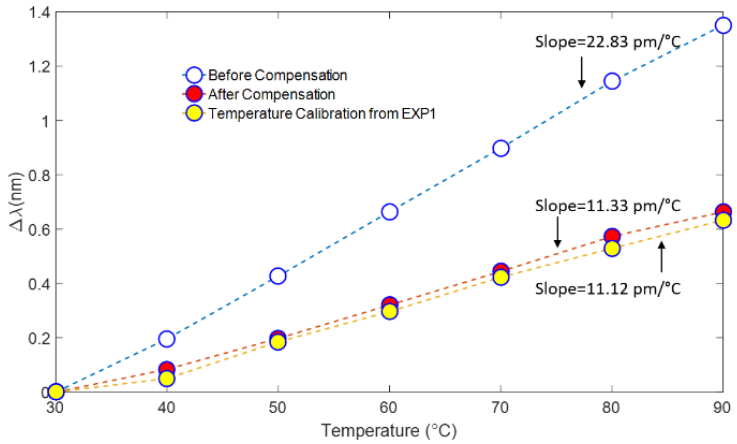

Figure 3.22 Test result before compensation in blue line. After compensation by linearly subtracting the strain information, the result of spectrum matches the temperature calibration from experiment 1.

3.4.5 Conclusion

An IFPI-based temperature sensor system with strain self-compensation fabricated by FS laser micromachining was developed in this study. The experimental results indicate that temperature information is completely refined based on the FFT-based wavelength tracking method. The reconstructed spectrum of the main IFPI sensor was analyzed using

the temperature-strain cross talk calculation, the results showing that the cascaded IFPI sensors have a temperature sensitivity of 11.33 pm/ ˚C with interference from the dynamic strain variation. The sensor system also has a linear response of strain of 1.17 pm/⌠∑ provided by the compensate IFPI sensor. The sensing performance was the same for both the single or multiple parameters. These results indicate that the temperature sensor system developed here is similar to the theoretical analysis in terms of the sensitivity and measurement resolution. The fabrication method used here effectively improved the quality of the inscribed region and kept the buffer coating of the fiber intact, thus enhancing the robustness of the sensor system.

CHAPTER FOUR

OCIM ASSISTED IN-SITU WEAK REFLECTOR FABRICATION

From the previously developed sensor measurement system, we obtained a dynamic measurement sensitive to temperature and strain. The sensor was fabricated in SMF, with the interference spectrum being detected by an optical spectrum analyzer, from which we could monitor and estimate whether the reflectivity of the paired mirrors is balanced, meaning that the in-situ case remains indirect; however, what about the MMF and the cascaded cavities with more than 2 pairs and a longer cavity length? So the question becomes is it possible to control and monitor the reflectivity of a single reflector? And the answer is yes.

In this chapter, an incoherent optical carrier based microwave interferometry (OCMI) technique is utilized for in-situ weak reflector fabrication using femtosecond laser micromachining. We propose to use this technique for optical fiber in-situ fabrication for SMF, MMF, and cascaded or longer FP cavities. The balance of reflectance for FP cavity directly affects the signal quality for power-based sensing. The OCMI provides the opportunity to monitor the reflectance of each reflector. Multiple laser parameters and related environmental aspects may affect the refractive index modification under certain conditions. Therefore, a careful step-by-step creation of the mirrors is necessary with assistance from the OCMI and fs laser micromachining system.

4.1 Incoherent optical carrier based microwave interferometry (OCMI) technique

The incoherent optical carrier based microwave interferometry (OCMI) technique has fully distributed sensing capability with high spatial resolution and a large measurement range. This system uses a microwave modulated incoherent (broadband) light source to interrogate cascaded intrinsic Fabry-Perot interferometers formed by adjacent weak reflectors inside an optical fiber [79]. When the distance between the two adjacent reflectors is larger than the coherence length of the light source, the optical interference components in the received signal becomes zero, and the microwave terms are processed to form a microwave interferogram, which is further analyzed to calculate the optical path difference between any two reflectors along the fiber. This method has a number of unique advantages including high signal quality, relieved requirements for fabrication, low dependence on the types of optical waveguides, insensitivity to the variations of polarization, high spatial resolution, and fully distributed sensing capability [87].

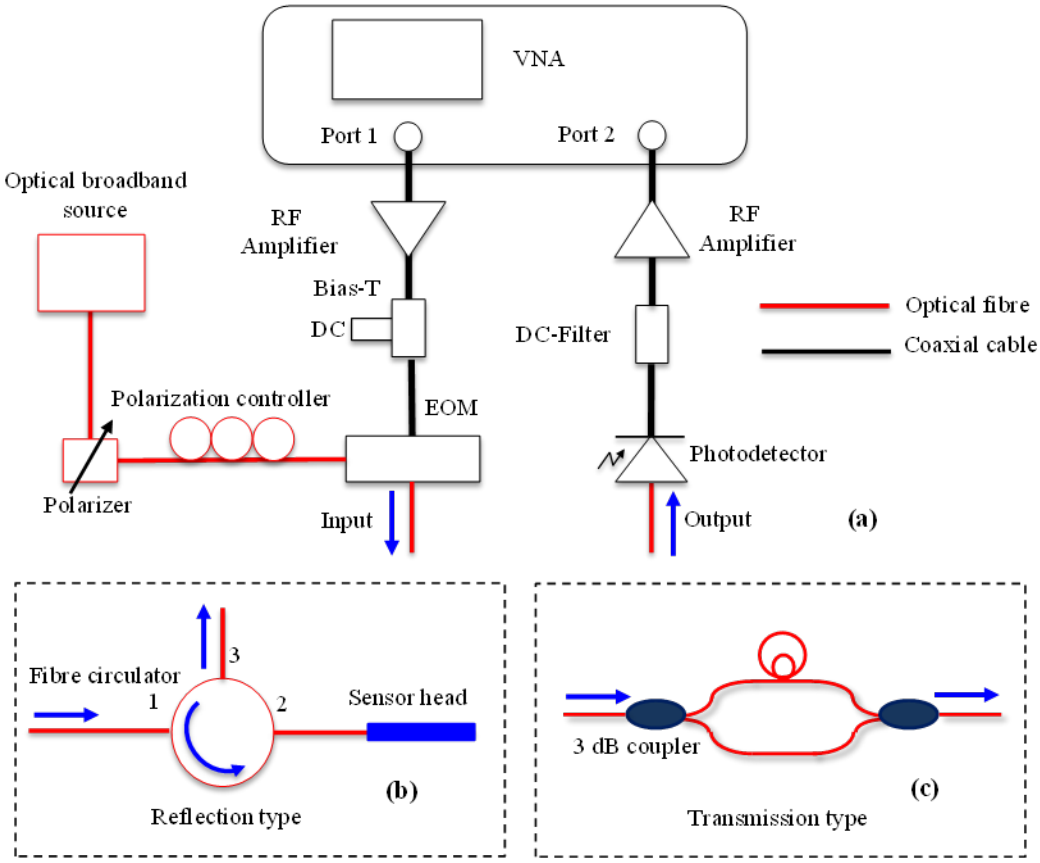

Figure 4.1 Schematic of OCMI system

First, the light from the broadband source (BBS) is intensity modulated by a microwave signal through an electro-optic modulator (EOM)[88]. An in-line fiber polarizer and a polarization controller followed by the light source are used to optimize the modulation depth of the EOM, which is driven by Port 1 of the vector network analyzer (VNA). The microwave-modulated light, for which the optics is the carrier and the microwave is the envelope, emits from the EOM and then couples into a 2×1 fiber coupler (a circulator also works). The cascaded fiber interferometers are connected to one lead of the fiber coupler. The interferometers can be a reflection type (as shown in Figure 4.1(b))

such as a cascaded FPI, a Michelson type interferometer, or a transmission type (as shown in Figure 4.1(c)). The light from the interferometer is then detected by a high-speed photo-detector, which converts the optical signal into an electrical signal. This electrical signal is then recorded by Port 2 of the VNA. The VNA is referred to as voltage ratio measurements where a swept continuous wave (CW) source in a microwave band is tracked by a transmission receiver and the results are displayed as scattering parameters S_{21}.

The amplitude and phase spectra of the scattering parameter (S_{21} in this illustration) obtained from a Michelson-OCMI based two reflection optical fiber sensing system are shown in Figure 4.2 (a) and (b), respectively. The time domain response of the system can be obtained by applying an inverse discrete Fourier transform (IDFT) to the complex S_{21}. Figure 4.2 (c) shows the amplitude spectrum of the calculated time domain response where the two main pulses indicate the reflections from the fiber ends of the two sensor arms. The other pulses shown in the time domain amplitude spectrum may be caused by multiple reflections at the fiber ends. Those small pulses in the time domain contribute to the ripples on the amplitude spectrum shown in the inset of Figure 4.2 (a). One way to eliminate these ripples is to add a time domain gate on the TDR signal to select the two main reflections and suppress other unwanted signals as shown in Figure 4.2 (c) and then apply a discrete Fourier transform (DFT) [89] to the filtered signal to reconstruct its frequency spectrum. The amplitude spectrum of the reconstructed signal is shown in Fig 4.2 (d) where the inset shows the zoomed in spectrum. A distance change between the two pulses would show as a readable shift in the reconstructed spectrum.

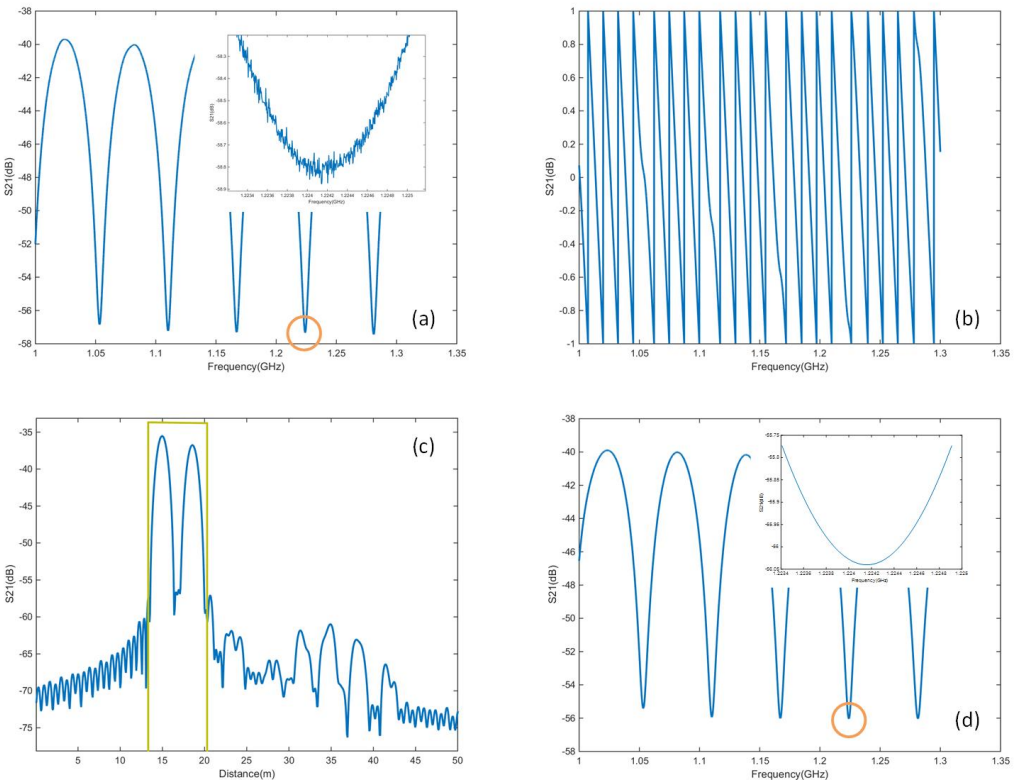

Figure 4.2 (a) Amplitude spectrum of the original S21; (b) phase spectrum of the original S21;(c) time domain signal got from S21 through the IDFT; the rectangular gate indicates the time domain band pass filter; (d) amplitude spectrum of the filtered S21

In summary, this technique uses the optics as the carrier and reads the optical interference information in the microwave domain. For cascaded FP cavities along an optical fiber, a photodetector is used to demodulate the light wave, then send the reflectance information to the vector microwave detector. Each pulse in the time domain represents the time delay for the light wave to pass through the respective path, and the distance between them is proportional to the optical length difference between the two paths.

After we applied the inverse Fourier transform, we obtained a clear time domain spectrum. We can see very sharp pulses, the amplitude and the locations of each

corresponding to the reflectivity and locations of these reflectors. By adopting the OCMI technique, the phase of the microwave, which can be used to locate each reflector, is easily recorded.

4.2 In-situ Fabrication Process Using OCMI System

With assistance from the OCMI system, in-situ fabrication of individual reflectors can be realized. We propose to use it for optical fiber in-situ fabrication of SMF, MMF, cascaded or longer FP cavities.

From the bottom to the top of the fiber core, the intensity changes essentially follow the same pattern. The highest peak occurs before the center, dropping soon after as shown in Figure 4.3. This trend is explained by mode distribution, the laser beam shaping corresponding to the imaging system of the laser setup. Based on experience, when we find the highest point, the re-scanning and surface polish around these areas contribute to improving the intensity. On the other hand, if the reflectance is over the value matching the others, we keep scanning towards the dropping area. In order find the highest peak value or the value needed to balance the sensing system, the fabrication procedure was sliced into lines forming a vertical mirror wall crossing the fiber core. The building process is terminated once the OCMI system tested the reflectance needed.

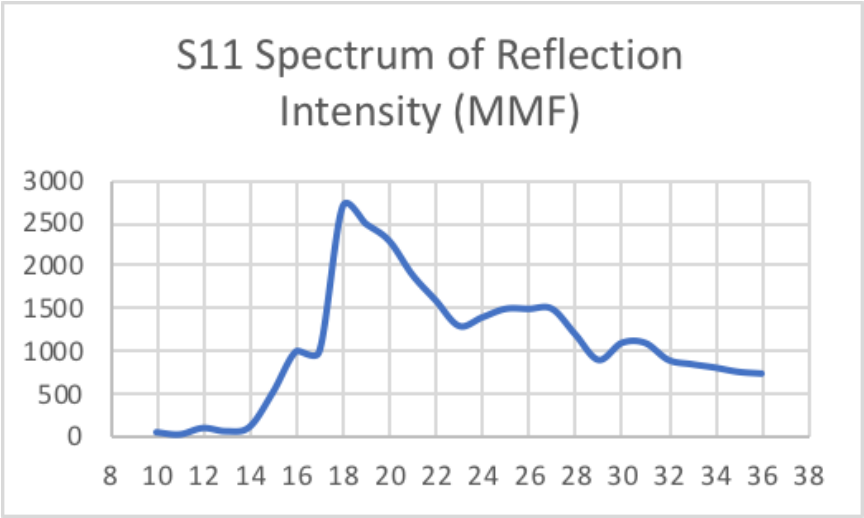

Figure 4.3 S11 Spectrum of reflection intensity of MMF during fabrication

More specifically, we used the fs laser micromachining system to fabricate the reflectors in the MMF for distributed strain sensor preparation. The central wavelength, pulse width, and repetition rate of the laser were 800 nm, 200 fs, and 250 kHz, respectively. The maximum output power of the laser was 1 W. The actual power used for fabrication was controlled by adjusting the laser beam optics, which included a half-wave plate and a polarizer. The laser was switched on or off by electrically gating the internal clock. The actual laser energy used for fabrication was approximately 0.4 μJ per pulse.

The fiber used in the experiments was a 10 meter long grade index MMF (Corning 62.5/125 Optical Fiber). It was cleaned using acetone and clamped onto two bare fiber holders (Newport 561-FH). The optical fiber and fiber holders were then immersed in distilled water during fabrication. The fiber assembly was mounted on a computer-controlled three-axis translation stage (Newport, Inc.) with a resolution of 0.1 μm. The fs laser beam was focused inside the optical fiber through a water immersion objective lens (Olympus UMPlanFL 20×) with a numerical aperture of 0.4. The spot size of the focused

beam was approximately 1 μm in air. The velocities of the stages were set at 50 μm/s during fabrication.

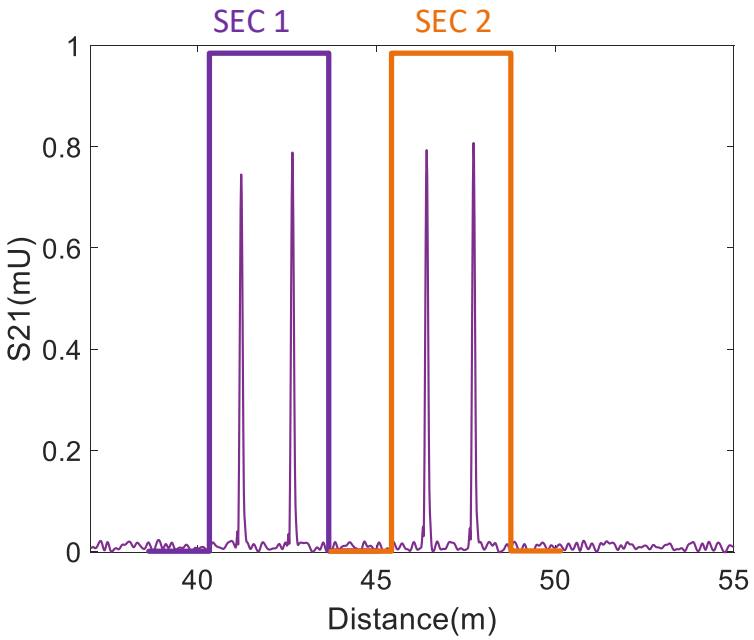

Figure 4.4 Time domain signal of each reflector

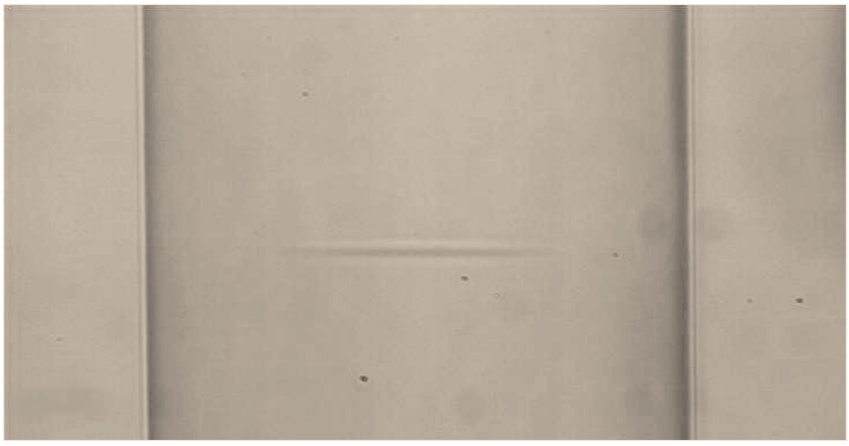

Figure 4.5 Microscope image of the fs laser irradiation region

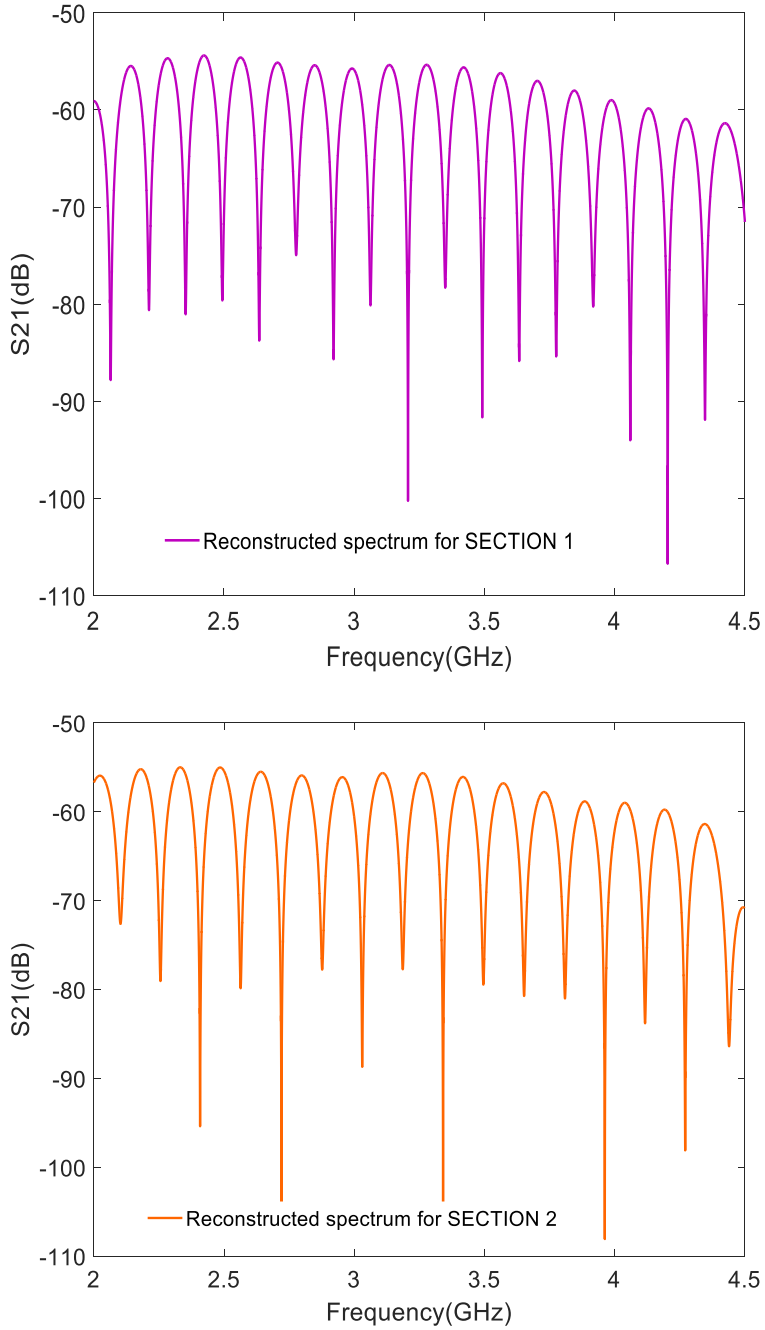

Figure 4.6 Reconstructed frequency domain spectrum of two IFPIs

Figure 4.5 shows the microscope image of a fabricated reflector. The microwave photonics system is connected to the MMF fiber under fabrication to monitor the reflectivity of each

reflector during the fabrication. In our experiment, the reflectivity of the reflector is measured on a scale of 10^{-3}. The entire reflector fabrication procedure can be completed within ten minutes.

The distances between two adjacent reflectors were in the range of 60 to 70 cm. It was not our intent to precisely control the distances since neither equal nor unequal distance will change the demonstration results [90]. However, the distance is limited by the microwave frequency sweeping band. The minimum distance we can separate in the time domain is inversely proportional to the bandwidth. For example, with a 10 GHz microwave band, the minimum distance that can be separated in the time domain is approximately 1 cm. Figure 4.4 shows the time domain signal while Figure 4.6 shows the reconstructed frequency domain signal of two IFPIs. The distance value between two reflectors represents the light travel path difference between two reflectors, which is twice the physical length.

4.3 Microwave Interrogated Polymer Fiber Fabry-Perot Interferometer for Large Strain Sensing

The use of optical fiber sensors for accurate and reliable measurements for monitoring the structural heath of civil engineering and industrial components has been accept for decades [91]. These miniaturized sensing devices have answered the increasing demand for safe and reliable structures since they have the advantages of high sensitivity, fast response time, large dynamic range and flexibility in use, characteristics which make

us cautiously optimistic about their use for measuring distributed physical quantities such as strain or temperature. As a result, different types of optical fiber sensors have been studied for detecting load-bearing structures [92]. For example, the fiber extrinsic Fabry-Perot interferometer (EFPI) sensor was developed based on fiber-optic acoustic emission. By attaching it to the outer surface of a structure, dynamic signals of a strain test were recorded resolving from optical length difference transferred from surface deformation. This concept provided information about the overall length bearing behavior, although it is limited by the integration of the sensor and the structure. Fiber Bragg grating (FBG) sensors are another common optical component for measuring strain distribution, one which is based on wavelength detection sensing [93].

Glass optical fibers are the most commonly used optical fibers in applications because of their high information transmission capacity coupled with their low loss [94]. In comparison, polymer optical fibers (POF) are composed of simpler and less expensive components as well as exhibit greater flexibility and resiliency to bending, shock and vibration, giving them a longer measuring range of strain or temperature along the fiber length. Traditionally, they are composed of PMszMA (acrylic) as the core that facilitates the transmission of light and fluorinated polymers as the cladding material [95], providing them with the added advantage of high corrosion resistance, one of their material properties; however, plastic fibers are much thicker than glass. Optical polymer fiber-optic sensors for monitoring large deformations in geo-structures have been developed using different sensing techniques. Optical time domain reflectometers (OTDRs) were proposed in the initial stage of research on distributed sensing [96][97]. When a short light

pulse launches into a fiber and the Rayleigh scattered light is reflected to a detector, the resulting signal in exponential decay with time can be converted to distance information. In later research, the optical frequency domain interferometry (OFDRs) with millimeter scale spatial resolution was used to measure the amplitude and phase information of interference fringes in a frequency domain [98], resulting in distributed sensing in a short-haul optical fiber link [99].

More recently, optical carrier based microwave interferometry (OCMI) has been reported as achieving fully distributed sensing with a number of unique advantages including high signal quality, relieved requirements for fabrication, low dependence on the types of optical waveguides, insensitivity to variations of polarization and high spatial resolution [84]. This system has been used for strain and temperature distributed sensing though cascaded intrinsic Fabry-Perot interferometers formed by cascaded weak reflectors inside a glass optical fiber.

Here, we report a test of a newly designed POF-based cascaded FPIs distributed strain sensing system using the OCMI technique. FPIs formed by weak reflectors were directly fabricated through blade cutting on the fiber core. When the distance between two adjacent reflectors was larger than the coherence length of the light source, the optical interference components in the received signal became zero, and the microwave terms were processed to form a microwave interferogram, which was further processed to calculate the optical path difference (OPD) between any two cascaded reflectors along the POF. The large local strain as well as the strain distribution along an acryl beam was measured using this system. The results indicate that the POF-OCMI system has the capability of providing

full distributed large strain information. This POF-OCMI configuration looks promising for measuring distributed cracks for the purpose of monitoring structural health.

4.3.1 Principle of Operation

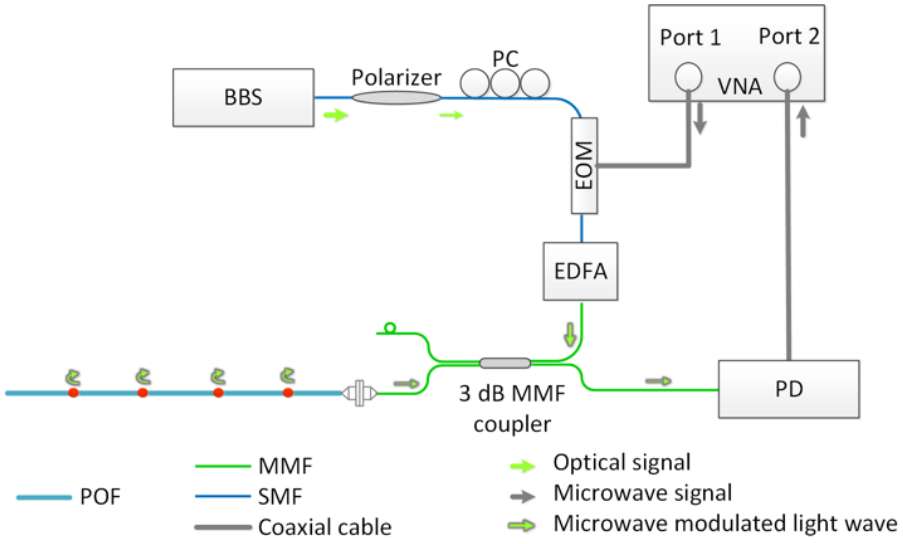

Figure 4.7 Schematic of the POF-OCMI distributed sensing system

Figure 4.7 shows the schematic of the POF-OCMI distributed sensing system. First, the intensity of the light from the broadband source (BBS) is modulated by a microwave signal in an electro-optic modulator (EOM, Pirelli Opto-Electric Components Team, Italy). An in-line fiber polarizer (Thorlabs, US) and a polarization controller (Thorlabs, US) followed by the light source are used to optimize the modulation depth of the EOM. The EOM is driven by Port 1 of a vector network analyzer (VNA Agilent E8364B). The microwave-modulated light, for which the optics is the carrier and the microwave is the

envelope emitted from the EOM, is then coupled into a 3-dB 2X2 multimode fiber coupler. The lead-in and out fiber pigtails of the coupler are made from grade index MMF with an inner/outer diameter of 62.5/125 μm. One lead of the fiber coupler is connected to a piece of POF through the FC/FC adaptor. The end of the other lead is terminated with a knot. Weak reflectors are fabricated on the POF. The reflected light from these reflectors is then detected by a high-speed photo-detector (OE-2 Wavecrest corporation), which converts the optical signal into an electrical signal. The electrical signal is then recorded by Port 2 of the VNA. The VNA is referred to as

voltage ratio measurements where a swept continuous wave (CW) source in microwave band is tracked by a transmission receiver and the results are displayed as scattering parameters ($S_{21}(\Omega)$). $S_{21}(\Omega)$ is actually the transfer function of the system, which carries both the phase and amplitude information. The Fourier transform of the $S_{21}(\Omega)$ provides time-resolved discrete reflections along the optical fiber and is expressed as

$$X(t) = \sum_{i=1}^{N} \left|\Gamma_i\right|^2 A^2 M \left|\sin c\left[(\Omega_{\max} - \Omega_{\min})(t + \tau_i)\right]\right|, \quad (1)$$

where Γ_i is the amplitude reflection coefficient of the *i*-th reflector among the total *N* reflectors, *A* is the amplitude of the modulated optical wave, *M* is the amplitude the modulation, which fell in the range of 0 to 1, $\Omega_{\max}$ and $\Omega_{\min}$ are the maximum and minimum swept angular frequency, τ_i is the propagation delay of the signal corresponding to the *i*-th reflector. The amplitude of the *i*-th pulse is proportional to the reflectivity of the *i*-th reflector, and the time gate function *g*(*t*) can be applied to select any

two adjacent time domain pulses. The time domain signal after applying a gate function is thus given by $X(t)g(t)$. The microwave interferogram can be got by Fourier transforming the gated signal back to the frequency domain, which can be used to find the optical distance between the two gated reflectors. The reconstructed OCMI-FPI interferogram is given by

$$S_{OCMI} = S * G(\Omega)\exp(-i\Omega\tau_0), \tag{2}$$

where $G(\Omega)$ is the inverse Fourier transform of the gate function $g(t)$; τ_0 is the time delay of the gate function. The OPD between the two gated reflectors can be easily found out by reading the free spectral range (FSR) on the reconstructed interferogram,

$$\begin{aligned} OPD &= \left|2(z_i - z_j)n\right|, \\ FSR &= \frac{c}{OPD}, \end{aligned} \tag{3}$$

where z_i and z_j are the physical distances from the laser source to the ith and jth reflectors, c is the speed of the light, and n is the effective refractive index of the optical fiber. For the grade index multimode fiber, the value of n is the average results based on all exited modes. Any perturbation along the fiber changes the mode distribution inside the fiber, but the effective refractive index will not experience any obvious change, especially in the grade index MMF case. On the other hand, a change in the difference in length between two reflectors could appear as an interference fringe shift and could be easily read out from the reconstructed spectrum. In this sensing system, the strain on each section is defined as a ratio of frequency shift and initial frequency,

$$\varepsilon = \frac{\Delta F}{F} = \frac{\Delta L}{L}(1 - P_{eff}) \tag{4}$$

where ΔL is the pull distance, and the P_{eff} is the effective strain-optic coefficient, approximately 0.35 for PMMF material.

4.3.2 Sensor Material and Fabrication

The most significant limitation of POF is its high attenuation, its attenuation loss being greater than that of glass fiber. Attenuation for glass fiber is generally in the range of 0.3 dB/km or less, but for POF it is generally in the range of 50 dB/km to 100 dB/km or more. Consequently, glass fiber can transmit light for tens of kilometers without any difficulties associated with loss, while POF is seldom useful in lengths over 100 m. Graded-index fiber and low-NA POF are two solutions for reducing attenuation problems. GigaPOF fiber is a perfluorinated (PF) grade index multimode polymer optical fiber (GI-POF) with low attenuation at infrared range. Figure 4.8 shows the attenuation behavior of glass- and polymer-based optical fibers, where the attenuation for PF GI-POF at a wavelength of 1550 nm is approximately 40 dB/ km, much smaller than that of the PMMA

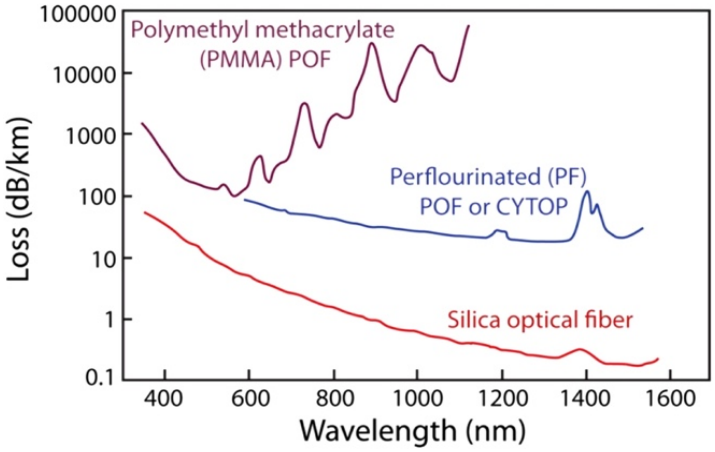

Figure 4.8 Attenuation of graded index POF

POF.

The POF used to fabricate the POF-OCMI sensors, GigaPOF from *Chromis Fiberoptics,* is a PF GI-POF. The core/cladding diameter of a GigaPOF fiber is 62.5/500 ⌈m, and its effective refractive index is 1.33. The core size of 62.5 ⌈m matches the standard input and output port size of optical communication equipment, though the NA mismatching will induce a power loss of approximately 2 dB. The low material dispersion of PF GI-POF enables data transmission rates of up to 10 Gbps km at 1550 nm, meaning that FPI fabricated by GigaPOF can be integrated throughout the infrared microwave photonics system, where the modulation bandwidth can be larger than 10 GHz. Compared with the visible light modulation with a bandwidth limited at 1GHz, the infrared microwave photonics system provides 10 times higher spatial resolution.

The reflectors, basically a series of shallow air gaps on the fiber core, were made by blade cutting. A 120 ⌈m thick blade was clamped by a holder attached to the Z-axis of a three-dimensional stage (Newport). This high precision motion stage had a moving accuracy of 100 nm. The GigaPOF fiber was placed horizontally and mounted without bending by a pair of fiber clamps while the cutting processing was in-situ monitored by a CCD camera. The cutting blade was moved vertically down to the fiber core step-by-step at 2 ⌈m per feeding. Due to the material properties, elastic deformation of the polymer fiber under cutting pressure could affect the air gap formation. Furthermore, the thickness of the blade could cause two-direction horizontal force resulting in ruptures at the bottom of the air gap. When viewed from the side, a specific depth and location for the air gap

could be precisely determined. Seven reflectors were fabricated along one of the PF GI-POF ends, and the distance between two adjacent reflectors was approximately 12.7 cm. These reflectors along with the two ends of the POF formed 6 sections as shown in Figure 4.9(a)

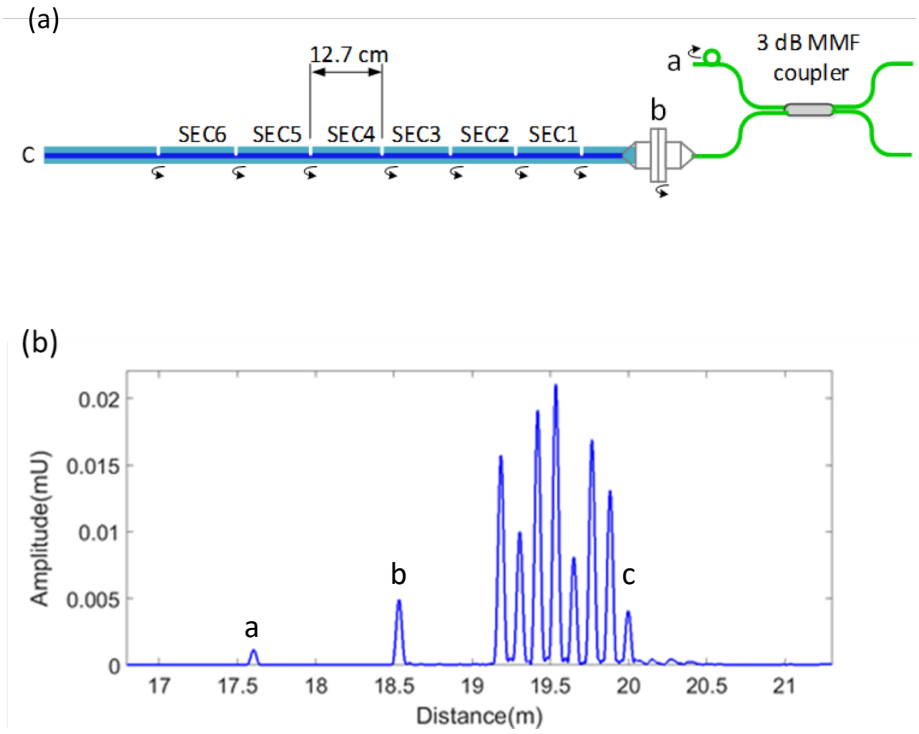

Figure 4.9 (a)Schematic of the cascaded sensors (b) Time domain signal. Pulse 'a' was generated by the terminated end of the other lead of the MMF coupler, pulse 'b' was generated by the FC to FC adaptor, pulse 'c' is generated by the unpolished end of the POF. The pulses between 'b' and 'c' are the reflections from the blade cutting induced shallow air gap in the core of the POF.

One end of the POF was well polished and terminated with a FC connector. The POF was connected with one lead of the multimode grade index optical fiber coupler through an FC to an FC adaptor. The amplitude spectrum of the time domain signal is

shown in Fig. 4.9(b), where pulse “a” was generated by the terminated end of the other lead of the MMF coupler, pulse “b” by the FC to FC adaptor, and pulse “c” the unpolished end of the POF.

4.3.3 Distributed Strain

The 6 sections formed were 6 cascaded FPIs. Sections 1, 2, and 3 were fixed on four high accuracy linear stages. To avoid stretching the blade induced air gaps, we placed the two fixing points inside of the mounted sections, 9.1 cm apart from each other. A piece of rubber and a post were placed on the top of each fixing point to increase friction, and an all purpose glue was applied to the fixing point.

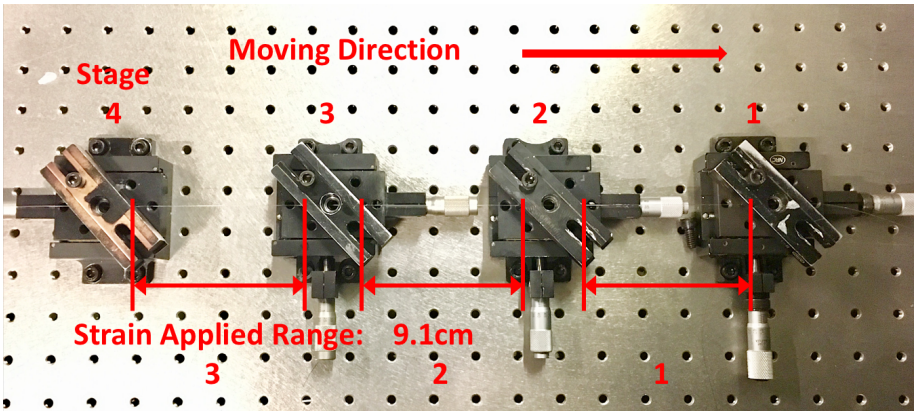

Figure 4.10 Section 1,2,3 were fix on four high accuracy linear stages with strain applied range in 9.1cm.

The VNA was set to 16001 sampling points in the microwave bandwidth from 1GHz to 6 GHz, and the intermediate frequency bandwidth (IFBW) was set as 1 kHz. Axial strains of 5.5 mε per step were applied to the 9.1 cm regime by pulling the POF a distance

of 500 μm per step. Eight pulling steps were made from Stage 1 to Section 1 first. The reconstructed S_{21} amplitude spectra for each section, with the initial frequency ranging from 3.5 GHz to 4.2 GHz, was taken for interrogation. The reconstructed frequency domain spectrum of Section 1 shifted linearly in response to the strain applied, while the reconstructed spectrum of the other sections experienced slight variance. Figure 4.11(a) shows the reconstructed amplitude spectra for Section 1 under different applied strains. The total dip frequency change for the interrogation dip was -106.3 MHz in response to 44.4mε, where the initial dip frequency was 3.89 GHz. Figure 4.11(b) plots the ratio of the dip frequency shift to the initial frequency as a function of the applied axial strain for all sections. The slope of the strain versus the dip frequency shift for Section 1 was -2.349 MHz/ mε, which is close to the calculated value (-2.4877MHz/ mε).

(a)

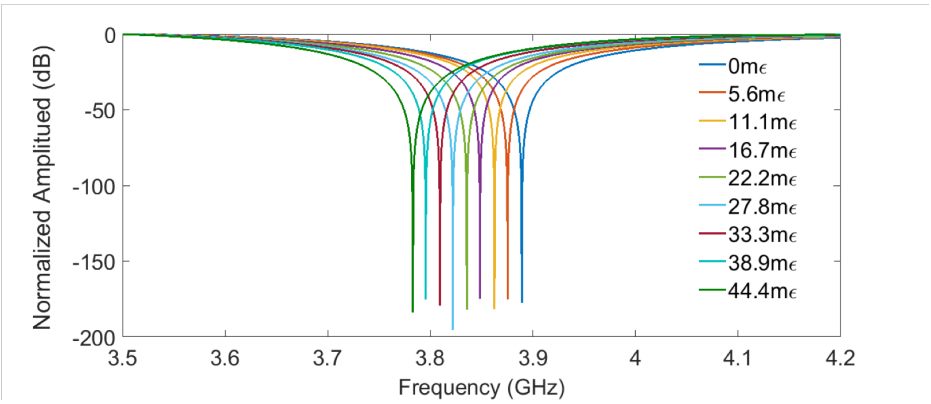

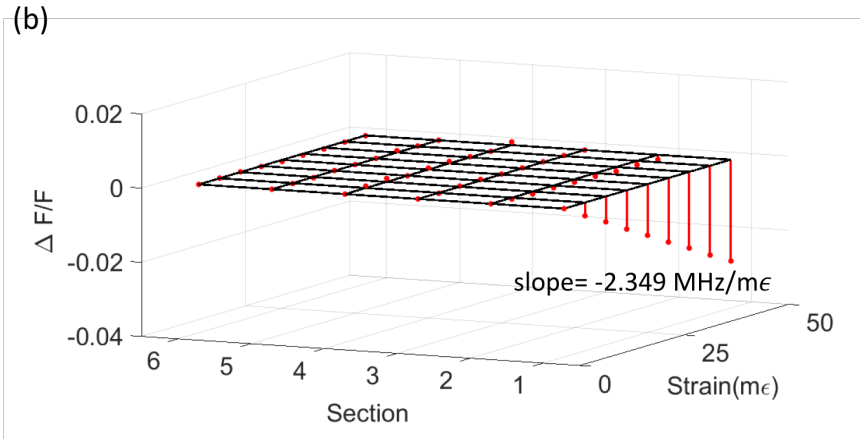

Figure 4.11 Apply the strain (a) reconstructed amplitude spectra for the section 1. (b) Dip frequency shifting as function of strain for all the 6 section

Similarly tests were conducted for Stage 2 and Stage 3 to verify the conditional independent sensing function of the entire IFPI sensor system. Eight steps (5.5 mε per step) were made to the right direction on Stage 2, causing a release on Section 1 and tension on Section 2. The reconstructed spectra of Section 1 shifted back to the original, while the unrecoverable plastic deformation of the polymer fiber may cause a slight change of sensing performance of the initial level. Figure 4.12(a) shows the dip frequency shift for all 6 sections as a function of the released strain on Section 1 and the increasing stain on Section 2. The frequency shift was still linear for this change of strain, and the slope of Section 1 was 2.390 MHz/ mε while that for Section 2 was -2.286 MHz/ mε. The same step of increase or decrease in the spectrum for Section 1 results in the same amount of shifting but in a different direction. The same experiment was conducted on Stage 3 affecting Sections 2 and 3. Figure 4.12(b) shows the dip frequency shift for all 6 sections as well. The slope of Section 2 was 2.643 MHz/ mε and -2.573 MHz/ mε for Section 3. The

experimental results indicated that this POF sensor can withstand strains as large as 44.5 mε .

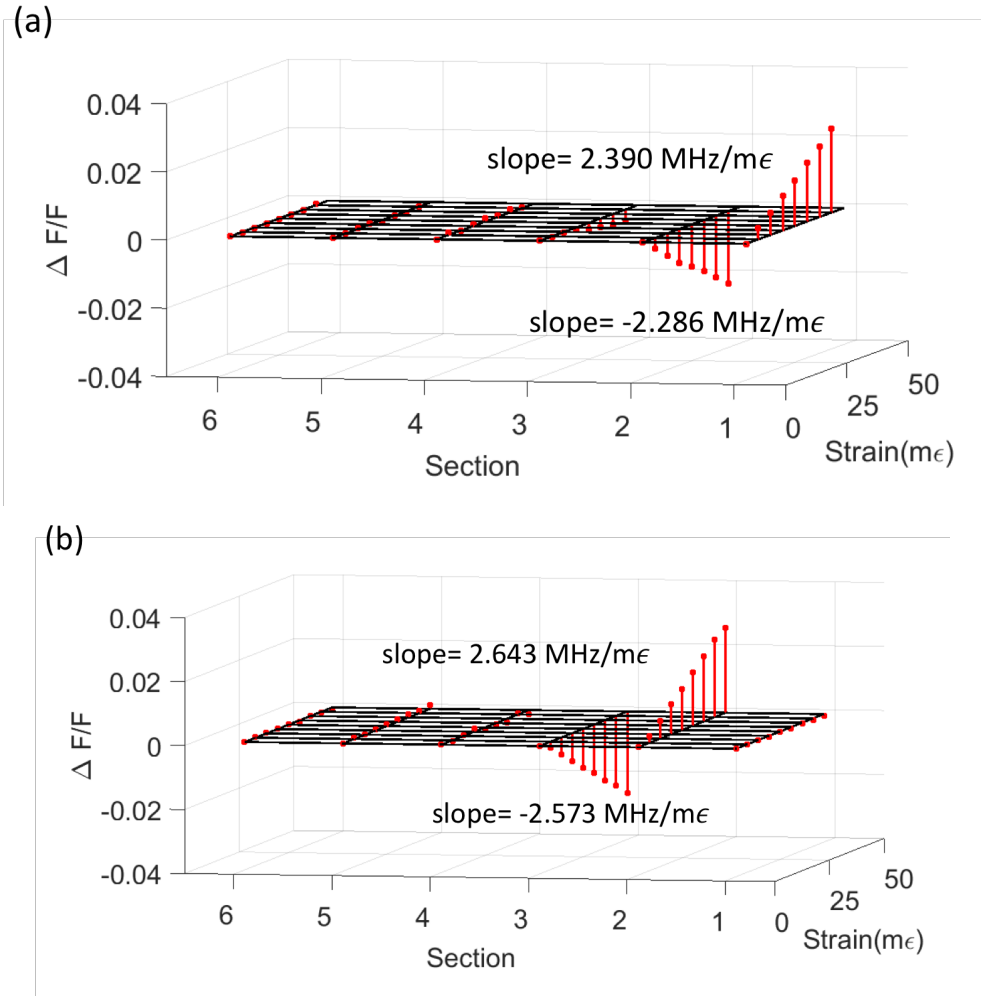

Figure 4.12 Apply the strain (a) Dip frequency shifting as function of strain for all the 6 section when moving stage 2. (b) Dip frequency shifting as function of strain for all the 6 section when moving stage 3

All the reflectors were well protected against the width of the airgap change generated by the reflectivity change, but when strain was applied, the amplitude of the time

domain signal showed a dramatic change as shown in Fig. 4.13 (a). The mode distribution inside the POF changed within the range of the strain applied , and it also changed the sections after that range. The effective refractive index changed slightly for those sections, and the largest changes occurred in the reflectivity of the reflectors after the strain applied range. Figure 4.13(b) shows the amplitude of each time domain pulse as a function of the strain. The dramatic pulse amplitude change started at peak 2 and toward the fiber end. The change was not revertible; the pulse amplitude did not return when the strain was released. The change also did not follow an increase or decrease trend to the applied strain, indicating that the change was not induced by the loss of the fiber. The reflectivity change resulted in a slight shifting of the reconstructed spectrum for the related sections.

(a)

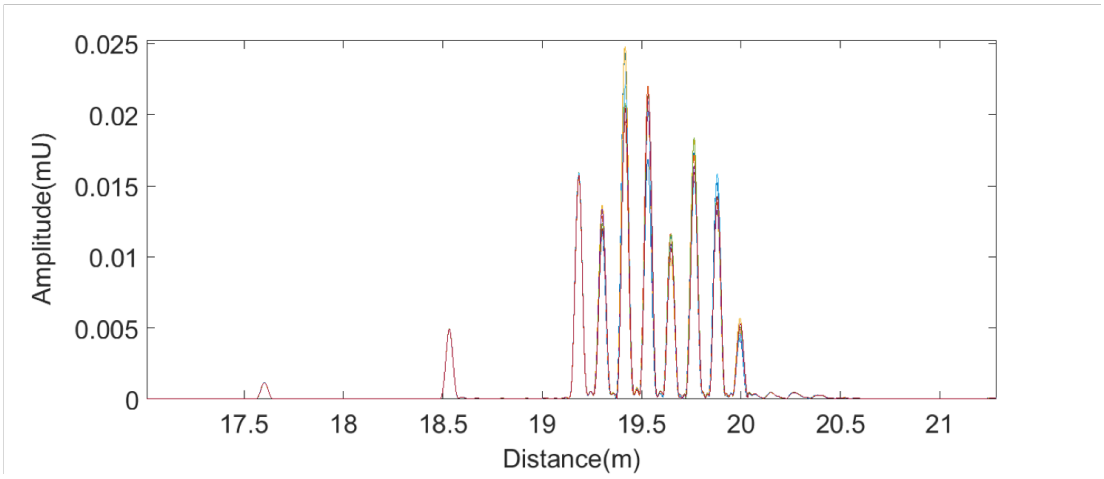

(b)

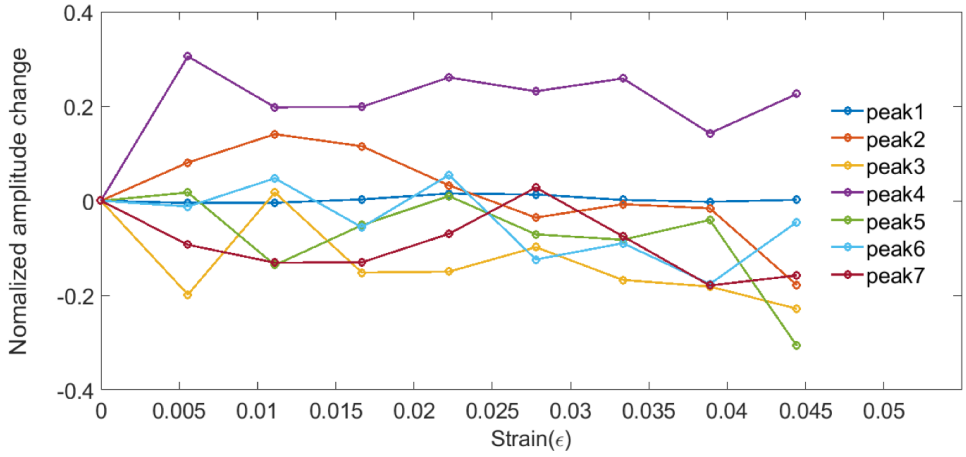

Figure 4.13 (a) Amplitude of the time domain signal under different strain. (b) Normalized amplitude of the time domain pulse as function of strain

4.3.4 Conclusion

A Fabry-Perot type PF GI-POF sensor using the CMI technique was examined in this study. The experimental results show excellent strain sensitivity under both increasing strain and decreasing strain, both of which are in good agreement with the theoretical calculation. The measurement resolution was 30 με at room temperature. This POF sensor can withstand strains as large as 44.4mε without failing, approximately 40% more strain that a typical glass optical fiber can withstand. The strain distribution results indicate that this POF sensor has great potential for sensing spatially continuing large strains, such as distributed crack sensing for the structual health monitoring.

CHAPTER FIVE

PICOSECOND LASER MICROMACHINING

Since the femtosecond laser micromachining of fiber optics sensors, a process developed in our lab, has shown excellent capability in ultrahigh precision fabrication in subsequent experiments, we became increasingly interested in further developing this technique for more practical manufacturing applications. The picosecond laser, which is also a type of ultrafast laser, has higher output power than the femtosecond laser because of its longer pulse duration [49]. Thus, this laser exhibits larger operation capability for machining both transparent materials and non-transparent materials [100]. If integrated into the additive manufacturing process, the picosecond laser has the potential to be a powerful tool for fabricating micro-scale structures on or inside printed objects either by precisely removing the materials or changing the index in the transparent bulk samples [101][102]. This laser is based on cold ablation since its pulse duration of several picoseconds is still shorter than the heat transfer time needed to move electrons to lattices [102].

The dynamic processes of the electrons, ions and melting particles as the picosecond laser pulses removed material were investigated through a series of steps. The emission of electrons and ions from the surface ablated by the picosecond laser pulses were measured using time-of-flight spectroscopy. However, only single-charged ions can be detected if no plasma is generated on the surface [103]. The removal of material was visualized using electron microscopy. The hole opening was observed within 5–30 ns of

drilling, speeding up with increasing laser fluence. At large fluence, the evaporation was collimated in a thin jet perpendicular to the surface, and then, melt expulsion was detected [104].

5.1 Picosecond Laser Micromachining System

Two years ago, our lab began to build an integrated additive manufacturing system implemented with a picosecond laser micromachining tool, with the goal of developing three-dimensional devices with applications in optics, medical science, energy storage, and civil engineering, among others. In addition to the picosecond laser, a material additive tool and a laser heating tool were also integrated into this system. These tools enabled using 3D printing to fabricate specific materials into a designed 3D shape with full automatic control (CAD compatible). In addition, since the system has full laser micromachining capability allowing for the cutting of specific structures, the integration of the additive (3D printing) and subtractive (laser machining) tools into a single system allows us to implant information into the parts as they are being manufactured. Therefore, this new manufacturing system looks promising for the fabrication of smart sensors and components with various functions in a highly integrated procedure. Based on this concept, the following components comprise this system [105].

1. 3D Motion device: a high resolution linear X-Y-Z stage (Newport)
2. Materials additive system: a precise material extruder (eco-PEN 300, Preeflow by ViscoTech, Germany) and its controller (eco-CONTROL EC-200K, Preeflow by ViscoTech, Germany)

3. Laser machining system: a Nd:YAG picosecond laser (APL-4000, Attodyne, Canada) with laser beam delivery optics and a galvo scanner (intelliSCAN 14, SCANLAB, Germany)
4. Laser heating system: a CO_2 laser (Firestar v20, SYNRAD, WA, USA) with a galvo scanner (intelliSCAN 14, SCANLAB, Germany)
5. Active imaging system: a high resolution CCD camera
6. Control center and software: Laser Machining Software (LMS, Direct Manufacturing Control, Lithuania)

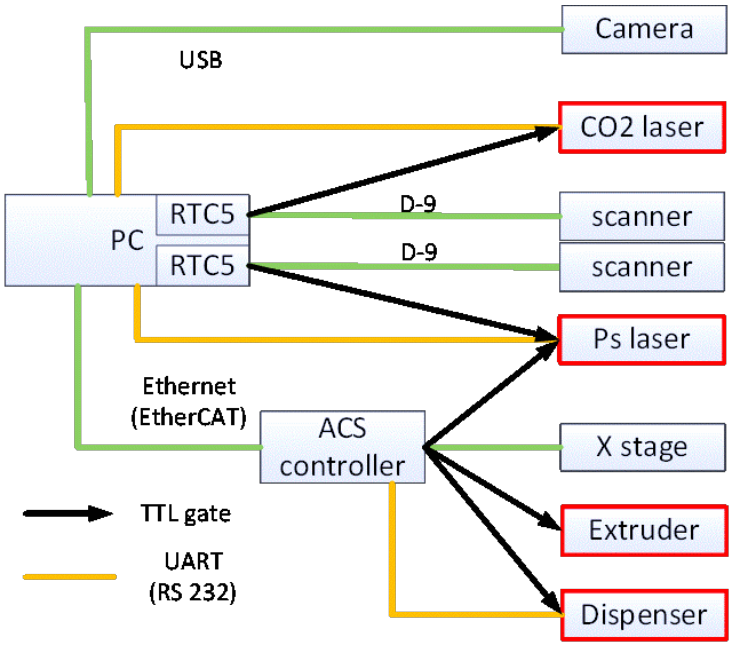

Figure 5.1 Schematic of additive manufacturing system operating flow

Since multiple sub-systems were to operate during the manufacturing process, one of the most challenging tasks was to coordinate the 3D motion device with the different tools through the Laser Machining Software in the desired sequence without any conflict between devices in the programming process loop. Figure 5.1 shows the diagram of the

system's flow of operation. The computer with Laser Machining software on it functioned as the control center. Two main controllers were connected to this control center: One, the ACS controller which was connected through the Ethernet and the second, the RTC5 board which was embedded inside the computer. The ACS controller directly controls the moving of the 3D linear stages and provides several digital output (DOut) ports. When the lasers or extruder connect to the ut ports, the ACS controller gives a TTL gate signal to these devices that triggers their on/off status based on the moving of the stages and the selection of the devices in the laser machining software. Similarly, the RTC5 board, which is used to control the movement of the galvo scanners, also controls the on/off status of the connected laser during scanning. Therefore, all tools can be operated automatically based on the sequence designed in the control center.

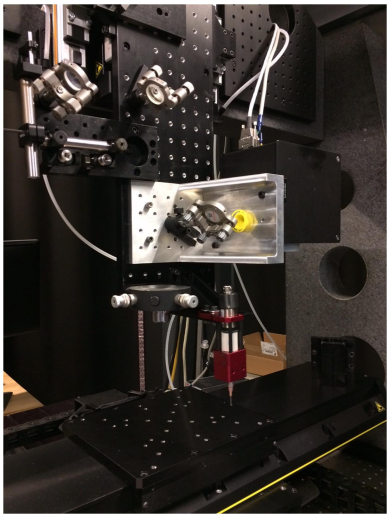

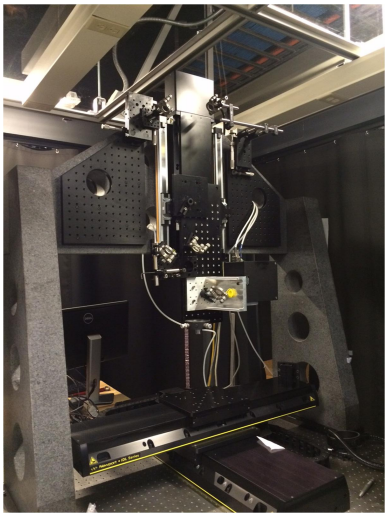

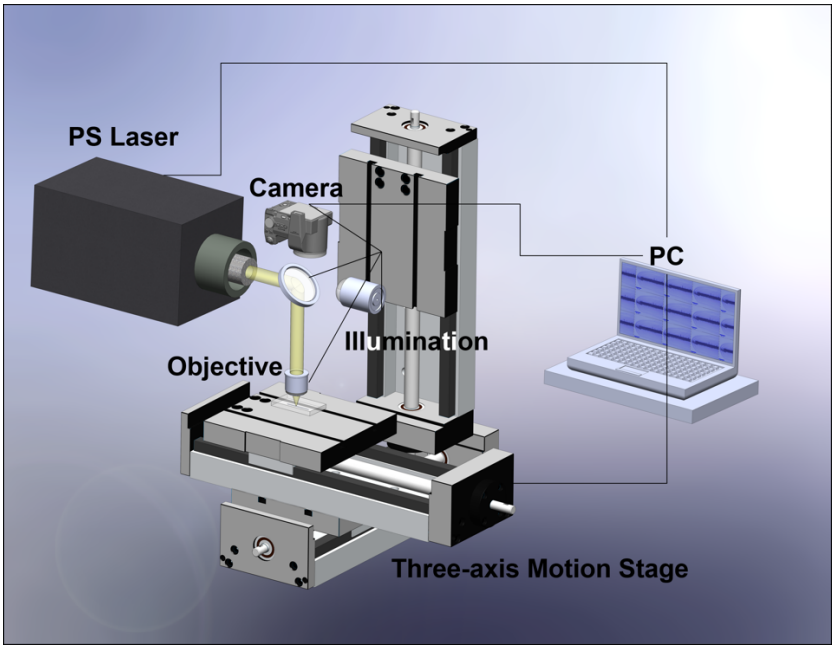

Figure 5.2 Schematic of PS laser system

Figure 5.2 shows the schematic of the picosecond laser machining system (Attodyne, APL-4000) in the integrated additive manufacturing system. This machine is a solid state, diode pumped, amplified laser system with output pulses in the picosecond range and a repetition rate as high as 1 MHz. It consisted of a laser head and a control unit. In addition to the optical components, this laser head also contains a temperature sensor and controller, photodiode sensors, an optical shutter and power laser diodes. The control unit includes a fiber laser oscillator, a diode power supply, an electronics power supply, temperature control for those components including the sensors and the control, and interface circuitry. The central wavelength of the laser spectra is located at 1064 nm with a pulse duration of 6 ± 2 ps. The repetition rate can be set from 0.152 Hz to 1 MHz[106], while the maximum output power is 4 W. The actual power delivered on the

target materials is controlled by adjusting the laser beam optical system. A power meter is used to check the power level at the focal point frequently during fabrication. To achieve hands-free fabrication, remote control is realized through a serial interface with standard RS232 in MATLAB and through laser machining software to automatically set up such laser operating parameters as output power and repetition rate.

To ensure fabrication resolution and good integration with the other devices during manufacturing, all the laser beam delivery optics and the image system were mounted on the z-axis of the long travel industrial linear stage (Newport, IDL Series) of the additive manufacturing system. This z-axis is held by a stable supporting bridge which includes an air flow to ensure a moving accuracy of 100 nm on this highly efficient linear motor-driven stage. It is worth mentioning that its maximum traveling speed can be up to 2 m/s.

5.2 Software Interface of 3D Micromachining

To achieve the challenging goals of three-dimensional manufacturing mentioned above, Laser Machining Software (Newport, LLc) was employed as the control center of the system. It is a complete software package, able to input the original design (the CAD file), design the fabrication sequences, compile the design sequences for every device and operate the entire manufacturing process.

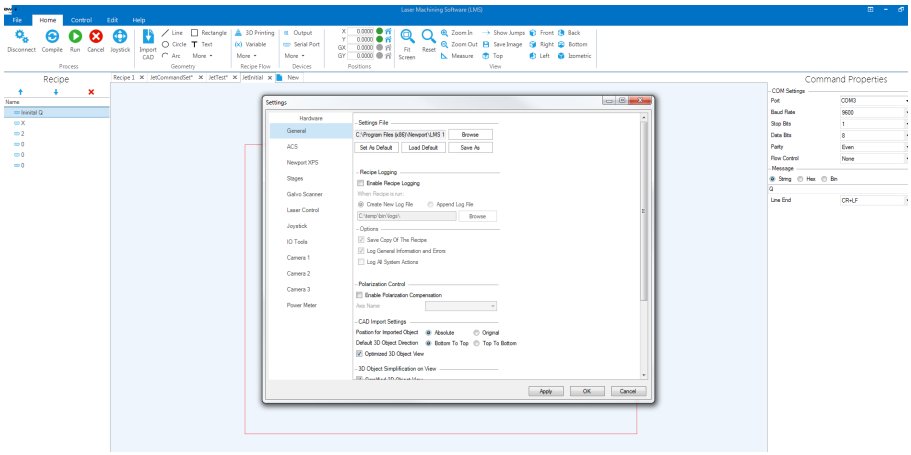
Laser Machining Software (LMS)
File
Home
Control
Edit
Help
Recipe
Command Properties
Settings
Hardware
General
ACS
Newport.XPS
Stages
Galvo Scanner
Laser Control
Joystick
IO Tools
Camera 1
Camera 2
Camera 3
Power Meter
Settings File
Set As Default
Load Default
Save As
Recipe Logging
Enable Recipe Logging
Options
Polarization Control
Enable Polarization Compensation
CAD Import Settings
3D Object Simplification on View
Apply
OK
Cancel

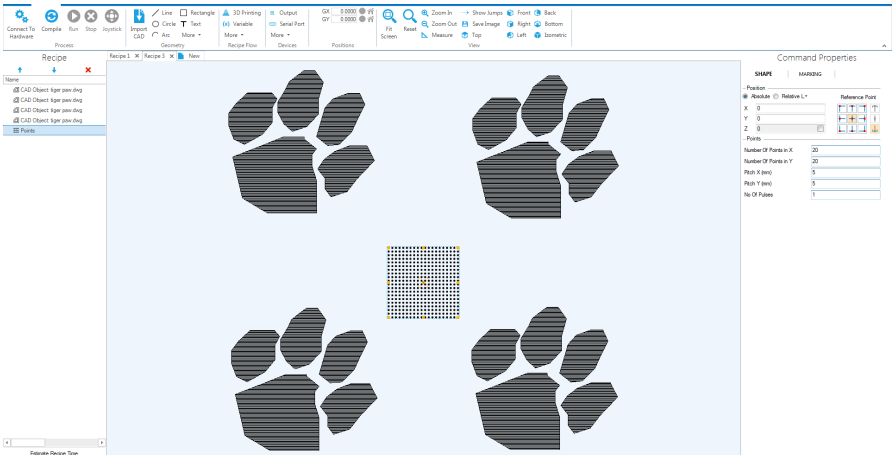
Recipe
Command Properties
SHAPE
MARKING

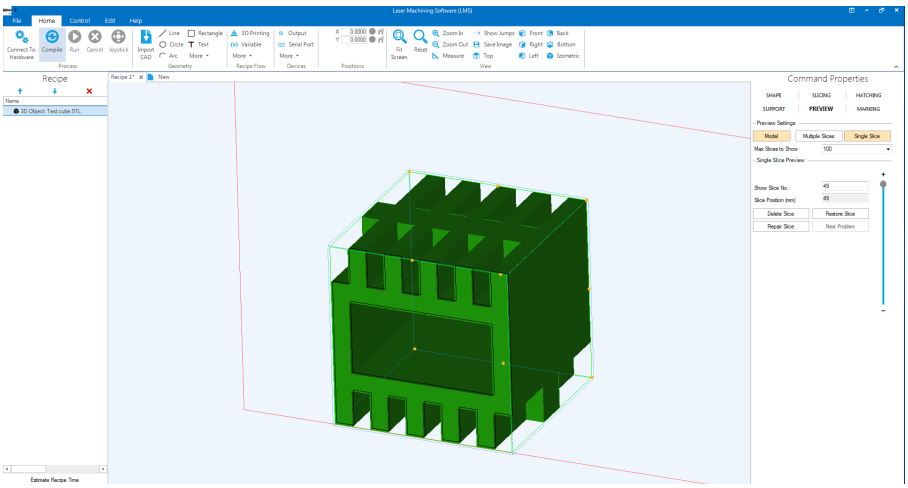

Figure 5.3 DMC user interface for (a) Hardware setting (b) 2D multiple pattern processing (c) 3D STL file import and analysis

For example, when using this software for laser machining, all the devices---the picosecond laser, the galvo scanner and the motion stages—are fully controlled by this software interface, and the laser machining procedure and the laser fabrication toolpath is created by what is referred to as a recipe. There are two ways for generating the toolpath in the software: One is to directly draw various simple 2D features using the built-in drawing tools in the software, while the second is to import the CAD files (DXF, DWG, STL, Gerber, NC Drill, etc.) created from software such as Solidworks and AutoCAD.

One of the special features of this software is that by using the 3D printing function, the input objects can be sliced into layers of the desired thickness and multiple devices can be applied to process every layer. Finally, the 3D object is completed by fabricating layer-by-layer. In addition, this software allows the running of multiple CAD models in one receipt, and different input objects can be processed independently using the same or different devices and parameters.

5.3 PS Laser Test Fabrication on Various Kind of Material

To investigate the material processing capability of the picosecond laser machining system, we have conducted several basic fabrication tests on different types of materials including glass, ceramics and metal, all which represent the most common materials used in both fundamental research and practical applications. The drilling capability, removal quantity, speed and structure accuracy were the most important parameters considered in these tests since they impact the effectiveness of the picosecond laser.

Figure 5.4 shows the SEM images of the glass samples that were ablated by the picosecond laser for 10-time scanning without feeding in depth [107]. The repetition rate was set at 100 kHz with an output power of 3.2 W. The picosecond laser beam was focused on the top surface of the glass substrate through a 10X objective lens (Olympus, 10X) with a numerical aperture of 0.25. The pattern fabricated was designed in the Laser Machining Software. As seen in these SEM images, the width of the ablated grooves is approximately 40 μm with a depth of approximately 20 μm, a result indicating the precision and powerful capability of the picosecond laser's control of the dimensional accuracy and removal quantity. By applying the long travelling distance and the high scanning speed of the motion devices, the processing area of the picosecond laser can be hundreds or even thousands times larger than that of a femtosecond laser system.

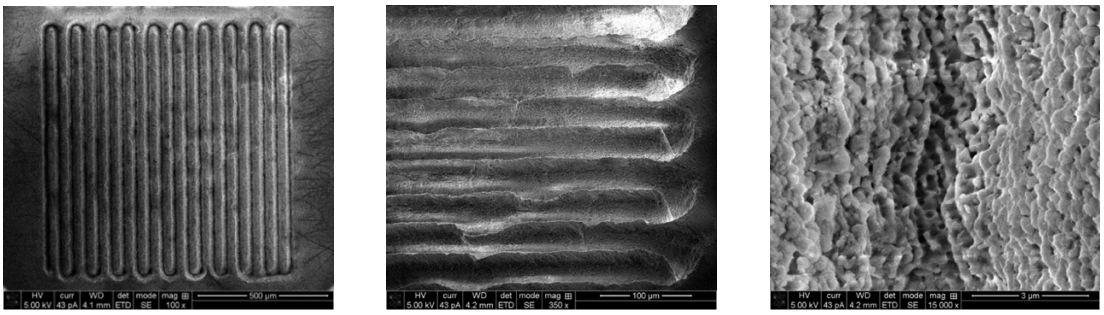

Figure 5.4 SEM photos of single layer ablation pattern by PS laser

For determine the ability of the picosecond laser to machine non-transparent ceramics [37][108], we fabricated the microgroove on the zirconia ferrule seen in Figure 5.5 The microgroove was a through channel to the inner tube of the ferrule. A 3D model of the microgroove was designed using Solidworks and then imported into the LMS software for the model to be sliced into multiple layers. The laser output power, repetition rate and scanning speed were set at 4 W, 100 kHz and 10 mm/s, respectively. Fragments and chips generated during the laser machining were removed by a vacuum tube placed close to the ablated area to ensure their efficient removal. This zirconia ferrule was used to protect the sapphire optical fiber sensors from the high temperature (up to 1600°C) application. One of the challenges was to package the sensors inside the ferrule and seal it firmly. To do so, a high temperature ceramic bond was injected through the microgroove to firmly seal the sensor within the zirconia ferrule with minimum contact area between the ferrule and the sapphire optical fibers.

Figure 5.5 Ceramic cutting test with ps laser micromachining system

In addition, a laser processing test was also conducted to create multi-layer PCB boards coated with 30 μm Cu[109]. The picosecond laser was used to ablate the Cu coating in a design pattern to fabricate the circuit. Figure 5.6 shows the circuit after laser scanning. The white area represents the PCB boards after the removal of the Cu coating. This work demonstrated that the picosecond laser is also capable of processing metal and can be applied in circuit fabrication.

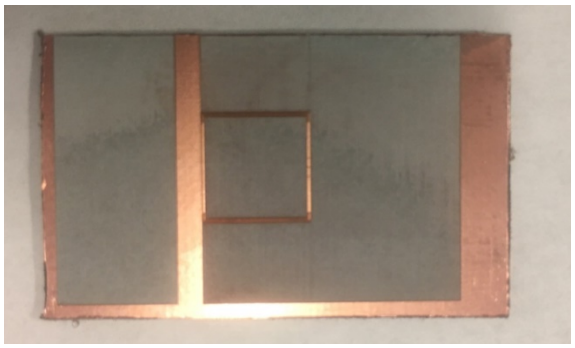

Figure 5.6 Metal cutting test by ps laser micromachining (Power: 4 W, Repetition rate: 100 kHz, Feeding distance in depth: 10 μm Repeating times: 3)

CHAPTER SIX

FABRICATION OF HIGH-ASPECT-RATIO MICRO-GROOVE ON GLASS BY PICOSECOND LASER IRRADIATION

In this study we investigated two laser fabrication methods for generating microgroove structures in a transparent fused silica glass substrate, creating a microfluidics environment with large surface-to-volume ratios for application in microliter-volume reactors. A picosecond laser with a center wavelength of 1064 nm was used to ablate the fused glass substrate, beginning from either the top surface or the rear surface. Based on the dynamic phenomenon of the starting surface, the fabrication quality can be optimized by varying such laser operating parameters as laser fluence, scanning speed and the number of consecutive passes. The dependence of the microgroove shape, surface roughness and aspect ratio on the laser operating parameters were also investigated. Using the optimal parameters, microgrooves up to 210 μm deep and with an aspect-ratio of up to 15:1 were obtained.

6.1 Introduction

Recently, the rapid development of the lab on a chip (LoC) technique has opened up increasingly more possibilities in high tech areas. Among them, bioengineering, especially biosensing [110], has shown the potential available for combining original techniques with LoC. On one hand, it is beneficial for a number of reasons to integrate the microfluidic system with the biosensing design to improve the overall performance of the

biosensor. On the other hand, the growth of fabrication techniques has made significant progress, focusing on the functional diversity of the LoC since high quality and resolution is being achieved more easily. Currently, microfluidic structures in all shapes and sizes can be realized on a variety of materials [111]. For example, fused silica glass is an excellent material for fabricating LofC devices because of its thermal and chemical stability. These characteristics combined with its optical properties explain why it has been widely used for opto-microfluidic devices.

The most common technique for fabricating LoC devises is soft lithography[112], which typically requires photo masks on wafers. The pattern design of this technique is limited to 2D since it involves peeling off layers of the material surface to the depth required by the design. Currently, ultrafast laser direct writing is one of the competing technologies for fabricating three-dimensional microstructures in fused silica glass easily and efficiently [113]. Ultrafast laser most frequently refers to femtosecond and picosecond lasers in the applications mentioned. These lasers use cold ablation due to their ultrashort pulse, which is shorter than the time needed for heat diffusion in the lattices, leading to very accurate fabrication. As a result, laser-induced fabrication has become one of the most reliable techniques for creating 3D microstructures in transparent materials.

When the optical breakdown caused by the nonlinear absorption at the focal region occurs, high aspect-ratio linear structures in fused silica glass like three-dimensional holes can be directly produced in s single step using a femtosecond laser. When further assisted by the breakdown of the water on the rear surface of the glass, the fabrication process can drill holes or channels with higher surface quality [114]. More recently, a rear-surface

ablation enhancement approach has been developed for fabricating high-aspect ratio microchannels in air [115]. The relationship between the laser pulse train and the machining depth indicates that the material removal rate is dependent on the processing rate during rear-surface ablation. Research has demonstrated that a much higher fabrication speed can be achieved using a picosecond rather than a femtosecond laser. Since the output power is increased, the rate of material removal is enhanced, meaning a larger processing area can be realized, while maintaining the dimensional accuracy. A study of the influence of the pulse duration on laser machining showed that the picosecond laser can also be used as a drilling tools for forming micro-channels [116]. However, cracking at the bottom led to multiple ends of a microchannel. To generate high-aspect ratio linear structures, subsequent chemical etching is still necessary after laser machining [35].

This study investigates two methods for fabricating high-aspect ratio microgrooves directly using picosecond laser irradiation in air at a high speed. The laser beam was focused on either the top-surface or the rear-surface at the beginning of ablation. The ablating process was in-situ monitored in order to evaluate the quality of the material removal. The analysis of the laser fluence, fabrication performance and shape of the microgroove resulting from the two methods are also reported here. For the method starting from the rear-surface, a crack-free condition is optimized based on single-point damage at the focal position, which will cause an index change during fabrication.

6.2 Experimental Setup

Figure 2 shows the principle setup for the integrated picosecond laser in-situ fabricating system. A low-power solid state diode pumped Nd:YAG picosecond laser system (Attodyne Inc, APL-4000) was used. Its central wavelength is 1064 nm with a pulse duration of 6 ± 2 ps. The repetition rate can be adjusted to a value between 0.152 Hz and 1 MHz, while the maximum output power is 4 W at 100 kHz. The actual processing power is controlled by adjusting a linear neutral density filter at the beam delivery system. A power meter is used to check the focal point power frequently during fabrication. The laser beam is focused on the surface of the glass substrate through a 5X objective lens (Olympus UMPLanFX) with a focal length of 23.4mm and a numerical aperture (NA) of 0.1, produced a tight beam spot with a diameter of ~19μm. The entire fabrication process was in-situ monitored by a CCD-camera linked to the PC.

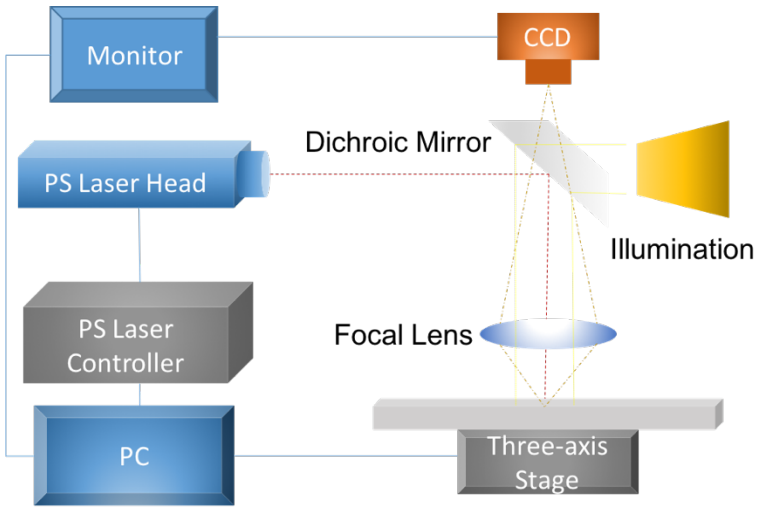

Figure 6.1 The schematic of integrated picosecond laser system

The fused silica glass sample with a thickness of 500μm was mounted on the three-axis motion stage (Newport, IDL280-LM). The entire system was controlled by the Laser Machining Software (LMS), which can interface with a 3D model created in Solidworks. The model for fabrication, which was a 20*300*20000μm cuboid imported into the LMS, formed the fabrication toolpath. As in the traditional 3D printing, this cuboid was sliced into layers of a specified thickness.

6.3 Laser Performance Discussion

Figure 6.2 and Figure 6.3 show the results fabricated using the top-surface method on the fused silica glass. The top-surface can be ablated when the laser pulse energy is higher than 16 μJ at 100 kHz. Since it is a pulsed laser, the single laser track was actually written by a pulse train. In a single track, the percentage of the overlap between two successive pulses is given by

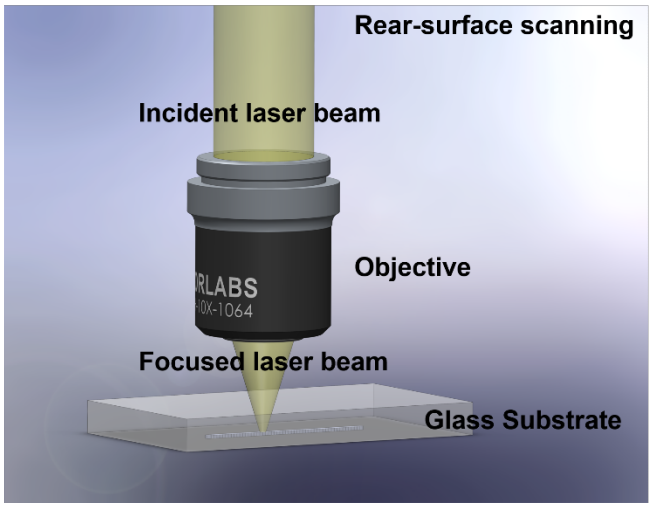

Figure 6.2 Schematic of rear-surface fabrication method

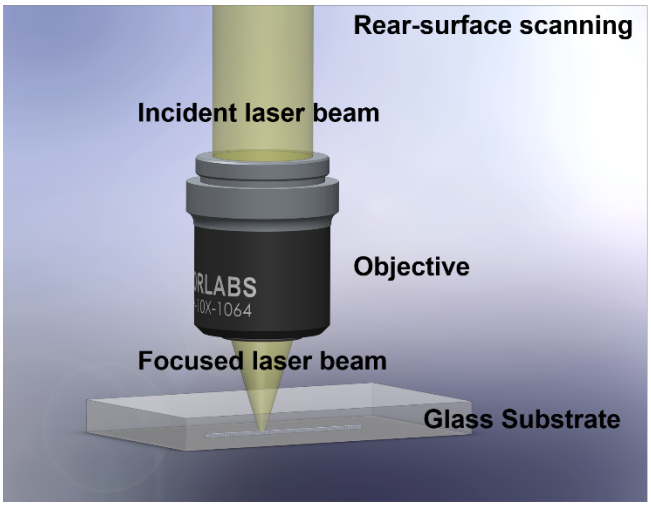

Figure 6.3 Schematic of top-surface fabrication method

$$S_x = 1 - \frac{V}{sfR} \tag{1}$$

where V is the laser scanning speed, f the pulse repetition rate and R the beam radius. The distance b travelled by the beam between two adjacent pulses is given by

$$b = 2R(1 - s_x) \tag{2}$$

As the laser spot moves at a constant velocity V, multiple laser pulses are required to process an area equal to the beam spot diameter (2R), with the number of pulses N required to process this area being given by

$$N = \frac{2R}{b} \tag{3}$$

The corresponding overlap of each pulse over the spot region is given by

$$s_{pulse} = \frac{2R-(n-1)b}{2R} \tag{4}$$

where n is the number of pulses from 1 to N, b is the spot traveling distance and R is the spot radius. The total effective energy falling to every spot size region is given by the product of s_{pulse} and the pulse energy:

$$Q = \sum_1^N \left[\frac{2R-(n-1)b}{2R}\right] \times e \quad (5)$$

Based on the parameters of the objective lens, the R can be calculated as 9.7μm. To ensure the efficiency of the fabrication, the scanning speed was set at approximately 10 mm/s, which resulted in two seconds per scan. Based on calculations, the most efficient value of Q is obtained when the overlapped area between every two pulses is larger than 99%. In the first layer, the depth of the removal quantity was approximately 15 μm. The surface quality was poor after single scanning at this z-axis level, with large chips, sags and crests indicating that the laser processing in the form of a pulse train on an ablated region did not remove the desired amount material. However, the depth of this single scan could be estimated, a value needed for the 3D analysis to slice the model in the z-direction. After multiple tests, we found that at the eighth scanning, the surface roughness was less than 1μm. Therefore, the feeding of the z-axis during cutting was set at 15 μm downward after every eighth scan of one layer.

The use of ablation on the surface of transparent glass cannot be considered for processing bulk material. Beginning from the first scanning, the absorption of radiation at singularities or scattering apparently occurred. The changes in the surface condition and the debris generated during fabrication were concentrated at the ablated area. Thus, the damage threshold for bulk material is much lower than for internal glass modification. As

the focal spot was constantly moving deeper, the primary factor that began to limit the width and depth of the groove was the spatial distribution of the

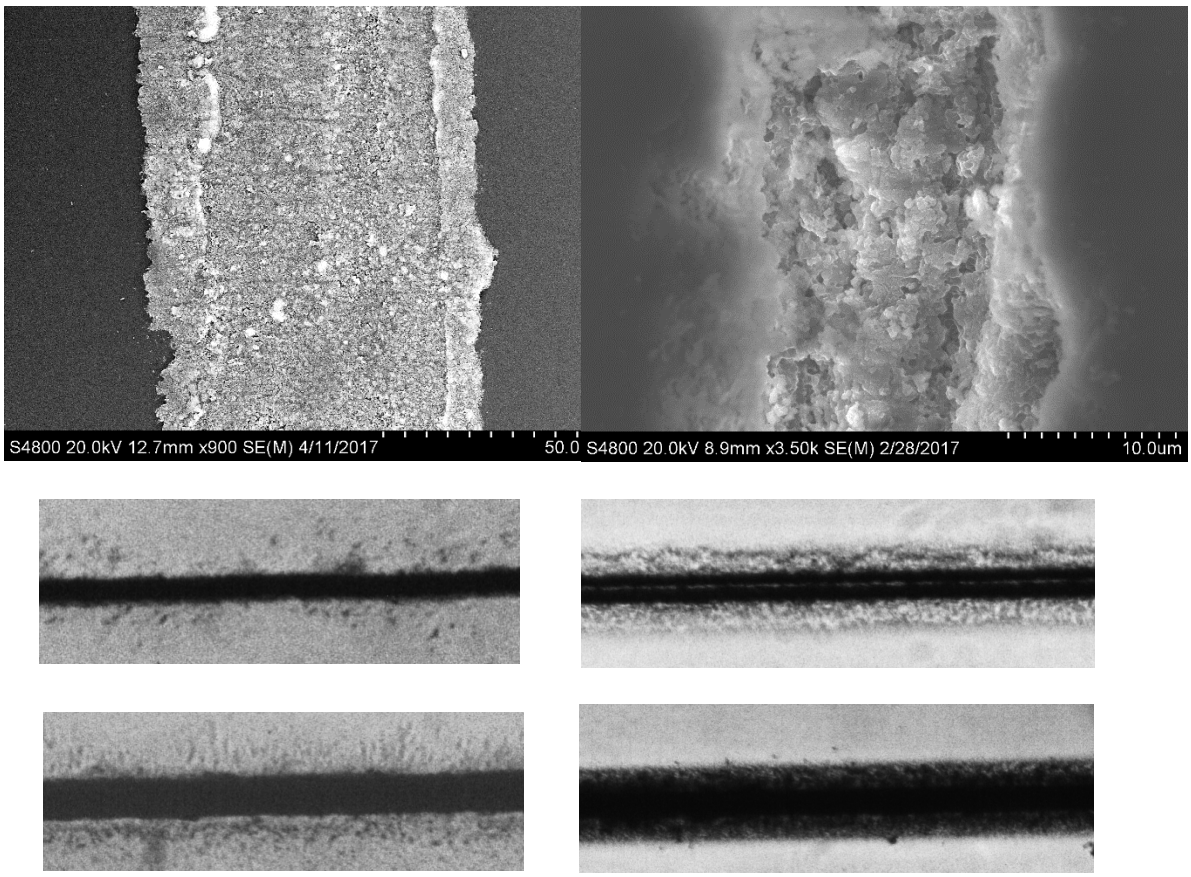

Figure 6.4 Monitoring view of first and final scanning from top-surface ablation method and rear-surface scanning method.

Gaussian beam induced by the focal objective lens which has NA of 0.1. At the top surface, the groove opening was slightly enlarged since the Gaussian beam modification constantly passed through the surface. Then, this opening gradually blocked the cone-shaped beam until the laser fluence at the processed position was not powerful enough to remove the material. As a result, the groove shape could not go beyond a V-shape when using the top-

surface method. Figure 6.5a shows the top views of the first scan and after the final scan respectively. The change in the width was less than 10um. The aspect ratio reached 10:1 cross-section with 245um in depth.

In contrast to the top-surface method, the rear-surface ablation has several similarity in principle. During ablation, considerable energy absorption occurred starting from the top-surface, and the absorbed energy per volume was higher than those for the top-surface method. This phenomenon can be explained by the Fresnel Reflection theory. Furthermore, the reflected wave at the top-surface experienced a 180˚ shift in phase, resulting in destructive interference with the incident wave. However, at the rear-surface, no phase shift of the reflected wave led to a constructive interference. Therefore, the threshold at the rear-surface should be much lower than that at the top-surface.

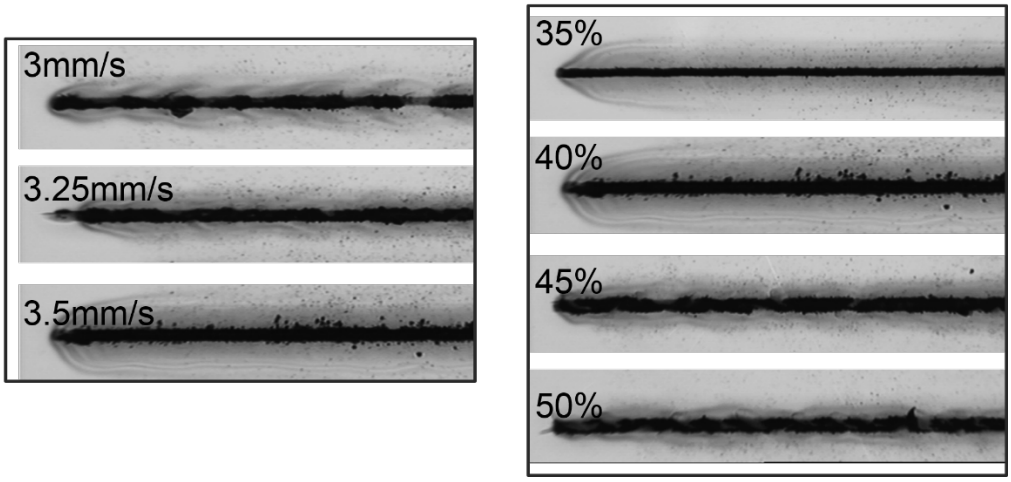

Figure 6.5 (a) The speed test of first scanning in rear-surface ablation method (b) The power level test of first scanning in rear-surface ablation method

For single scanning using the rear-surface method, one issue is finding the appropriate laser focal position on the rear surface; the experimental result showing that this range is quite narrow. Cracks caused by thermal expansion formed easily along the scanning direction. Figure 6.4 shows the SEM images of a single scanning with and without the crack details. For the reason mentioned above, the input laser pulsed energy and the corresponding repetition rate were set at 60μJ/pulse and 200 Hz, as the laser fluence in this area is much lower than on the top surface. Figure 6.5 shows the level test of the single scanning. Two narrow slits on a non-transparent slide were employed in a separate experiment to lift the lens from a position very close to the slit to 6 mm away from the lens. A power meter was placed under the slit, and the power was recorded every 30 μm. At 320μm and 100μm, we saw the highest power density when the lens was 23.637mm higher than the slit. In the crack-free level test, 23.960 ± 10 μm between the lens and the rear surface was the position where debris appeared in place of the crack, meaning the optimum fabrication region is approximately 330 μm higher than the maximum power level in respect to the rear-surface. This may because in this relative position, the high power region has adjusted to the air below rear-surface, thus reducing the high density thermal expansion on the groove while ensuring that enough material is removed.

After determining the focusing level, laser fluence on the rear-surface was investigated as it was for the top-surface. An ablation phenomenon was observed when the power increased to 35% with a laser repetition rate of 200 Hz. At 40% power, debris occurred along the edge of the groove. With an increase in the power level, a crack occurred due to the energy level delivered to the ablated region. These results indicate that

monitoring the first scanning in the ablation processing is critical for judging whether the laser parameter and scanning speed will result in the successful formation of the microgroove. After testing, the z-axis, the moving step was set to 6μm and the second scanning resulted in the 230μm deep microgroove. The shape, however, is better than that from the top-surface as it was a straight cross-section because the beam blocking problem did not exist in the rear-surface ablation method. Based on the Rayleigh criterion, the beam spot size focused on the rear-surface is the spot size divided by the refractive index. According to the energy delivery calculation, only 9.7% of the pulse overlapped resulting in a crack-free condition, which is quite different from the top-surface ablation method. Figure 6.6 shows the microgroove fabricated from the rear-surface and top-surface, which reaches the aspect ratio of 15:1 and 10:1, while the rear-surface opening is more narrow than the top-surface one. Debris generated during fabrication will be vacuumed and will barely stacking on the groove surface.

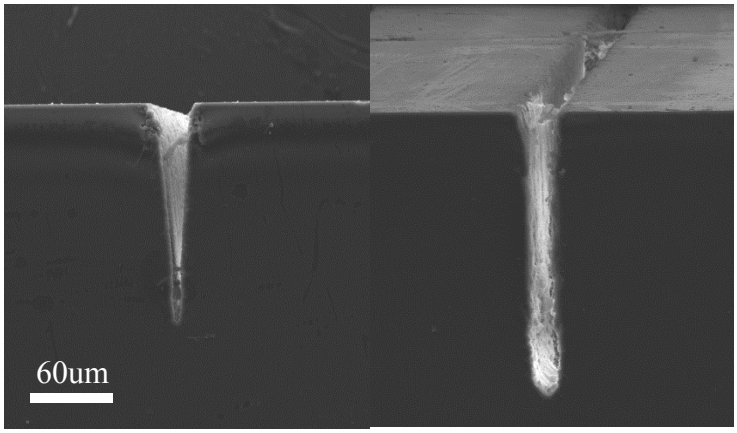

Figure 6.6 SEM of the real-surface and top-surface ps laser fabrication method

6.4 Conclusion

In this work, we assessed the formation of a 2 cm length microgroove through PS laser fabrication on bulk glass using two ablation methods: the top-surface and the rear-surface ablation methods. The aspect-ratio of the rear-surface ablation method reached 15:1 while that of the top-surface ablation method was limited by the NA of the objective lens. But the crack-free condition must be taken into consideration in rear-surface ablation since it is the biggest problem. The surface roughness of top-surface was less than 1μm, while there were chips along the microgroove from rear-surface ablation. The laser parameter based energy delivered for the removal of the material required indicates that the two surfaces have different thresholds. The scanning speed was estimated and the related pulse overlap calculated. In summary, for the application value, if the the depth and shape of microgroove are important characters and the slow fabrication speed resulting in crack-free condition test is acceptable, the rear-surface ablation method is suitable. Similarly, for conditions that rely on formation speed and surface roughness, the top-surface is the better fabrication method in general. Multiple arrangement pattern of microgrooves in parallel shapes can be fabricated in future for various application.

CHAPTER SEVEN

CONCULSION AND FUTURE WORK

7.1 Summery

Ultrafast laser micromachining has been demonstrated here as a powerful tool for material processing, especially transparent material in conjunction with an advanced optical and electrical system setup. Due to their unique characteristics of an ultrashort pulse width and an extremely high peak intensity, fs and ps laser beams can achieve 3D micromachining with large material bandgaps. Compared with the more conventional machining methods, ultrafast lasers offer several advantages, including negligible cracks, minimal heat-affected-zone, low recast, high precision and 3D machining capability.

Optical fiber sensors and novel Lab-on-chip devices are in high demand for various applications such as energy control and monitoring advanced energy systems and chemical/biomedical sensing. To achieve the high performance and robust structure expected today, advanced manufacturing methods are required for the creation of the devices. Motivated by developing fs and ps laser processing methods for the fabrication of novel sensing or monitoring assembly-free sensors and devices, this dissertation primarily focuses on developing advanced ultrafast laser micromachining techniques. This development of novel devices is motivated by the desire to understand the relationship among laser parameters, material properties and 3D optical structures.

Below are the specific achievements addressed in this research:

Chapter 2 introduced the history of laser cutting, explaining the fundamental knowledge behind laser-matter interaction and the basic principles of ultrafast laser micromachining.

Chapter 3 explored the femtosecond laser system setup. The development of the procedure, three-dimensional fabrication and the performance of the entire system was introduced for fs laser assisted sensing applications. Sensors fabricated on a single mode fiber using the Febry-Perot interferometer for strain, temperature and optofuildic sensing were discussed.

Chapter 4 discussed in-situ weak reflector fabrication using an optical carrier based microwave interferometry (OCMI) system for SMF, MMF, cascaded or longer FP cavities. The OCMI provided the capability for monitoring the reflectance of weak reflectors. Multiple in-situ fabrication parameters were discussed.

Chapter 5 introduced the overall planning of the laser assisted additive manufacturing technique, including a picosecond laser micromachining system. Similarly, ps laser micromachining was found to be a unique material processing tools for the next generation manufacturing methods.

Chapter 6 discussed the manufacture of a microgroove and a microchannel in LOC devices of sufficient dimensions and surface smoothness. Two laser fabrication methods for generating microgroove structures in a fused silica glass substrate were compared for application in microliter-volume reactors, which leverage the advantages of large surface area-to-volume ratios.

7.2 Innovations and contributions

The major scientific and technical contributions of this dissertation include the following:

1. A femtosecond laser micromachining system and a picosecond laser assisted additive manufacturing system were developed. Three-dimensional manufacturing methods and laser processing techniques were developed for fabricating integrated optical fiber sensors, lab-on-chip and other specific functional devices.
2. A ferrofluid based optical fiber magnetic field sensor was fabricated using femtosecond (fs) laser ablation. With the help of the fs laser micromaching technique, a built-in micro-reservoir inside a single mode optical fiber was fabricated inside a single mode fiber and capillary tube. The micro-reservoir, which functions as a fiber inline Fabry-Perot (FP) cavity, is filled with ferrofluidic liquid. The refractive index of the ferrofluid varies as the surrounding magnetic field strength changes, a difference that can be optically probed using an FP interferometer.
3. An intrinsic Fabry-Perot interferometry (IFPI) temperature sensor system with self-compensate in strain was fabricated using a Femtosecond (FS) laser. The sensor is composed of two cascaded IFPIs of cavity lengths of 100μm and 500μm based on the wavelength tracking method. When fabricating, the intact puffer coating of the optical fiber was maintained unlike in the traditional approach used to maintain the optical mechanical properties.

4. A polymer optical fiber (POF) based cascaded intrinsic Fabry-Perot interferometer (FPIs) system was developed with the unique ability to measure distributed large strains along a fiber. The optical carrier based microwave interferometry (OCMI) technique was used to in-situ fabricate the sensor structure and interrogate the POF based cascaded FPIs system.
5. Two laser fabrication methods were developed for generating a microgroove structure in a transparent fused silica glass substrate, creating the microfluidic environment for handling of very small fluid volumes, enabling control of microliter-volume reactors while taking advantage of large surface area-to-volume ratios.

7.3 Future work

7.3.1 Femtosecond laser micromachining of optical waveguide

Along with data storage, waveguide fabrication was one of the first potential application demonstrations of the potential of femtosecond laser micromachining for photonic applications. Fs laser-micromachined waveguides can serve as interconnects in a variety of host glasses and have opened up the possibility of three-dimensional layering of waveguides. The pulse energy required for fabricating devices can be as low as a few nanojoules. Over the past decade, the transmission losses, refractive-index contrast and bending radii of femtosecond-laser-micromachined interconnects have been characterized. Transmission losses are of the order of 0.1 dB mm^{-1} for a large variety of materials and processing.

Therefore, how to address the relationship with fs laser parameter and optical waveguide quality is the biggest challenge currently. In order to achieve the low loss, flexible shaping, and various functional waveguides, the laser-induced refractive index change of the material has to be further tested and explored. The refractive-index increase in high-silica glasses has to be large enough for the creation of optical devices and waveguides in bulk glasses.

7.3.2 Picosecond laser micromachining of novel ceramic devices

The design and development of advanced ceramics for high-performance applications ranging from automotive to aerospace, defense, energy, environmental, and biomedical applications is one of the most challenging tasks of modern engineering. The need for advanced ceramic devices depends on the growth of end-use markets, while one of the novel applications is creative fuel cell reactors built using photonic ceramics. These energy devices include protonic ceramic fuel cells (PCFCs) 3-7 , protonic ceramic electrolysis cells (PCECs), solid state ammonia synthesis cells, hydrogen or water sensors, steam permeable membrane reactors, and hydrogen permeable membrane reactors.

For example, Palladium membranes are utilized for gas separation where the pure hydrogen gas can be separated from gas mixture. By increasing the surface area, more gas molecules can come in contact with the membranes, therefore increasing the efficiency of the production rate of the hydrogen. So, an advanced fabrication technique to enhance the performance of certain ceramic devices is the major objective of ultrafast lasers, especially for the picosecond laser.

BIBLIGRAPHY

[1] T. H. Maiman, “Stimulated optical radiation in Ruby,” *Nature*, vol. 187, no. 4736, pp. 493–494, 1960.

[2] P. T. Houldcroft and A. B. J. Sullivan, “Gas-jet laser cutting,” *Br. Weld. J.*, p. 443, 1967.

[3] A. K. Dubey and V. Yadava, “Laser beam machining-A review,” *International Journal of Machine Tools and Manufacture*, vol. 48, no. 6. pp. 609–628, 2008.

[4] J. Uh, J. S. Lee, Y. H. Kim, J. T. Choi, M. G. Joo, and C. Lim, “Laser engraving of micro-patterns on roll surfaces,” *ISIJ Int.*, vol. 42, no. 11, pp. 1266–1272, 2002.

[5] W. M. Steen and J. Mazumder, *Laser Material Processing*. 2010.

[6] W. M. Steen, “Laser material processing - An overview,” in *Journal of Optics A: Pure and Applied Optics*, 2003, vol. 5, no. 4.

[7] I. Pigulevski, “Laser Propulsion Market-Creating Innovation,” *New Sp.*, vol. 4, no. 2, pp. 123–128, 2016.

[8] S. Mueller, B. Kruck, and P. Baudisch, “LaserOrigami: Laser-Cutting 3D Objects,” *Proc. SIGCHI Conf. Hum. Factors Comput. Syst. - CHI ’13*, p. 2585, 2013.

[9] W. Konrad, D. Claus, H. Marcel, and W. Christian, “Laser Prepared Cutting Tools,” in *Physics Procedia*, 2012, vol. 39, pp. 240–248.

[10] C. Klahn, F. Bechmann, S. Hofmann, M. Dinkel, and C. Emmelmann, “Laser additive manufacturing of gas permeable structures,” in *Physics Procedia*, 2013, vol. 41, pp. 873–880.

[11] C. G. K. Malek, "Laser processing for bio-microfluidics applications (part II)," *Analytical and Bioanalytical Chemistry*, vol. 385, no. 8. pp. 1362–1369, 2006.

[12] L. Hao and J. Lawrence, *Laser Surface Treatment of Bio-Implant Materials*. 2006.

[13] J. Ihlemann, B. Wolff, and P. Simon, "Nanosecond and femtosecond excimer laser ablation of fused silica," *Appl. Phys. A Solids Surfaces*, vol. 54, no. 4, pp. 363–368, 1992.

[14] W. Sibbett, A. A. Lagatsky, and C. T. A. Brown, "The development and application of femtosecond laser systems," *Opt. Express*, vol. 20, no. 7, p. 6989, 2012.

[15] N. H. Rizvi, "Femtosecond laser micromachining : Current status and applications," *Glass*, vol. 50, no. 50, pp. 107–112, 2003.

[16] Y. Wang, "Review of long period fiber gratings written by CO2 laser," *Journal of Applied Physics*, vol. 108, no. 8. p. 81101, 2010.

[17] J. Cheng *et al.*, "A review of ultrafast laser materials micromachining," *Optics and Laser Technology*, vol. 46, no. 1. pp. 88–102, 2013.

[18] J. H. Cole, R. L. Johnson, and P. G. Bhuta, "Fiber-optic detection of sound," *J. Acoust. Soc. Am.*, vol. 62, no. 5, pp. 1136–1138, 1977.

[19] M. Ramakrishnan, G. Rajan, Y. Semenova, and G. Farrell, "Overview of Fiber Optic Sensor Technologies for Strain/Temperature Sensing Applications in Composite Materials.," *Sensors (Basel).*, vol. 16, no. 1, p. 99, 2015.

[20] T. Wei, Y. Han, Y. Li, H.-L. Tsai, and H. Xiao, "Temperature-insensitive miniaturized fiber inline Fabry-Perot interferometer for highly sensitive refractive index measurement.," *Opt. Express*, vol. 16, no. 8, pp. 5764–5769, 2008.

[21] B. Lee, S. Roh, and J. Park, "Current status of micro- and nano-structured optical fiber sensors," *Opt. Fiber Technol.*, vol. 15, no. 3, pp. 209–221, 2009.

[22] A. D. Kersey *et al.*, "Fiber grating sensors," *J. Light. Technol.*, vol. 15, no. 8, pp. 1442–1463, 1997.

[23] K. O. Hill and G. Meltz, "Fiber Bragg Grating Technology Fundementals and Overview," *IEEE J. Light. Technol.*, vol. 15, no. 8, pp. 1263–1276, 1997.

[24] T. Yoshino, T. Ose, K. Kurosawa, and K. Itoh, "Fiber-Optic Fabry–Perot Interferometer and Its Sensor Applications," *IEEE Trans. Microw. Theory Tech.*, vol. 30, no. 10, pp. 1612–1621, 1982.

[25] B. Cheng, L. Yuan, W. Zhu, Y. Song, and H. Xiao, "A coaxial cable magnetic field sensor based on ferrofluid filled Fabry-Perot interferometer structure," *Sensors Actuators, A Phys.*, vol. 257, 2017.

[26] R.-Q. Lv, Y. Zhao, D. Wang, and Q. Wang, "Magnetic fluid-filled optical fiber Fabry-Perot sensor for magnetic field measurement," vol. 26, no. 3, pp. 2013–2015, 2014.

[27] K. K. Chin *et al.*, "Fabry-Perot diaphragm fiber-optic sensor," *Appl. Opt.*, vol. 46, no. 31, p. 7614, 2007.

[28] A. Kaur and H. Xiao, "Microcavity strain sensor for high temperature applications," 2016.

[29] Y. Song *et al.*, "An IFPI Temperature Sensor Fabricated in an Unstriped Optical Fiber with Self-Strain-Compensation Function," *J. Sensors*, vol. 2016, 2016.

[30] R. Daw and J. Finkelstein, "Lab on a chip," *Nature*, vol. 442, no. 7101, p. 367, 2006.

[31] B. H. Weigl, R. L. Bardell, and C. R. Cabrera, "Lab-on-a-chip for drug development," *Advanced Drug Delivery Reviews*, vol. 55, no. 3. pp. 349–377, 2003.

[32] H. Craighead, "Future lab-on-a-chip technologies for interrogating individual molecules," *Nature*, vol. 442, no. 7101. pp. 387–393, 2006.

[33] S. Haeberle, D. Mark, F. Von Stetten, and R. Zengerle, "Microfluidic platforms for lab-on-a-chip applications," in *Microsystems and Nanotechnology*, vol. 9783642182938, 2012, pp. 853–895.

[34] M. Hejazian, W. Li, and N.-T. Nguyen, "Lab on a chip for continuous-flow magnetic cell separation," *Lab Chip*, vol. 15, no. 4, pp. 959–970, 2015.

[35] Y. Cheng and Ya, "Internal Laser Writing of High-Aspect-Ratio Microfluidic Structures in Silicate Glasses for Lab-on-a-Chip Applications," *Micromachines*, vol. 8, no. 2, p. 59, 2017.

[36] C. Teng *et al.*, "A review of defect modeling in laser material processing," *Additive Manufacturing*, vol. 14. pp. 137–147, 2017.

[37] L. Rihakova and H. Chmelickova, "Laser micromachining of glass, silicon, and ceramics," *Advances in Materials Science and Engineering*, vol. 2015. 2015.

[38] G. Byrne, D. Dornfeld, and B. Denkena, "Advancing cutting technology," *CIRP Ann. - Manuf. Technol.*, vol. 52, no. 2, pp. 483–507, 2003.

[39] J. Powell and A. Kaplan, "Laser cutting: From first principles to the state of the art," *1st Pacific Int. Conf. Appl. Lasers Opt.*, p. 6, 2004.

[40] J. C. Ion, "Laser Processing of Engineering Materials: Principles, Procedure and Industrial Application," in *Laser Processing of Engineering Materials*, 2005, p. 576.

[41] J. Collins and P. Gremaud, “A simple model for laser drilling,” *Math. Comput. Simul.*, vol. 81, no. 8, pp. 1541–1552, 2011.

[42] T. Q. Qiu and C. L. Tien, “Short-pulse laser heating on metals,” *Int. J. Heat Mass Transf.*, vol. 35, no. 3, pp. 719–726, 1992.

[43] T. Kurita, K. Komatsuzaki, and M. Hattori, “Advanced material processing with nano- and femto-second pulsed laser,” *Int. J. Mach. Tools Manuf.*, vol. 48, no. 2, pp. 220–227, 2008.

[44] E. Carpene, D. Hoche, and P. Schaaf, “Fundamentals of Laser-Material Interactions,” *Laser Process. Mater. Fundam. Appl. Dev.*, vol. 139, pp. 21–47, 2010.

[45] M. E. Fermann and I. Hartl, “Ultrafast Fiber Laser Technology,” *IEEE J. Sel. Top. Quantum Electron.*, vol. 15, no. 1, pp. 191–206, 2009.

[46] E. Assuncao and S. Williams, “Comparison of continuous wave and pulsed wave laser welding effects,” *Opt. Lasers Eng.*, vol. 51, no. 6, pp. 674–680, 2013.

[47] S. H. Ko, Y. Choi, D. J. Hwang, C. P. Grigoropoulos, J. Chung, and D. Poulikakos, “Nanosecond laser ablation of gold nanoparticle films,” *Appl. Phys. Lett.*, vol. 89, no. 14, 2006.

[48] R. R. Gattass and E. Mazur, “Femtosecond laser micromachining in transparent materials,” *Nat. Photonics*, vol. 2, no. 4, pp. 219–225, 2008.

[49] C. B. Schaffer, A. Brodeur, and E. Mazur, “Laser-induced breakdown and damage in bulk transparent materials induced by tightly focused femtosecond laser pulses,” *Meas. Sci. Technol.*, vol. 12, no. 11, pp. 1784–1794, 2001.

[50] and P. G. K. Martynas Beresna,* Mindaugas Gecevi˘cius, “Ultrafast laser direct

writing and nanostructuring in transparent materials," *Adv. Opt. Photonics*, vol. 6, pp. 293–339, 2014.

[51] X. Liu, D. Du, and G. Mourou, "Laser ablation and micromachining with ultrashort laser pulses," *IEEE J. Quantum Electron.*, vol. 33, no. 10, pp. 1706–1716, 1997.

[52] D. Hunger, T. Steinmetz, Y. Colombe, C. Deutsch, T. W. Hänsch, and J. Reichel, "A fiber Fabry-Perot cavity with high finesse," *New J. Phys.*, vol. 12, 2010.

[53] L. Yuan *et al.*, "Femtosecond laser processing of transparent materials for assembly-free fabrication of photonic microsensors," in *Proceedings of SPIE - The International Society for Optical Engineering*, 2016, vol. 9735.

[54] Y. Song *et al.*, "An IFPI Temperature Sensor Fabricated in an Unstriped Optical Fiber with Self-Strain-Compensation Function," *J. Sensors*, vol. 2016, p. 6419623, 2016.

[55] J. Ma, J. S. Wang, C. Denker, and H. M. Wang, "Optical design of multilayer achromatic waveplate by simulated annealing algorithm," *Chinese J. Astron. Astrophys.*, vol. 8, no. 3, pp. 349–361, 2008.

[56] A. M. Memon and M. Guizani, "Design and Implementation Tools for Optical Architectures," in *Proceedings of the Fourth Saudi Engineering Conference*, 1995, pp. 437–442.

[57] A. J. Poustie, N. Finlayson, and P. Harper, "Multiwavelength fiber laser using a spatial mode beating filter.," *Opt. Lett.*, vol. 19, no. 10, pp. 716–718, 1994.

[58] S. Stepanov and S. Ruschin, "Modulation of light by light in silicon-on-insulator waveguides," *Appl. Phys. Lett.*, vol. 83, no. 25, pp. 5151–5153, 2003.

[59] Nikon, “Immersion microscope objective lens,” 2005.

[60] Y. Sorel and J. F. Kerdiles, “Simple measurement of fiber dispersion and of chirp parameter of intensity modulated light emitter,” *J. Light. Technol.*, vol. 11, no. 12, pp. 1937–1940, 1993.

[61] N. B. Dahotre and S. P. Harimkar, *Laser fabrication and machining of materials*. 2008.

[62] S. Matsuo, S. Juodkazis, and H. Misawa, “Femtosecond laser microfabrication of periodic structures using a microlens array,” *Appl. Phys. A*, vol. 80, no. 4, pp. 683–685, 2005.

[63] W. L. Chan, H. T. Chen, A. J. Taylor, I. Brener, M. J. Cich, and D. M. Mittleman, “A spatial light modulator for terahertz beams,” *Appl. Phys. Lett.*, vol. 94, no. 21, 2009.

[64] T. Wei, Y. Han, H.-L. Tsai, and H. Xiao, “Miniaturized fiber inline Fabry-Perot interferometer fabricated with a femtosecond laser.,” *Opt. Lett.*, vol. 33, no. 6, pp. 536–538, 2008.

[65] H. U. Guo-yong, C. Chang-ying, and C. Zhen-qiang, “Free-Space Optical communication using visible light,” *J. Zhejiang Univ. Sci. A*, vol. 8, no. 2, pp. 186–191, 2007.

[66] O. Frazão *et al.*, “Fabry-Perot refractometer based on an end-of-fiber polymer tip,” *Opt. Lett.*, vol. 34, no. 16, p. 2474, 2009.

[67] Yang Song, L. Yuan, L. Hua, and H. Xiao, “Ferrofluid-based optical fiber magnetic field sensor fabricated by femtosecond laser irradiation,” *SPIE OPTO*, vol. 9750, p.

97501U–97501U–6, 2016.

[68] L. Yuan, J. Huang, X. W. Lan, H. Z. Wang, L. Jiang, and H. Xiao, "All-in-fiber optofluidic sensor fabricated by femtosecond laser assisted chemical etching," *Opt. Lett.*, vol. 39, no. 8, pp. 2358–2361, 2014.

[69] N. T. Nguyen, "Micro-magnetofluidics: Interactions between magnetism and fluid flow on the microscale," *Microfluidics and Nanofluidics*, vol. 12, no. 1–4. pp. 1–16, 2012.

[70] K. Raj, B. Moskowitz, and R. Casciari, "Advances in ferrofluid technology," *J. Magn. Magn. Mater.*, vol. 149, no. 1–2, pp. 174–180, 1995.

[71] R. Gao and Y. Jiang, "Magnetic fluid-filled microhole in the collapsed region of a photonic crystal fiber for the measurement of a magnetic field.," *Opt. Lett.*, vol. 38, no. 16, pp. 3181–4, 2013.

[72] X. Li, Y. Shao, Y. Yu, Y. Zhang, and S. Wei, "A Highly Sensitive Fiber-Optic Fabry–Perot Interferometer Based on Internal Reflection Mirrors for Refractive Index Measurement," *Sensors*, vol. 16, no. 6, p. 794, 2016.

[73] S. Schlautmann, G. A. J. Besselink, R. Prabhu G, and R. B. M. Schasfoort, "Fabrication of a microfluidic chip by UV bonding at room temperature for integration of temperature-sensitive layers," in *Journal of Micromechanics and Microengineering*, 2003, vol. 13, no. 4.

[74] Y. Zhang and H. Xiao, "Simultaneous measurement of temperature and pressure with cascaded extrinsic Fabry – Perot interferometer and intrinsic Fabry – Perot interferometer sensors," 2016.

[75] W. Wang, D. Ding, N. Chen, F. Pang, and T. Wang, "Quasi-Distributed IFPI Sensing System Demultiplexed With FFT-Based Wavelength Tracking Method," vol. 12, no. 9, pp. 2875–2880, 2012.

[76] M. Wuilpart and M. Patrice, "Analysis and suppression of nonlinear frequency modulation in an optical frequency-domain reflectometer," vol. 17, no. 7, pp. 5845–5851, 2009.

[77] W. Eickhoff and R. Ulrich, "Optical frequency domain reflectometry in single-mode fiber," *Appl. Phys. Lett.*, vol. 39, no. 9, pp. 693–695, 1981.

[78] Z. Chen, G. Hefferman, L. Yuan, Y. Song, and T. Wei, "Ultraweak Waveguide Modification With Intact Buffer Coating Using Femtosecond Laser Pulses," vol. 27, no. 16, pp. 1705–1708, 2015.

[79] L. Hua, Y. Song, J. Huang, B. Cheng, W. Zhu, and H. Xiao, "Femtosecond laser fabricated multimode fiber sensors interrogated by optical-carrier-based microwave interferometry technique for distributed strain sensing," vol. 9754, p. 97540V, 2016.

[80] S. Takahashi, S. Shibata, I. Electrical, N. Telegraph, and T. Public, "Thermal variation od attenuation for optical fibers," vol. 30, pp. 359–370, 1979.

[81] D. P. Hand and P. S. T. Russell, "Photoinduced refractive-index changes in germanosilicate fibers." Optical Letters, pp. 102–104, 1990.

[82] J. Huang *et al.*, "Microwave Interrogated Sapphire Fiber Michelson Interferometer for High Temperature Sensing," vol. 27, no. 13, pp. 1398–1401, 2015.

[83] E. Chmielewska, W. Urban, and W. J. Bock, "Measurement of pressure and temperature sensitivities of a Bragg grating imprinted in a highly birefringent side-

hole fiber," 2003.

[84] B. Cheng, L. Hua, Q. Zhang, J. Lei, and H. Xiao, "Microwave-assisted frequency domain measurement of fiber-loop ring-down system," *Opt. Lett.*, vol. 42, no. 7, p. 1209, 2017.

[85] L. Hua, Y. Song, B. Cheng, W. Zhu, Q. Zhang, and H. Xiao, "Coherence-length-gated distributed optical fiber sensing based on microwave-photonic interferometry," *Opt. Express*, vol. 25, no. 25, pp. 31362–31376, 2017.

[86] S. T. Ross, "Ultrahigh-NA oil immersion optics with spherical aberration correction capability," *American Laboratory*, vol. 35, no. 8. pp. 14–17, 2003.

[87] J. Huang, L. Hua, X. Lan, T. Wei, and H. Xiao, "Microwave assisted reconstruction of optical interferograms for distributed fiber optic sensing.," *Opt. Express*, vol. 21, no. 15, pp. 18152–18159, 2013.

[88] S. Datta and B. Das, "Electronic analog of the electro-optic modulator," *Appl. Phys. Lett.*, vol. 56, no. 7, pp. 665–667, 1990.

[89] A. V Oppenheim, R. W. Schafer, and J. R. Buck, *Discrete Time Signal Processing*, vol. 1999. 1999.

[90] L. Hua, Y. Song, J. Huang, X. Lan, Y. Li, and H. Xiao, "Microwave interrogated large core fused silica fiber Michelson interferometer for strain sensing," *Appl. Opt.*, vol. 54, no. 24, pp. 7181–7187, 2015.

[91] W. R. Habel and K. Krebber, "Fiber-optic sensor applications in civil and geotechnical engineering," *Photonic Sensors*, vol. 1, no. 3, pp. 268–280, Sep. 2011.

[92] J. Leng and A. Asundi, "Structural health monitoring of smart composite materials

by using EFPI and FBG sensors," *Sensors Actuators A Phys.*, vol. 103, no. 3, pp. 330–340, 2003.

[93] M. Majumder, T. K. Gangopadhyay, A. K. Chakraborty, K. Dasgupta, and D. K. Bhattacharya, "Fibre Bragg gratings in structural health monitoring-Present status and applications," *Sensors and Actuators, A: Physical*, vol. 147, no. 1. pp. 150–164, 2008.

[94] K. Peters, "Polymer optical fiber sensors—a review," *Smart Mater. Struct.*, vol. 20, no. 1, p. 13002, Jan. 2011.

[95] J. Zubia and J. Arrue, "Plastic Optical Fibers: An Introduction to Their Technological Processes and Applications," *Opt. Fiber Technol.*, vol. 7, no. 2, pp. 101–140, 2001.

[96] Z. Zhang and X. Bao, "Distributed optical fiber vibration sensor based on spectrum analysis of Polarization-OTDR system.," *Opt. Express*, vol. 16, no. 14, pp. 10240–10247, 2008.

[97] S. Liehr *et al.*, "Polymer Optical Fiber Sensors for Distributed Strain Measurement and Application in Structural Health Monitoring," vol. 9, no. 11, pp. 1330–1338, 2009.

[98] S. Liehr and K. Krebber, "Phase-OFDR for Distributed Disturbance Measurement," in *SPIE 9916, Sixth European Workshop on Optical Fibre Sensors*, 2016, vol. 9916, pp. 19–22.

[99] Y. Koike, T. Ishigure, and E. Nihei, "High-Bandwidth Graded-Index Polymer Optical Fiber," *J. Light. Technol.*, vol. 13, no. 7, pp. 1475–1489, 1995.

[100] A. Risch and R. Hellmann, "Picosecond laser patterning of ITO thin films," in *Physics Procedia*, 2011, vol. 12, no. PART 2, pp. 133–140.

[101] C. Schäfer, H. M. Urbassek, and L. V. Zhigilei, "Metal ablation by picosecond laser pulses: A hybrid simulation," *Phys. Rev. B - Condens. Matter Mater. Phys.*, vol. 66, no. 11, pp. 1154041–1154048, 2002.

[102] J. Jandeleit, A. Horn, R. Weichenhain, E. . Kreutz, and R. Poprawe, "Fundamental investigations of micromachining by nano- and picosecond laser radiation," *Appl. Surf. Sci.*, vol. 127, pp. 885–891, 1998.

[103] J. H. Bechtel, W. Lee Smith, and N. Bloembergen, "Two-photon photoemission from metals induced by picosecond laser pulses," *Phys. Rev. B*, vol. 15, no. 10, pp. 4557–4563, 1977.

[104] R. Penttilla, H. Pantsar, and P. Laakso, "Picosecond Laser Processing – Material," *Scanning*, pp. 502–512, 2007.

[105] J. Davis, T. Edgar, J. Porter, J. Bernaden, and M. Sarli, "Smart manufacturing, manufacturing intelligence and demand-dynamic performance," *Comput. Chem. Eng.*, vol. 47, pp. 145–156, 2012.

[106] C. Baumgarten *et al.*, "1 J, 05 kHz repetition rate picosecond laser," *Opt. Lett.*, vol. 41, no. 14, p. 3339, 2016.

[107] D. Y. Wang, Y. Wang, M. Han, J. Gong, and A. Wang, "Fully distributed fiber-optic biological sensing," *IEEE Photonics Technol. Lett.*, vol. 22, no. 21, pp. 1553–1555, 2010.

[108] K. P. O'Flynn and K. T. Stanton, "Laser sintering and crystallization of a bioactive

glass-ceramic," *J. Non. Cryst. Solids*, vol. 360, no. 1, pp. 49–56, 2013.

[109] B. Rethfeld, D. S. Ivanov, M. E. Garcia, and S. I. Anisimov, "Modelling ultrafast laser ablation," *Journal of Physics D: Applied Physics*, vol. 50, no. 19. 2017.

[110] A. T. Giannitsis, "Microfabrication of biomedical lab-on-chip devices. A review," *Est. J. Eng.*, vol. 17, no. 2, p. 109, 2011.

[111] D. Atkinson and J. McDaniel, "Microchannel reactors in fuel production," *Pet. Technol. Q.*, vol. 15, no. 3, pp. 95–98, 2010.

[112] P. Abgrall and A. M. Gué, "Lab-on-chip technologies: Making a microfluidic network and coupling it into a complete microsystem - A review," *Journal of Micromechanics and Microengineering*, vol. 17, no. 5. 2007.

[113] M. Beresna, M. Gecevičius, and P. G. Kazansky, "Ultrafast laser direct writing and nanostructuring in transparent materials," *Adv. Opt. Photonics*, vol. 6, no. 3, p. 293, 2014.

[114] R. E. Wagner, "Laser drilling mechanics," *J. Appl. Phys.*, vol. 45, no. 10, pp. 4631–4637, 1974.

[115] Y. Li *et al.*, "Three-dimensional hole drilling of silica glass from the rear surface with femtosecond laser pulses," *Opt. Lett.*, vol. 26, no. 23, pp. 1912–1914, 2001.

[116] L. Jiang *et al.*, "High-throughput rear-surface drilling of microchannels in glass based on electron dynamics control using femtosecond pulse trains," *Opt. Lett.*, vol. 37, no. 14, p. 2781, 2012.